The hydraulic properties of faults in unconsolidated sediments and their impact on groundwater flow

a study in the Roer Valley Rift System and adjacent areas in the Lower Rhine Embayment

V.F. Bense

The research reported in this thesis took place within the framework of the Netherlands Research School of Sedimentary Geology (NSG) and has been carried out at the

Vrije Universiteit Amsterdam
Faculty of Earth and Life Sciences
Department of Hydrology and Geo-Environmental Sciences
De Boelelaan 1085
1081 HV Amsterdam
The Netherlands

ISBN 90-9018334-5
NUR 934

Cover: The Geleen Fault as seen in the trenched outcrop that is discussed in Chapter 3 (photograph by Laurens Bouwer)

This document has been type-set using the LaTeX system of programs and packages.

VRIJE UNIVERSITEIT

The hydraulic properties of faults in unconsolidated sediments and their impact on groundwater flow

a study in the Roer Valley Rift System and adjacent areas in the Lower Rhine Embayment

ACADEMISCH PROEFSCHRIFT

ter verkrijging van de graad van doctor aan
de Vrije Universiteit Amsterdam,
op gezag van de rector magnificus
prof.dr. T. Sminia,
in het openbaar te verdedigen
ten overstaan van de promotiecommissie
van de faculteit der Aard- en Levenswetenschappen
op donderdag 16 september 2004 om 13.45 uur
in de aula van de universiteit,
De Boelelaan 1105

door

Victor Franciscus Bense

geboren te Amsterdam

promotoren:	prof.dr. S.A.P.L. Cloetingh
	prof.dr. J.J. de Vries
copromotor:	dr. R.T. van Balen

Faults

They came to tell your faults to me,
They named them over one by one;
I laughed aloud when they were done,
I knew them all so well before, –
Oh, they were blind, too blind to see
Your faults had made me love you more.

Sarah Teasdale (1884-1933)

leescommissie: dr. R.T. van Balen
dr. J.C. Gehrels
prof.dr. P.A. Kukla
dr. J.M. Verweij
dr. J.J. Walsh

Contents

Figures

Tables

Samenvatting

Het is al langer bekend dat breuken die voorkomen in de ondergrond van zuidoost Nederland barrières kunnen vormen voor grondwaterstroming. Op de locaties van breuken komen vaak opvallend hoge hydraulische gradiënten voor in horizontale richting die wijzen op een lage hydraulische doorlatendheid van het breukvlak. De meer precieze invloed van breuken op grondwaterstromingspatronen was tot nu toe echter onduidelijk. Omdat het meeste drinkwater in het zuidoosten van Nederland wordt gewonnen uit de sedimentpaketten waarin deze storende zones voorkomen, is een beter inzicht in hoe breuken bijvoorbeeld de verspreiding van vervuild grondwater beïnvloeden, niet alleen wetenschappelijk interessant maar ook van praktisch belang. Het primaire doel van het onderzoek dat beschreven is in dit proefschrift, is het verkrijgen van een beter inzicht in de hydraulische en lithologische structuur van breukzones en het effect van breuken op grondwaterstromingspatronen in het gebied van het Roer Vallei Rift Systeem in zuidoost Nederland en aangrenzende gebieden in Duitsland. Voor het bestuderen van deze onderwerpen zijn een aantal veldonderzoeken uitgevoerd op verschillende ruimtelijke schalen variërend van cm-schaal (Hoofdstuk 1 en 2) tot op de veldschaal van enkele honderden meters (Hoofdstuk 3). Daarnaast zijn er hydrogeologische gegevens uit het gebied van de honderden meters diepe bruinkoolgroeves in het Duitse gedeelte van het studiegebied gebruikt om de invloed van breuken op regionale grondwaterstromingspatronen te evalueren (Hoofdstuk 5).

In het eerste Hoofdstuk van dit proefschrift wordt een overzicht gepresenteerd van hydrologische verschijnselen die waargenomen zijn in samenhang met breuken in de ondergrond van het studiegebied. Deze eerste analyse is gebaseerd op interpretatie van bestaande gegevens uit de literatuur die zijn aangevuld met, tijdens dit onderzoek uitgevoerde, veldwaarnemingen van ondiepe grondwater stijghoogtes over de Peelrandbreuk en interpretatie van luchtfoto's. Het meest opvallende verschijnsel dat samenhangt met de geringe doorlatendheid van de breuken is dat op de topografische hoger gelegen delen van het landschap grondwater aan het oppervlak uittreedt daar waar normaliter een neerwaartse stroming van grondwater plaatsvindt in de richting van de lager gelegen gebieden. In deze gebieden, die lokaal bekend staan als de *Wijstgronden*, komt de grondwaterspiegel tot dicht

aan het maaiveld waardoor zij ook tijdens de droogste periodes van het jaar nat blijven. De slechte doorlatendheid van veel breuken in het studiegebied wordt ook gereflecteerd in de stijghoogteverdeling op een regionale schaal. Met name rond het gebied van de bruinkoolwinningen in het Duitse gedeelte van het studiegebied is dat goed zichtbaar omdat daar de stijghoogtegradiënten aanzienlijk zijn versterkt ten gevolge van grootschalige grondwateronttrekingen. Terwijl het duidelijk is dat breuken horizontale grondwaterstroming sterk kunnen hinderen, suggereren gedetailleerde stijghoogtemetingen dat breuken voor verticale grondwater stroming juist een preferente stroombaan kan vormen.

Waarnemingen op micro-schaal in een gegraven sleuf over de Geleenbreuk nabij Sittard in het zuiden van Limburg, laten in detail de interne lithologische structuur van een breuk zien (Hoofdstuk 3). In deze sleuf zijn de geologische deformatiemechanismen bestudeerd die gerelateerd zullen zijn aan de geobserveerde hydrologische eigenschappen van de breuk. Met behulp van dunne-doorsnedes van sedimentmonsters is een zeer gedetaileerd beeld verkregen van de interne geologische structuren van de Geleenbreuk. De verdeling van permeabiliteit rondom de breuk die samenhangt met deze geologische structuur is geëvalueerd met behulp van laboratorium bepalingen van de doorlatendheid van ter plaatse gestoken sedimentmonsters. Het versmeren van klei langs het slechts enkele centimeters brede breukvlak zorgt waarschijnlijk voor een lage doorlatendheid van de breuk ter plaatse. Daarnaast blijkt echter ook dat grof zand langs het breukvlak kan worden verplaatst. Deze waarnemingen dragen bij aan het vormen van een realistisch hydrologisch model dat het gedrag beschrijft van ondiepe breuken in ongeconsolideerde sedimenten.

Op de iets grotere schaal, van 10 tot 100 meter, is de grondwaterstromingsituatie rondom de Peelrandbreuk nabij Uden in beeld gebracht (Hoofdstuk 4). Hiervoor zijn grondwater temperatuur metingen gebruikt als belangrijke aanvulling op stijghoogte metingen. Hierbij wordt gebruik gemaakt van het effect dat de verschillen in grondwaterstroming aan weerszijden van de breuk gereflecteerd worden in het temperatuur verloop met de diepte. In twee peilbuizen op een onderlinge afstand van $\pm$ 500 meter zijn maandelijks temperatuur-diepte metingen verricht (tot een diepte van maximaal 50 meter). Deze zijn aangevuld met temperatuurmetingen in een profiel op 50 centimeter diepte onder een sloot loodrecht op de Peelrandbreuk. Met behulp van numerieke modellering van grondwaterstroming gekoppeld aan warmtetransport is de interactie tussen seizoenale variaties in oppervlaktetemperatuur en ondiepe grondwaterstroming gesimuleerd. Het blijkt dat met deze ondiepe geothermische methode de heterogeniteit van het stromingsveld rondom de breuk fraai in beeld gebracht kan worden. Opmerkelijk is dat om het wat diepere geothermische regime te kunnen begrijpen, zoals dat is geobserveerd in twee peilbuizen aan beide zijden van de breuk, de invloed van recente opwarming aan het oppervlak als gevolg van veranderende klimaat, als randvoorwaarde in het model ingevoerd moet worden.

De invloed van breuken op het regionale grondwatersysteem op de regionale schaal is zeer duidelijk zichtbaar in het gebied van de bruinkoolmijnen in het Duitse gedeelte van het studiegebied. In Hoofdstuk 5 wordt de invloed van kleiversmering langs het breukvlak enerzijds, en de invloed van de structuur van breuken op grondwaterstroming anderzijds

onderzocht. Voor het eerste onderwerp van dit Hoofdstuk worden methodes afkomstig uit de olie-industrie gebruikt om de hydraulische eigenschappen van breuken te schatten uit de te verwachten hoeveelheid klei die langs het breukvlak is versmeerd. Dit gebeurd aan de hand van geologische gegevens zoals de verplaatsingen langs de breuken en het kleigehalte van de lithologieën aan weerszijden van de breuk. De zo geschatte variatie van kleigehalte in het breukvlak blijkt goed te correleren met gemeten stijghoogteverschillen over de breuk. Toch blijft het moeilijk om via deze methode de hydraulische eigenschappen van de breuk te bepalen omdat het onduidelijk is wat de precieze relatie is tussen het geschatte kleigehalte in de breuk en zijn doorlatendheid. Desalniettemin zou deze methodologie een goeie eerste indicatie kunnen geven van de te verwachten variatie in hydraulische eigenschappen van een breuk voor gebruik in grondwaterstromingsmodellen. Naast de effecten van kleiversmering blijkt dat de structureel geologsiche context van een breuk essentieel is voor het inschatten van het uiteindelijke effect van de breuk op grondwaterstromingspatronen. Op de plaatsen waar zogenaamde ”overstap”-zones voorkomen is het doorgaans afsluitende karakter van breuken sterk verminderd en kan de breuk juist een goed doorlatende zone vormen waar watervoerende paketten in hydraulisch contact staan.

Het laatste Hoofdstuk van dit proefschrift is een synthese van de onderzoeksresultaten waarin de belangrijkste conclusies van elk deelonderzoek nog eens zijn samengevat. Naast een beter inzicht in het hydrogeologisch karakter van de breuken, is wellicht de belangrijkste van deze conclusies dat breuken niet alleen als min of meer voor grondwaterstroming gesloten zones kunnen worden beschouwd, maar ook als plaatsen waar aquifers in contact met elkaar kunnen staan, hetzij door een zeer sterke anisotrope doorlatendheid structuur (Hoofdstuk 3) danwel als gevolg van open structuren in de breukvlakken zelf (Hoofdstuk 5).

1

General Introduction

This first Chapter introduces the subject matter of the study that is reported in this thesis. Here, the scientific relevance of this study and its specific research objectives are explained. In order to facilitate the reading of this thesis, at the end of this introduction the set-up of this thesis is outlined by briefly summarizing the contents of each Chapter.

1.1 Background

A short description of the current state of knowledge on groundwater flow around fault zones in unconsolidated sediments is provided here after which the objectives of the present study are presented.

1.1.1 Groundwater flow in relation to faults

The notion that faults in sedimentary aquifers can be of fundamental impact to the groundwater flow system of an area is not standard in hydrological thinking. Although, notably in crystalline rocks faults and related fractures are often the most important generators of secondary porosity and associated aquifer zones [*e.g. Caine et al.*, 1996], the subject is not specifically discussed in the mainstream hydrological handbooks [*e.g. Freeze and Cherry*, 1979; *Domenico and Schwartz*, 1998]. In this thesis focus will be on the impact of faults on groundwater flow in unconsolidated sediments where, other than in crystalline rocks, faults can form strong barriers to fluid movement. However, only few studies present generalized, conceptual, models for the hydrogeological build-up of fault zones in unconsolidated sediments [*e.g. Heynekamp et al.*, 1999; *Rawling et al.*, 2001]. Applied research shows how important faults are to, for example, the distribution of saline water in coastal areas [*e.g. Barker et al.*, 1998; *Yechieli et al.*, 2001] or to the possible spread of radioactive waste and other contaminants in aquifer systems *Nuclear Energy Agency* [1996]; *Mal'kovskii and Pek* [2001]; *Ofoegbou et al.* [2001]. On regional scale, *Wallbraun* [1992] shows how faults can compartmentalize whole groundwater flow systems.

1.1.2 Objectives of the present study

The general aim of the present study is to improve our understanding of the impact of fault zones on groundwater flow in unconsolidated sediments. In this thesis work, there is a focus on the groundwater flow situation in the Roer Valley Rift System that is located in the southeastern parts of the Netherlands and the adjacent areas in Germany. In this sedimentary basin, the aquifer system is formed by fluvial and marine sediments of Quaternary and Tertiary age. Groundwater movement in these aquifers is monitored by a very dense network of groundwater observation wells. The unconsolidated sediments in the study area are cut by active normal faults, of which the most important are the Peel Boundary Fault Zone (known as the Rurrand Fault in the German part of the system) and the Feldbiss Fault Zone. From the sparse earlier studies in the study area, it is known that faults in the system can strongly hamper groundwater movement [*e.g. Ernst and De Ridder*, 1960; *Wallbraun*, 1992; *Stuurman and Atari*, 1997].

In order to reach the primary goal of this study, four sub-topics on various spatial scales have been taken into consideration in the study area. In these studies the following specific research questions were addressed:

1. How is the presence of faults in the subsurface reflected in local hydrological conditions within the Roer Valley Rift System?
2. What are the internal structure and associated hydraulic properties of fault zones in unconsolidated sediments?
3. What is the relevance of fault zones to shallow and local groundwater flow paths?
4. What is the impact of the larger scale structure of fault zones on regional groundwater flow?

1.2 Approach

In the present study the hydrogeological impact of faults is described at different scales, from μm-scale to the regional scale ($\sim$10s of km). It is expected that the observations at micro-scale help to understand the hydraulic properties of a fault at larger scales. However, at each scale level different field- and analysis techniques are required.

At the smallest scale, at the outcrop, thin-sections of sediment samples were analyzed to understand the impact of small-scale deformation on the hydraulic properties of the sediment. In addition, measurements of hydraulic conductivity were

carried out on core-plug samples of the same sediment. In order to find out what the larger scale impact is of these deformation structures along the fault, groundwater flow models have been set up which are constrained with both hydraulic and geothermal data. At this stage also the hydrochemistry of groundwater samples yielded important pieces of information on the origin and direction of groundwater flow. At a regional scale groundwater flow is strongly compartmentalized by faults. This compartmentalization of aquifers is very similar to patterns in fluid pressure observed in deep hydrocarbon basins. Techniques to hydraulically characterize faults in these regional systems have been developed in hydrocarbon recovery related studies. These were explored for their applicability in a hydrogeological context during the present study.

The research reported in this thesis is strongly multi-disciplinary between structural geology and hydrology. Techniques from both fields were applied and the subjects that are discussed are probably along the edges of these two scientific fields. However, the present study should be regarded as a hydrogeological one into which many techniques and insights from structural geological research are explored for their applicability. This is especially true for Chapters 3 and 5. Surprisingly, there has been far more attention to the impact of faults on fluid flow in hydrocarbon-recovery related studies than in groundwater flow studies. This is surprising because data for groundwater flow studies are generally far more abundant than that for fluid flow studies, off-shore, in deeply buried hydrocarbon reservoirs. Therefore, groundwater flow data can significantly contribute to our understanding of fault hydraulic properties.

1.3 Thesis outline

Chapter 2 The first study presented in this thesis addresses specifically research questions 1, 3 and 4. A multi-scale survey of hydrogeological observations in the Roer Valley Rift System and adjacent areas in Germany is presented in this Chapter in order to identify the overall influence of fault zones on groundwater flow. Analysis of hydraulic head data over the Peel Boundary Fault Zone, from existing maps and as observed at meter-scale in a trenched outcrop, show that groundwater recharge and / or discharge preferentially occurs along faults. On the other hand, hydraulic head data from the German part of the system show that faults act generally as strong barriers to horizontal groundwater flow. The analysis in this Chapter shows that faults in the Roer Valley Rift System can act as conduits for vertical groundwater movement while they impede groundwater flow horizontally.

Chapter 3 Research question 2 is central in this Chapter. The apparent strongly anisotropic behavior of fault zones that is inferred from the data presented in Chapter 2, can be better understood from the geological architecture of faults. Deformation mechanisms (*i.e.* clay smearing, diagenetic effects and particulate flow) along faults in unconsolidated sediments and its hydrological implications are studied in great detail in a trenched outcrop over the Geleen Fault (part of the Feldbiss Fault Zone). Digital image analysis is used to unravel the permeability structure, at micro-scale, of the Geleen Fault. This study learns that faults are likely to be very anisotropic and heterogeneous features.

Chapter 4 The effect of faults on shallow groundwater flow (research question 3), as a result of the fault zone processes that were observed in the trench over the Geleen Fault (Chapter 3), has been evaluated in a field study around the Peel Boundary Fault Zone close to the village of Uden. It appeared that the available network of piezometers was insufficient to map the spatial distribution of groundwater flow velocities close to the surface in detail. Therefore, shallow geothermal methods were applied to reveal the small scale variability of the shallow groundwater flow field around the fault which is strongly associated with local geological heterogeneity. Numerical models of coupled groundwater flow and heat transport allowed to understand the observed thermal patterns and to discern the a-typical pattern of groundwater discharge and recharge areas at this location.

Chapter 5 Groundwater flow patterns around open pit lignite mines operated in the Lower Rhine Embayment adjacent to the Roer Valley Rift System in Germany, show the hydrogeological impact of clay smearing and fault relay zones (research question 4). Very large groundwater extraction around open pit lignite mines has led to strongly transient and increased groundwater flow velocities in the area. Groundwater flow patterns are influenced by clay smearing along faults, resulting in high hydraulic gradients over many faults, while fault relay zones are the locations where this sealing behavior is interrupted. Clay smearing can be parameterized using the Shale Gouge Ratio (SGR) method, which is a common tool in hydrocarbon related studies, to predict fault zone hydraulic properties. The applicability of this method has been tested on groundwater flow and geological data from the Lower Rhine Embayment. The impact of fault relay structures has been evaluated using numerical groundwater flow simulations.

Chapter 6 In the last Chapter, the outcomes of the work that is reported in this thesis are synthesized and general conclusions are drawn on the hydrogeology of fault zones in unconsolidated sediments. Moreover, recommendations and suggestions are made for future scientific research in this subject area.

2

The hydrological expression of faults in the study area

Abstract

The hydrogeology of the Roer Valley Rift System is strongly influenced by the hydraulic properties of faults. The hydrogeological impact of faults is illustrated by examples from the SE Netherlands and the adjacent lignite mining areas within the Roer Valley Rift System. Hydraulic head discontinuities over the main faults in the latter area can be up to tens of meters as a result of extremely large groundwater extractions in combination with the relatively low conductivity of the main faults. Within the Netherlands, outside the mining areas, such large groundwater extractions do not take place, and groundwater fluxes are smaller. In this situation natural hydraulic head differences over the main faults are limited to several meters. Hydraulic head profiles over faults provide a first estimate of fault hydraulic properties that can be quantified using simple analytical solutions. The impact of faults on near surface processes is reflected in vegetation patterns and the structure of drainage networks, aquifer structure and hydraulic head patterns. Faults can thus be of great influence on transport processes in the sub-surface as well as on water-related phenomena at the surface, and should accordingly be taken into consideration in studies related to water management, contamination and environmental impact. Faults that have an enhanced vertical permeability are difficult to detect when horizontal groundwater flow is studied, which is probably the main reason why they are rarely described. These faults may, however, form important preferential flow paths to vertical groundwater movement.

This Chapter is largely based upon: Bense, V.F., Van Balen, and J.J. De Vries, . The impact of faults on the hydrogeological conditions in the Roer Valley Rift System: an overview *Netherlands Journal of Geosciences/Geologie en Mijnbouw, 82*, 41-53, 2003.

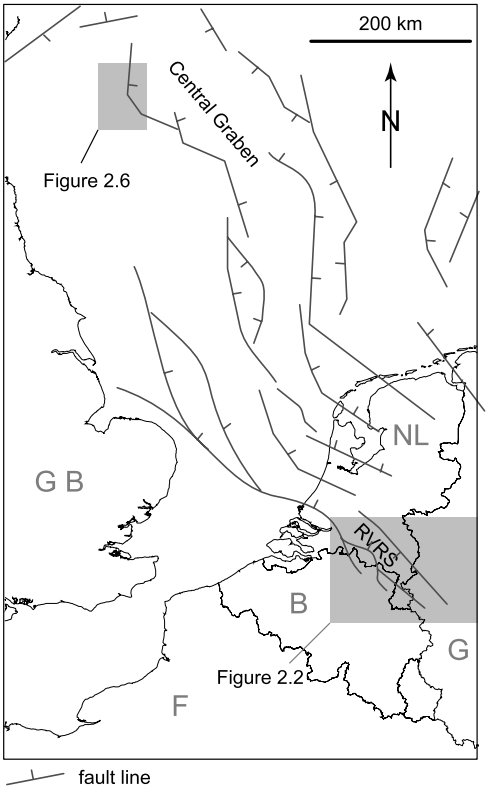

Figure 2.1: Structural overview map of the North Sea basin (after Knott, 1993; Ziegler, 1994). RVRS = Roer Valley Rift System, GB = Great-Britain, G = Germany, B = Belgium, NL = The Netherlands, F = France.

2.1 Introduction

The Roer Valley Rift System (RVRS) is located in the southeastern part of the Netherlands and adjacent parts of Belgium and Germany (Figure 2.1). The RVRS forms the southeastern part of the North Sea Basin which is part of a Cenozoic mega-rift system crossing western and central Europe [*Ziegler*, 1994]. The RVRS has a complex Mesozoic and Cenozoic tectonic history, comprising several extension and inversion phases. The current extension phase started during the Late Oligocene [*Geluk et al.*, 1994]. The RVRS comprises four main structural elements: the northern part of the Campine Block in the south, the Roer Valley Graben in the center, and the Peel Block and Venlo Block in the northeast (Figure 2.2). The Roer Valley Graben is separated from the adjoining blocks by the Feldbiss Fault Zone in the south and the Peel Boundary Fault Zone in the north. In the area of investigation these are the most active fault zones during the Quaternary [*e.g. Paulissen et al.*, 1985; *Houtgast and van Balen*, 2000]. The central Roer Valley Graben is filled with

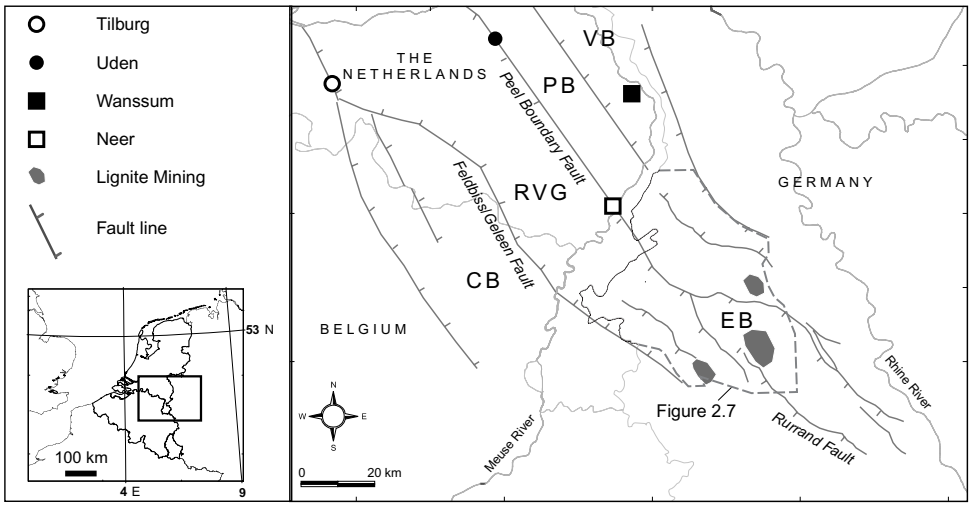

Figure 2.2: The Roer Valley Rift System (RVRS) with locations of sites as discussed in the text. RVG = Roer Valley Graben, VB = Venlo Block, PB = Peel Block, CB = Campine Block, EB = Erft Block.

up to $1200\,\mathrm{m}$ of Late Oligocene - Recent sediments comprising fine-grained marine deposits overlain by a relatively thin sequence (± 50 m) of medium to coarse grained fluvial-deltaic deposits of Pleistocene age. The same sequence has a total thickness of up to $200\,\mathrm{m}$ on the Peel Block [*Geluk et al.*, 1994]. The coarse grained fluvial deposits at the top of the sequence form the main aquifer in the study area.

In general, faults in the unconsolidated sediments in the RVRS appear to represent a barrier to horizontal groundwater flow. In addition, faulting has induced a stepped morphology, through small fault scarps. Figure 2.3 illustrates the case that groundwater, moving from a topographically more elevated block to a lower area, has to pass a low-conductivity fault zone. In such a situation, a high groundwater table in the upstream area is found, together with a high hydraulic gradient over the fault line. Where the groundwater table intersects the topography, the groundwater outcrop zone will be an area with sapping erosion. Differences in bank erodibility and stream deflection are other possible aspects of interaction between faults, morphology and hydrology [*De Vries*, 1974; *Vandenberghe*, 1990; *De Vries*, 1994]. It should be emphasized that small-scale variations in topography and soil permeability normally have a large influence on near surface hydrological conditions in areas with a shallow groundwater table. This is due to the fact that small scale vari-

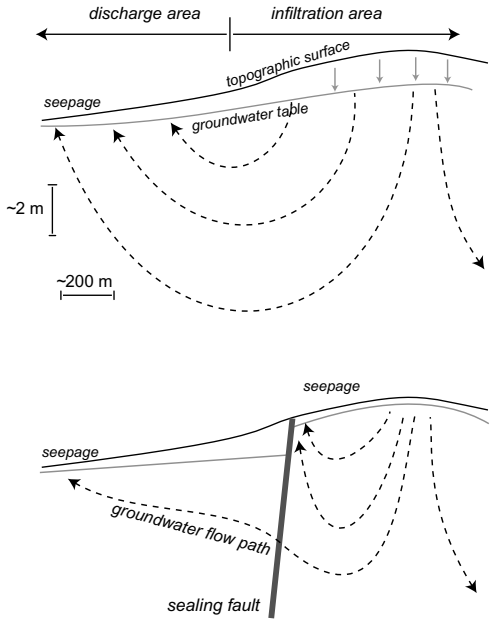

Figure 2.3: The difference between shallow hydrological systems as a result of the presence of a fault zone with a low conductivity in the subsurface.

ations in relief under such conditions cause relatively large variations in groundwater depth and thus in storage and buffering capacity which in turn enhances the differentiation in bare surface processes like erosion and soil formation [*De Vries*, 1994]. This applies to most of the Netherlands where this interaction is strongly reflected in the increase in drainage density with decreasing groundwater depth [*De Vries*, 1974, 1994]

One striking example of how a fault can influence the local hydrological situation is illustrated by aerial photographs of the vicinity of the city of Tilburg (Figure 2.4). The northward extension of the Feldbiss Fault Zone, here called the Gilze-Rijen Fault Zone, cuts through farming land. The eastern part of this land has a higher soil moisture content (darker tone on the image) than the western part. In this case, juxtaposition rather than the hydraulic properties of the fault zone itself, is the cause for the observed soil moisture patterns. It is evident that such contrasts can lead to considerable differences in crop yield between the different parts of this plot. The hydrogeological situation at this location will be discussed in more detail below. The impact of small-scale topographical features on the groundwater flow pattern reduces with depth. The vertical penetration of the influence of topographic undulations as well as the vertical propagation of groundwater level oscillations in

general increases with the wavelength and amplitude of the topographic phenomena [*Zijl*, 1993].

In this Chapter an overview and synthesis of the influence of rift-related faults on the hydrogeological conditions of the Roer Valley Rift System is presented. In addition, an example from the geologically associated North Sea basin is given (Figure 2.1). The examples and results from recent field studies, make clear that the impact of faults is strongly scale dependent. In this Chapter, it is first discussed how the hydraulic properties of faults can be quantified. Next, several examples are presented of fault-induced groundwater flow perturbations at different length scales, ranging from $100\,\mathrm{km}$ to $1\,\mathrm{m}$. Finally, the results and propose are discussed and a few generalized conclusions together with their implication to practical problems dealing with groundwater flow in areas where faults are cutting through unconsolidated sediments are presented.

2.2 Hydraulic characterization of fault zones

The most straightforward way to parameterize the hydraulic properties of a fault zone is to calculate its specific resistance (r [days]) to flow perpendicular to the fault zone (*i.e.* across the fault). The resistance of a fault in that case, is here defined as:

$$r = \frac{w}{K_f} \tag{2.1}$$

where w [m]is the fault zone width and K_f [m / s] is the bulk hydraulic conductivity of the fault zone material.

The rate of horizontal groundwater flow through an aquifer that has thickness D [m], length L [m], and a hydraulic conductivity in the direction of flow K [m / day], is given by Darcy's Law:

$$\vec{q} = -KD\frac{\Delta h_L}{L} \tag{2.2}$$

where Δh_L [m] is the hydraulic head difference over distance L. When L equals w and continuity of groundwater flux exists over the fault zone, combination of equation 2.2 and equation 2.1 allows to formulate the resistance of a fault zone as:

$$r = D_f \left| \frac{\Delta h_f}{q} \right| \tag{2.3}$$

where Δh_f [m] is the hydraulic head difference over the fault.

The specific flow resistance to flow perpendicular to the fault zone is the most general form to characterize the hydraulic properties of a fault zone as they are

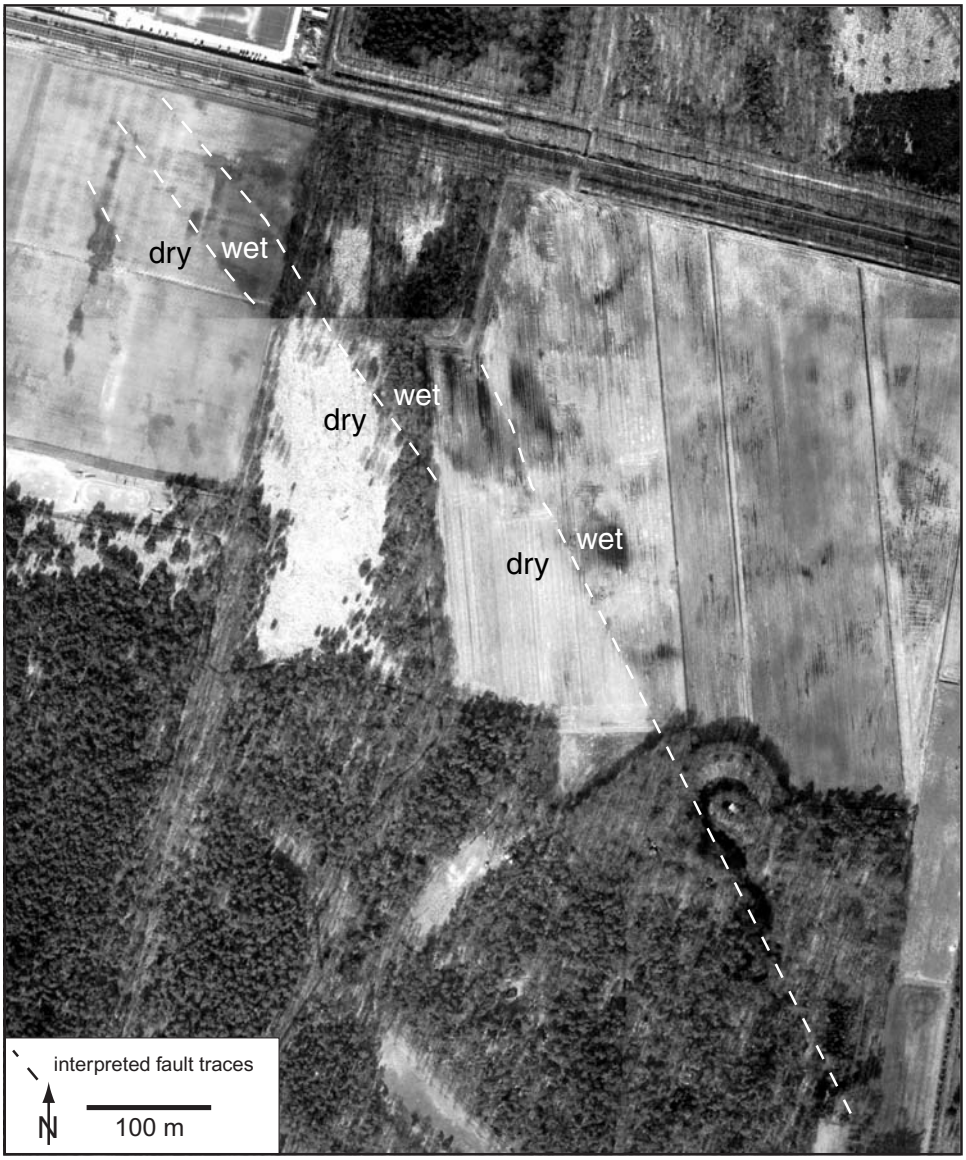

Figure 2.4: Aerial photograph of the Gilze-Rijen Fault as it crosses farming land near the city of Tilburg (with permission of the municipality of Tilburg). The fault clearly separates different hydrologic units; for location see Figure 2.14.

lumped into one parameter. On the other hand, the regional context can be considered using the transmissivity of the fault zone that equals the product of the vertically averaged hydraulic conductivity (K_f) and the thickness of the aquifer (D_f) over the fault zone.

The relation between specific resistance of the fault zone, r, and its transmissivity as $K_f D_f$ [m^2 / day] can be stated as:

$$r = \frac{D}{K_f D_f} w \tag{2.4}$$

Haneberg [1995] used the latter regional approach to calculate the hydraulic head profile over a regional aquifer that is cut by a fault zone (Figure 2.5). Three flow domains can be distinguished; the transmissivity of the left hand side block of the fault ($K_l D_l$), the transmissivity of the fault zone itself ($K_f D_f$) and the transmissivity of the right hand side block ($K_r D_r$). If exchanges of water with underlying aquifer systems or the surface drainage system are negligible, steady-state conditions require continuity of flux over the series of flow domains so that $q_l = q_f = q_r$. This implies for one-dimensional flow within each flow domain (Figure 2.5):

$$\frac{d^2 h}{dx} = 0 \tag{2.5}$$

Under confined conditions and for a constant thickness of the aquifer, solutions for equation 2.5 show that the hydraulic gradient i over each part of the aquifer system is linear, thus:

$$K_r D_r i_r = K_f D_f i_f = K_l D_l i_l \tag{2.6}$$

If recharge or discharge is taking place to or from the fault zone equation 2.5 changes to:

$$\frac{d^2 h}{dx} = -\frac{R}{K_f D_f} \tag{2.7}$$

where R [m / day] represents the rate of recharge ($R > 0$) or discharge ($R < 0$) to or from the fault zone.

Figure 2.5 illustrates a head profile under confined conditions for the case that $K_f D_f << K_r D_r < K_l D_l$ and $R = 0$. Since continuity of flux exists between each domain, the ratio between two aquifer transmissivities is inversely proportional to the ratio of the aquifer gradients. In order to produce a high enough gradient over the fault zone to satisfy a constant flux, an up-gradient head excess is produced relative to the undisturbed situation (*i.e.* if no fault was present in the system). In the left-hand aquifer the same principle results in a loss of head relative to the

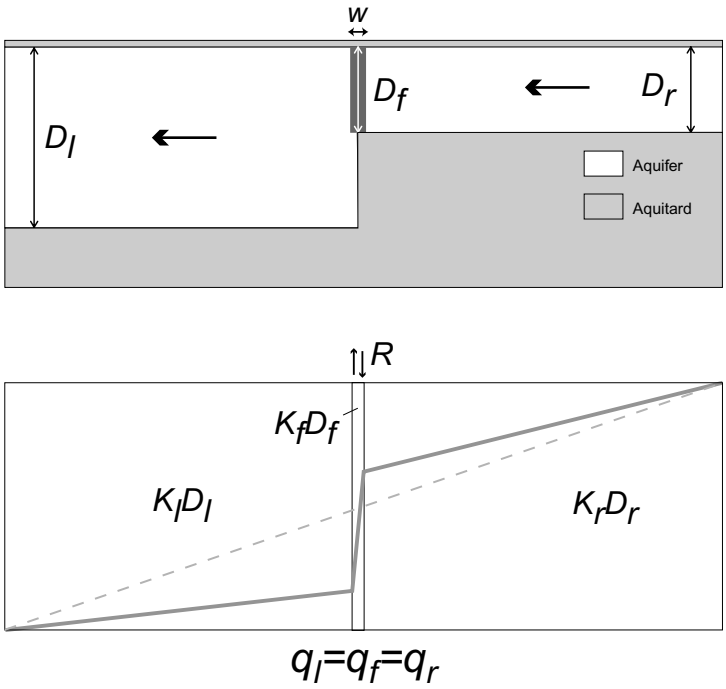

Figure 2.5: Schematized aquifer structure over which the hydraulic head profile can be described using a simple analytical approach ($K_l D_l > K_r D_r >> K_f D_f$). Arrows indicate the direction of groundwater flow from left to right.

undisturbed head gradient. If the topographic conditions are not in agreement with these required gradients continuity of flux can be lost. Groundwater will discharge near the fault zone if the topography lowers towards the fault zone in the right hand system (Figure 2.5).

If transmissivity ratios are estimated from the hydraulic gradients on both sides of a fault zone, and the fault zone width (w) can be estimated as well, the actual value of fault zone transmissivity can be calculated from one independent observation of the magnitude of the transmissivity of the aquifer on one side of the fault zone. Although this description of hydraulic head profiles over idealized faults is in principle simple, in most cases it requires many field observations to obtain enough information for a more complex interpretation of groundwater flow through a fault zone.

The impact on the hydraulic head profile is less significant when a fault zone

has a higher transmissivity than the flanking aquifers. This is because flow across a high- transmissivity zone is limited by the ability of the up gradient aquifer to supply a sufficient amount of water to maintain the flux through the fault zone. In this case the gradient in the fault zone will be lower than in the flanking aquifers and therefore will have less impact on the gradient in the flanking aquifers than when the fault is a relatively low transmissive zone. This effect may be one of the reasons that, as in this Chapter, faults that form barriers to groundwater flow are more frequently reported on than faults being high-transmissive zones. However, faults forming a barrier to horizontal groundwater flow may simultaneously act as important pathways to vertical groundwater flow.

2.3 Examples of the impact of faults on groundwater flow patterns

Most researchers focusing on the migration and trapping of hydrocarbons, are well aware of the importance of faults to the sub-surface hydrogeological conditions. For example, faults that bound pore water pressure cells and form seals to hydrocarbon accumulations are a common and well studied phenomenon in the North Sea basin [*e.g. Knott*, 1993; *Van Balen et al.*, 2000]. Since the RVRS forms the southernmost, on shore part of the North Sea basin (Figure 2.2), the hydrogeologic properties of faults at larger depths as inferred from hydrocarbon exploration and production data will be discussed in the first section. Subsequently, several on shore cases where faults are clearly expressed in the hydrogeology of the RVRS are discussed.

2.3.1 Regional scale (>10 km)

Sealing faults at large depths in the Roer Valley Rift System

In the northwestern part of the RVRS several oil and gas accumulations are situated in fault bounded Triassic sandstone reservoirs [*Winstanley*, 1993]. In this case the sealing behavior of the faults can be largely explained by juxtaposition of reservoir rock, *i.e.* sandstones against Jurassic claystones. These faults are part of the same larger rift system as the pressure sealing faults in the Central Graben. Geological structure from basin-scale to the local scale has a primary control on the distribution of overpressure in the Central Graben of the North Sea [*Darby et al.*, 1996, Figure 2.6].

The two principal mechanisms explaining the sealing capacity of faults in this

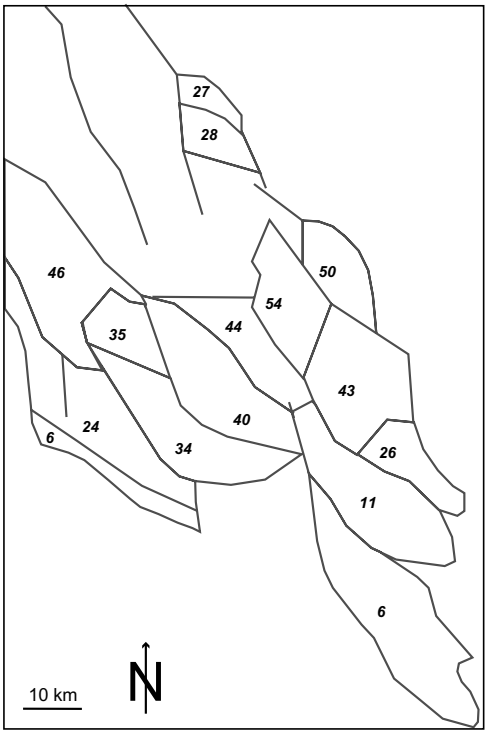

Figure 2.6: Fault bounded pressure cells in the Central Graben of the North Sea basin at a depth of around 3.5 kilometers; numbers indicate the amount of overpressure in MPa [redrawn after *Darby et al.*, 1996].

area are smearing of clay along the fault plane due to the faulting process and juxtaposition of lithologies that have strongly contrasting conductivities (*e.g.* shale vs. sandstone) [*Knott*, 1993]. In addition, according to *Harper and Lundin* [1997] a close relation exists between the orientation of cell-bounding faults and the present-day stress field. There are no sealing faults parallel to the NW-SE directed maximum horizontal stress, whereas the main strike orientations of the sealing faults are NNW-SSE and E-W.

Lignite mining area

The pattern of the hydraulic head distribution in deeper aquifers of the lignite mining area within the German part of the RVRS is very similar to the distribution of pressure in the Central Graben in the North Sea basin. In the lignite mining area, the origin of the head difference between the tectonic blocks is the result of large groundwater extractions and the low hydraulic transmissivity of the main faults. The complex interplay of faults with groundwater flow in the lignite mining

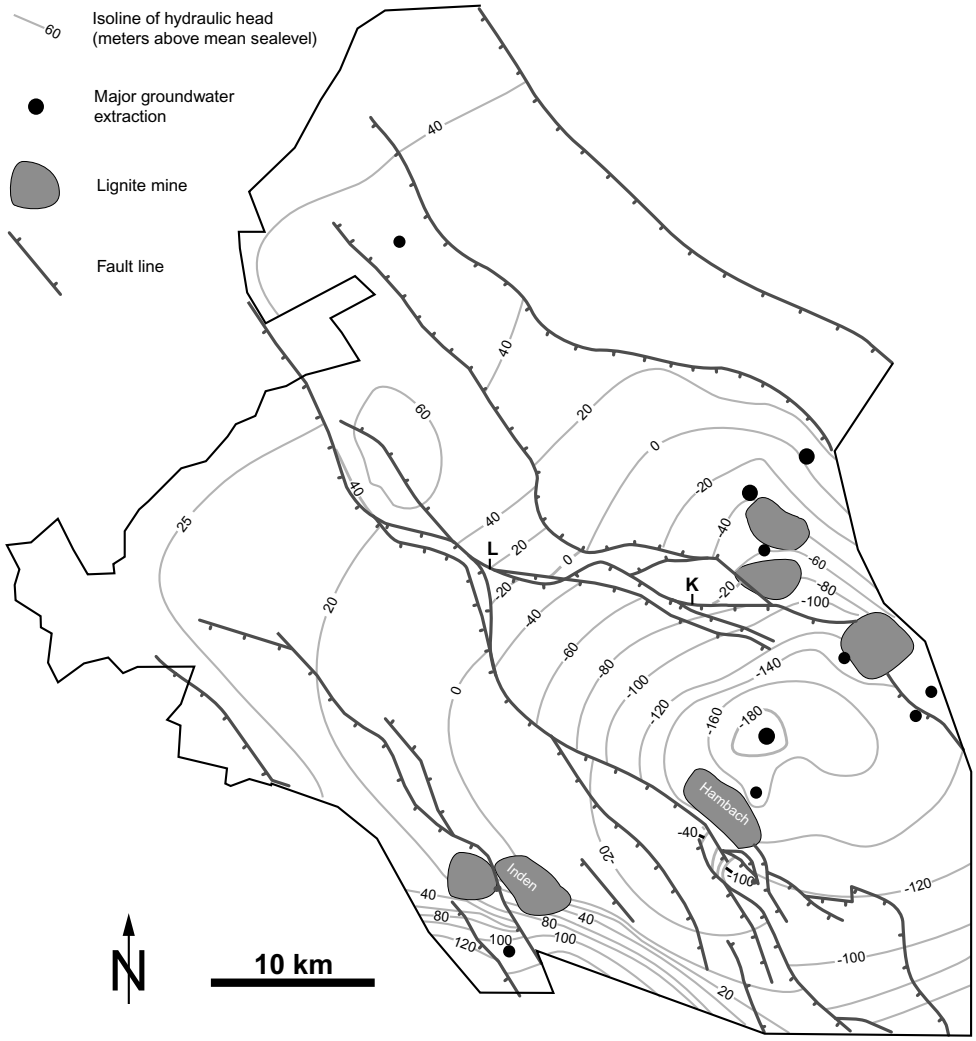

Figure 2.7: Hydraulic head pattern in the lignite mining area in middle deep aquifers. The pattern is the result of huge groundwater extractions [redrawn after *Wallbraun*, 1992]. K=section over the Kaster Fault; L=section over the Lövenicher Fault.

area is documented in greater detail than usual for hydrocarbon reservoir studies (compare for example Figures 2.6 and 2.7). Figure 2.7 shows the hydraulic head distribution in one of the deeper confined aquifers in the lignite mining area.

Mining for lignite takes place in open pits of around $300\ \mathrm{m}$ deep. In order to

construct mines to these depths, groundwater levels must be below the level of mining. This is realized through large groundwater extractions of which the most important well fields are indicated on Figure 2.7. The lowering of the groundwater levels has resulted in hydraulic head patterns that reveal that a great variation in fault permeability must exist. Some faults are sealing, causing locally very high hydraulic head gradients. Others appear to have little or no visible impact on the hydraulic head distribution. Hydraulic properties vary between individual faults but can also vary along the strike of a single fault. Like in hydrocarbon studies, factors that can explain these variations are the geometry of the fault zone, which depends on the fault throw, fault orientation, aquifer thickness, and the efficiency of fault zone processes, such as clay smearing and cataclasis. *Wallbraun* [1992] quantified the observed fault hydraulic resistance at various locations using numerical simulations. He did this for the aquifer for which isolines of hydraulic head are shown in Figure 2.7. The resistance of the 'Lövenicher' fault zone was calculated to be $\sim$770 days, while the 'Kaster' fault zone, which has a throw of the same magnitude showed a resistance of $\sim$190 days at this level (for locations, see Figure 2.7). The lowering of groundwater levels within the Erft Block resulted in hydraulic head differences of more than 50 m over the Rurrand Fault along the NW boundary of the Erft Block. The sealing capacities of the Rurrand Fault cause the gradual decline of groundwater levels in the Erft Block to have only a limited effect on the hydraulic head distribution within the Roer Valley Graben. Further south, directly adjacent to the 'Hambach' open-pit mine, the Rurrand Fault is segmented where relay zones are present which transfer strain between the fault segments [*Willemse et al.*, 1996]. This specific discontinuity in the Rurrand Fault is directly visible in the hydraulic head pattern of the Roer Valley Graben since at this location the extraction cone on the Erft Block continues into the Roer Valley Graben. Apparently, the sealing potential of the Rurrand Fault is strongly lowered by the segmentation structure. At this location groundwater flows through the relay zone between the fault segments into the Erft Block. Detailed mapping of hydraulic head patterns combined with the extensively available geological information over the area is needed to better explain the observed variation in hydraulic properties of the individual faults [*Wallbraun*, 1992, Chapter 5].

The spectacular hydraulic head gradients over the Rurrand Fault continue to exist as long as the flux is maintained through groundwater extractions. If these extractions will cease, the strong hydraulic gradient will reduce to a gradient that is in accordance with the natural groundwater flow distribution. The effect of the lignite mining activities on the hydraulic head in the deeper aquifers in the Nether-

lands is subject of ongoing research [*e.g. Stuurman*, 2000]. However, it is clear that due to the presence of the sealing faults in the mining area this effect is strongly attenuated.

In the Netherlands, groundwater extractions on the scale of that in the lignite mining area do not occur. Yet, the faults of the RVRS still have a considerable impact on groundwater flow and aquifer structure in the Netherlands, as will be shown in the next sections.

2.3.2 Field scale ($\sim$km)

The Gilze-Rijen Fault near the city of Tilburg

The Gilze-Rijen Fault forms the northward extension of the Feldbiss Fault Zone. An aerial photograph taken in the spring of 1997 near the city of Tilburg shows a section of the Gilze-Rijen fault, where it crosses farming land (Figure 2.4). The soil moisture distribution within the farming land is associated with the location of the fault trace. Dark colors NE of the fault represent a relatively higher soil moisture content. The Gilze-Rijen Fault Zone that separates the two different domains, is only a few meters wide. The soil map of the Netherlands [Figure 2.8; *STIBOKA*, 1985] shows that at the location of the aerial photograph (Figure 2.4) the fault line separates two different soil types.

On the footwall block, coarse sands occur at or near the surface (Sterksel Formation), while on the hanging wall at the eastern side of the fault fine sandy loams dominate (Nuenen Group). The same lithological contrast is found in a very detailed section that was made several kilometers to the south, on the terrain of the Water Supply Company of Tilburg [*De Glee and Brandenburg*, 1926]. The structure of the fault system in this area was further investigated by *Vandenberghe* [1982] and subsequently by *Van Zanten* [1996]. Both made use of geoelectrical prospecting methods in combination with borehole information. *Vandenberghe* [1982] showed that the Gilze-Rijen Fault is the easternmost fault of a set of faults that form the western boundary of the Roer Valley Graben. *Van Zanten* [1996] suggests that the Gilze-Rijen Fault consists of two closely spaced faults about 100 m apart. However, the soil map (Figure 2.8) and the more detailed aerial photograph of the area (Figure 2.4) suggest that a system of overstepping faults is a more likely scenario for the Gilze-Rijen Fault. In an overstepping system, relay zones, such as those observed in the lignite mining area in Germany, may cause discontinuities in the otherwise sealing behavior of faults. *Van Zanten* [1996] indeed showed a possible interaction between shallow and deeper groundwater along the faults located at the Tilburg

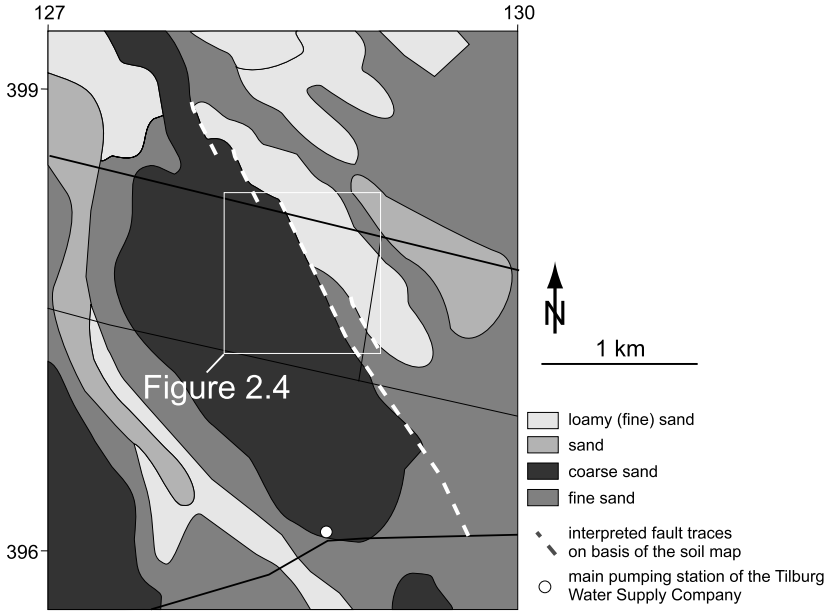

Figure 2.8: Detail of the soil map of the Netherlands [*STIBOKA*, 1985] that shows the overstepping structure of the Gilze-Rijen Fault Zone near the city of Tilburg; map coordinates are in thousands of meters in the Dutch coordinate system. The downthrown block is on the eastern side of the fault trace. The pattern of fault traces as interpreted on basis of the soil map does not fully match the fault traces as interpreted on the aerial photograph (Figure 2.4). Probably this discrepancy can be attributed to the uncertainties in the exact location of the borders between the different units on the soil map since these are interpreted on basis of point observations.

Water Supply area based upon tritium and chloride concentrations of water from deep aquifers. This may be explained by the occurrence of fault relay in the Gilze-Rijen Fault as discussed above.

Small fault near the village of Wanssum

During the late 1950s and the early 1960s research by the Institute of Land and Water Management Research (ICW) showed that faults on the Peel Block are associated with anomalous high hydraulic head gradients [*Bon*, 1968]. On the Venlo Block near the Maas River, a detailed hydrogeological profile based on boreholes and observation wells was constructed perpendicular to a secondary fault near the village

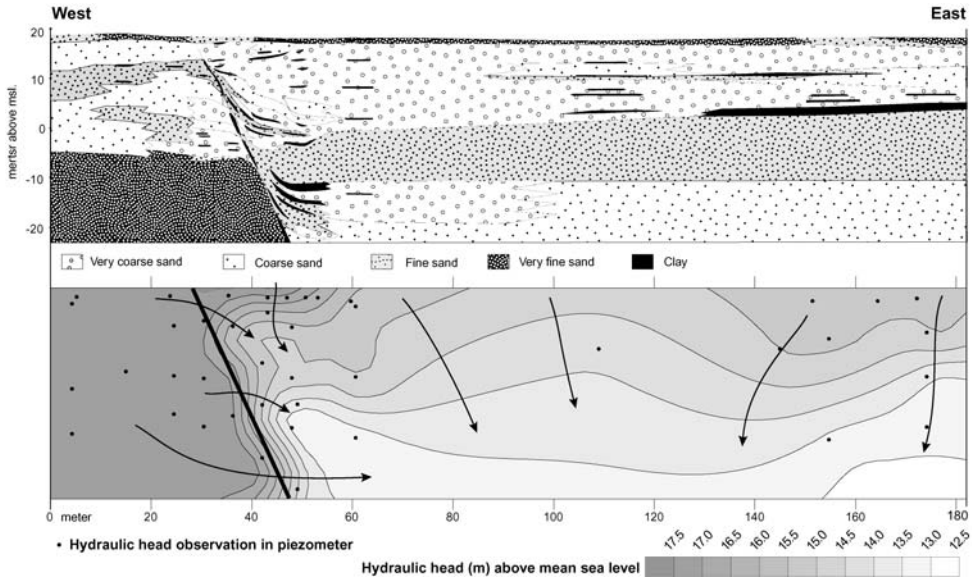

Figure 2.9: Hydrogeological section and associated hydraulic head patterns over a fault near the village of Wanssum [after *Ernst and De Ridder*, 1960, for location see Figure 2.2].

of Wanssum [for location see Figure 2.2; *Ernst and De Ridder*, 1960]. This study is probably the best-documented example in the Netherlands that shows the impact of a small fault on the local hydraulic head distribution (Figure 2.9). Moreover, it shows that extremely detailed observations are needed to properly characterize the hydrogeological buildup of a sealing fault zone. Also, the small spacing of observation wells shows that the fault zone is only limited to $5\,\mathrm{m}$ at most. *Ernst and De Ridder* [1960] estimated the specific resistance of this fault to be around 350 days based upon their field data.

The Peel Boundary Fault Zone near the village of Uden

A study on a similar scale was done in the late 1990s by *Stuurman and Atari* [1997] on the eastern boundary of the Peel Block, across the Peel Boundary Fault Zone near the village of Uden (Figure 2.2). Wet conditions prevail on the topographic high of the Peel Block. Peat bogs developed from the beginning of the Holocene. When even wetter and warmer climatic conditions caused the groundwater table to rise to the surface. This anomalous hydrological situation, with the wettest areas on the higher parts in the topography, was the motivation for earlier studies that

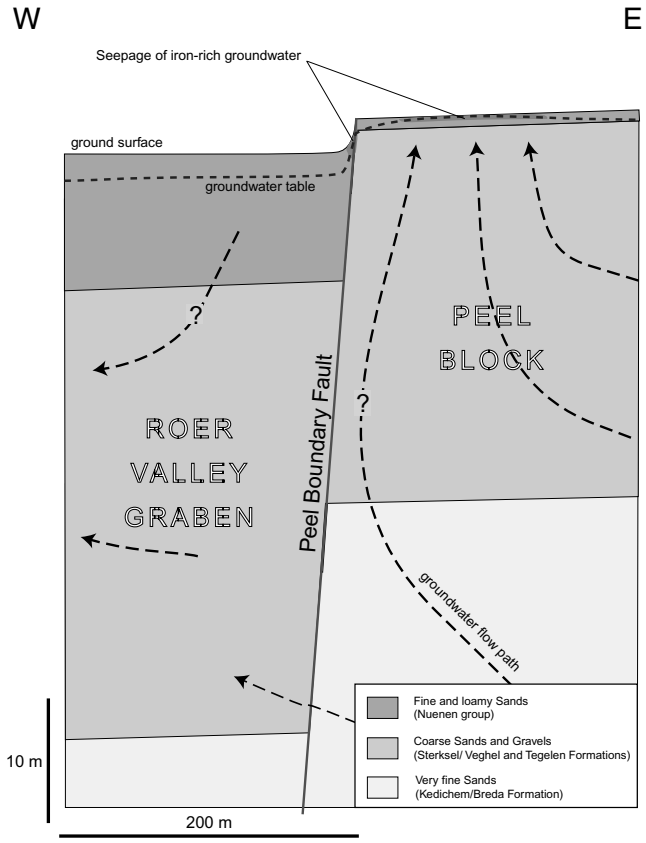

Figure 2.10: Schematized hydrogeological section over the Peel Boundary Fault Zone near the village of Uden [compiled after *Stuurman and Atari*, 1997, for location see Figure 2.2].

focused on an improvement of the problematic water management of these areas [*e.g. Visser*, 1948].

A schematized hydrogeologic section (Figure 2.10) shows how east of the Peel Boundary Fault Zone and along the fault scarp, iron-rich groundwater is discharging and is oxidized as soon as it approaches the surface. This process leads to iron-cemented sands and silts at these locations. At the surface, the Peel Boundary Fault Zone forms a topographic scarp of about $3\ \mathrm{m}$. The hydraulic head difference across the fault zone is about three meters, in the first aquifer below the phreatic zone. The width of the fault zone is estimated from lithological sections in *Stuurman and Atari* [1997], as five meters. The main aquifer is formed by fluvial sands and gravels

of mid-Pleistocene age (Veghel and Sterksel formations). On the Peel Block, these sediments overlay fine-grained marine sands of Miocene age (Breda Formation). In the Roer Valley Graben the hydrological base is formed by clays of Pleistocene age (Kedichem Formation). On top of this system silts and fine sands of aeolian origin were deposited during the Saalian and Weichselian (Nuenen Group). These latter deposits form the upper, phreatic aquifer. As a result of a faulted topography, the aeolian deposits are about 15 meters thicker in the Roer Valley Graben than on the higher Peel Block.

Although iron-cementation as observed along the Peel Boundary Fault Zone probably led to a strong reduction of its permeability, this phenomenon is limited to the upper oxygen rich part of the aquifer and therefore cannot explain the high resistance of the Peel Boundary Fault Zone at larger depths, as indicated by the large drop in hydraulic head over the fault. Probably, mechanisms like clay smearing and juxtaposition of aquitards and aquifers will play an important role at those depths.

The resistance of the Peel Boundary Fault Zone can be calculated by analysis of the hydraulic gradients on the Peel Block (i_{PB}), Roer Valley Graben (i_{RVG}) and over the Peel Boundary Fault Zone (i_f). The first two gradients, i_{PB} and i_{RVG} are directly estimated from the hydraulic head distribution in the main aquifer (Figure 2.11) as: $1.2 \cdot 10^{-3}$ m/m and $0.4 \cdot 10^{-3}$ m/m respectively. If the Peel Boundary Fault Zone is fitted in and a fault zone width of 5 m is assumed, i_f follows as $640 \cdot 10^{-3}$ m/m. The Groundwater Map of the Netherlands [*TNO-NITG*, 1974a] indicates that the main aquifer on the Peel Block has a transmissivity value of around 1100 m^2/day.

Two situations for the transmissivity distribution in the model are considered: (1) the contrast in gradient between the aquifer on the Peel Block and the Roer Valley Graben is fully explained by a difference in transmissivity between the two blocks; and (2) the same contrast is completely explained by assuming discharge in the fault zone while the transmissivities in the Peel Block (KD_{PB}) and Roer Valley Graben (KD_{RVG}) are considered to be equal. In either case the transmissivity of the Peel Block is fixed at 1100 m^2/day.

- When the observed gradients are fitted in the first case (no discharge in the fault zone), it follows from equation 2.6 that KD_{RVG} must equal 3300 m^2/day in the case that KD_{PB} equals 1100 m^2/day. The transmissivity of the Peel Boundary Fault Zone ($K_f D_f$) is about 2.1 m^2/day. The equivalent fault resistance in this case follows from equation 2.4. If D_f is estimated as 25 m (from

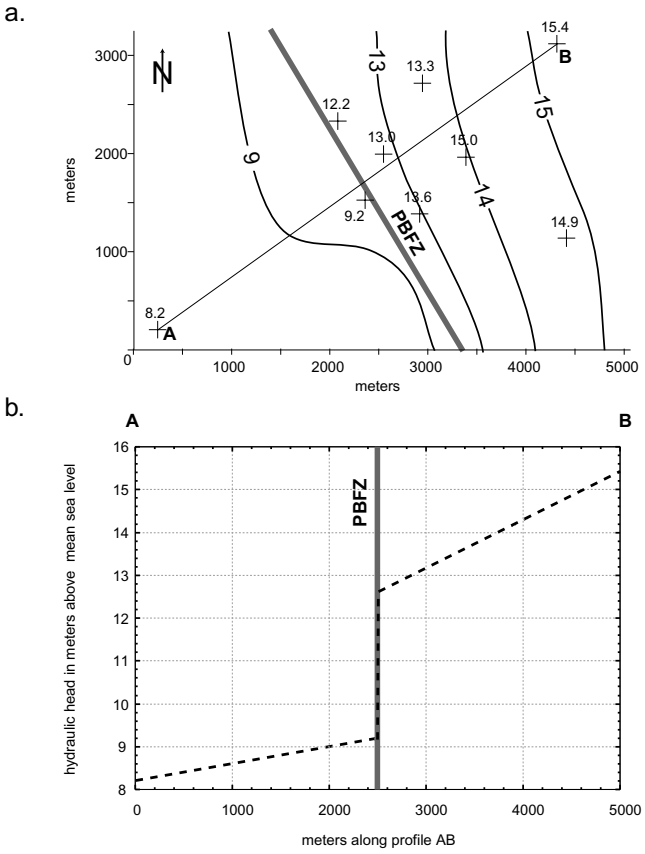

Figure 2.11: *a*) Hydraulic head distribution (above mean sea level) in the main aquifer near the Peel Boundary Fault Zone (PBFZ) near the village of Uden (average over 1995) in map view. Isohypses of hydraulic head are based on modeling results by *Stuurman and Atari* [1997]. *b*) The shift of hydraulic gradient over the Peel Boundary Fault Zone in cross section (A-B).

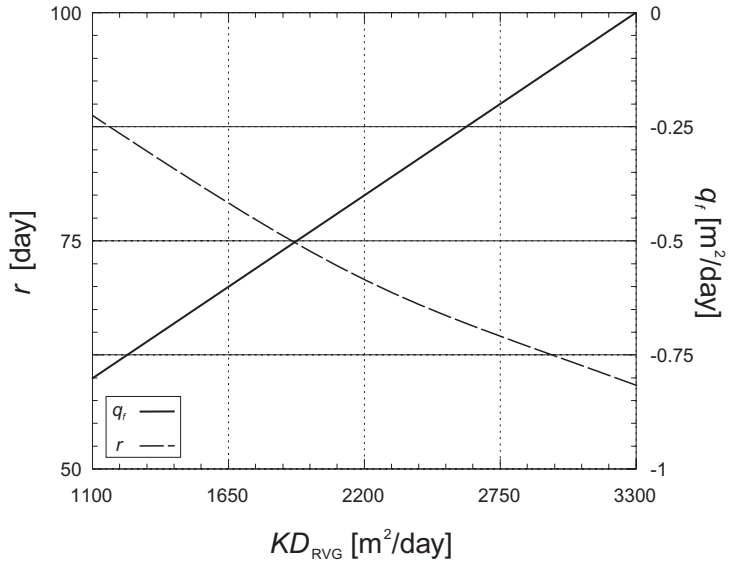

Figure 2.12: Relation between the transmissivity in the Roer Valley Graben (KD_{RVG}), fault resistance (r) and the specific discharge (q_f) in the Peel Boundary Fault Zone. The transmissivity of the aquifer on the Peel Block (KD_{PB}) is assumed to be $1100\ \mathrm{m}^2$ / day.

Figure 2.10) and the width of the fault zone (w) as $5\ \mathrm{m}$, the equivalent fault resistance r equals 59 days.

- In order to explain the observed difference in hydraulic gradient in the second case, assuming that $KD_{RVG} = KD_{PB} = 1100\ \mathrm{m}^2$ / day on either side of the Peel Boundary Fault, groundwater fluxes must be different between the two blocks. The difference can be explained by incorporating discharge in the fault zone by following equation 2.7. It follows that the specific discharge (q_r) *i.e.* the product of R and w, in the Peel Boundary Fault Zone must be $0.9\ \mathrm{m}^2$ / day. In the latter case, KD_f is found to be around $1.4\ \mathrm{m}^2$ / day (89 days). In the area on the Peel Block close to the Peel Boundary Fault Zone, discharge is observed as surface seepage.

The two cases as described above, can be considered as two end-members of a range of possible hydraulic parameters that can explain the observed hydraulic head gradients. Figure 2.12 shows the relation between the calculated values of the specific discharge over the fault zone (q_f), resistance of the fault zone (r) and the transmissivity in the Roer Valley Graben (KD_{RVG}) in the interval

$1100 - 3300\ \mathrm{m^2}$ / day. The fault resistance of around 75 days that follows from gradient analysis implies that the hydraulic conductivity (K_f) of the fault zone material is about 0.1 m / day. The undeformed material of the main aquifer has an estimated conductivity of around 60 m / day. This implies that the fault zone material has a hydraulic conductivity that is reduced with more than 2 orders of magnitude. A one-dimensional gradient analysis, as carried out above, provides a first estimate of fault zone hydraulic properties. The resistance of around 75 days for the Peel Boundary Fault Zone, that was found in the above analysis, is in contrast to the value of 1500 days that was inferred by *Stuurman and Atari* [1997] based on a numerical model of the system. This discrepancy is probably due to the fact that the numerical model incorporates more terms than horizontal groundwater flow only. More research is needed to elucidate the relative contribution of these variables in order to bring both models in closer agreement.

The Peel Boundary Fault Zone near the village of Neer

Near the village of Neer, a trench was opened over the Peel Boundary Fault Zone in the framework of paleo-seismological studies [*Van den Berg et al.*, 2002]. Here, in-situ observations on the micro-morphology of the fault zone were made in combination with a detailed profile of the hydraulic head gradients over the fault zone in the upper phreatic aquifer (Figure 2.13a & b). The top layer consists of fine-grained fluvio-aeolian sands (Nuenen Group) with a thickness of ~ 8 m.

The Peel Boundary Fault Zone has a small fault scarp in the topography but this is far less pronounced than it is near the village of Uden. The observations in the trench show that the fault is limited to a one meter wide zone at this shallow depth. Over this distance, going from the Peel Boundary Fault Zone into the Roer Valley Graben, the phreatic groundwater level drops about 15 cm. Just below the groundwater table in the trench, massive iron concretions were found along the fault plane. Similar to the situation near Uden, these iron concretions indicate that near the fault reduced groundwater discharges to the surface where it is subsequently oxidized. Therefore, these concretions are probably only limited to the zone close to the groundwater table.

Coarse sands and gravels (Veghel Formation) form the regional main aquifer below silts and fine sands (Nuenen Group). According to the groundwater map of the Netherlands [*TNO-NITG*, 1974b], in this area, hydraulic heads in the phreatic top layer are closely coupled to the hydraulic heads in the underlying aquifer. The direction of regional groundwater flow can at first instance be estimated from the same map; this indicates that near the trench, groundwater flow is semi-parallel

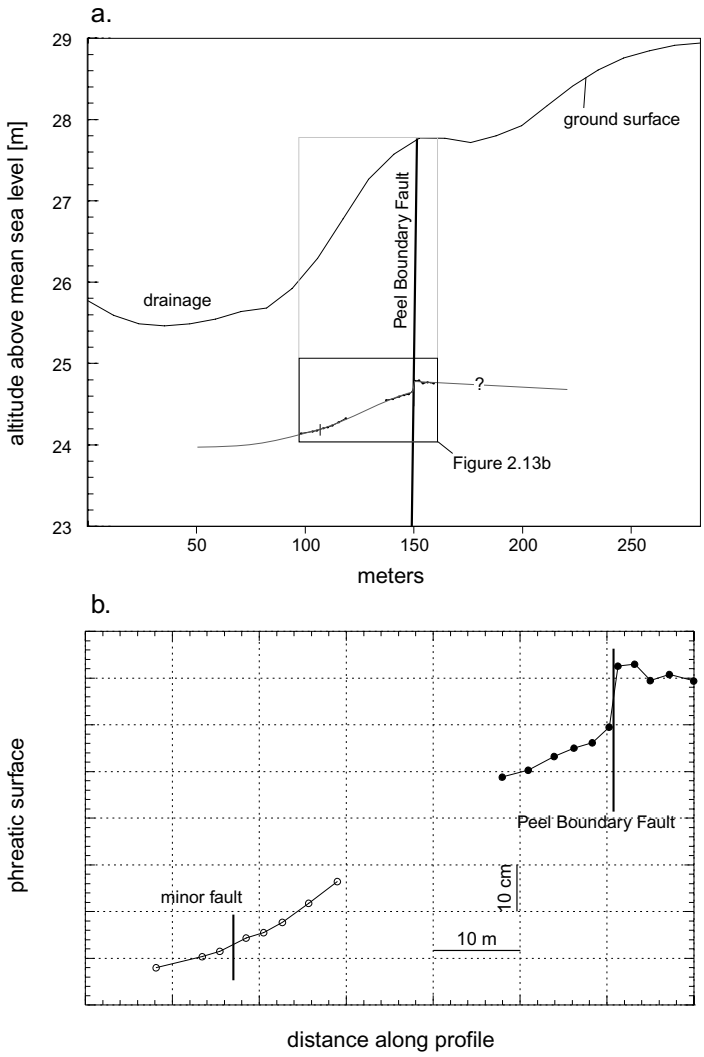

Figure 2.13: Section of groundwater levels over the Peel Boundary Fault Zone near the village of Neer; for location see Figure 2.2. Observations were done in shallow boreholes in a trenched outcrop.

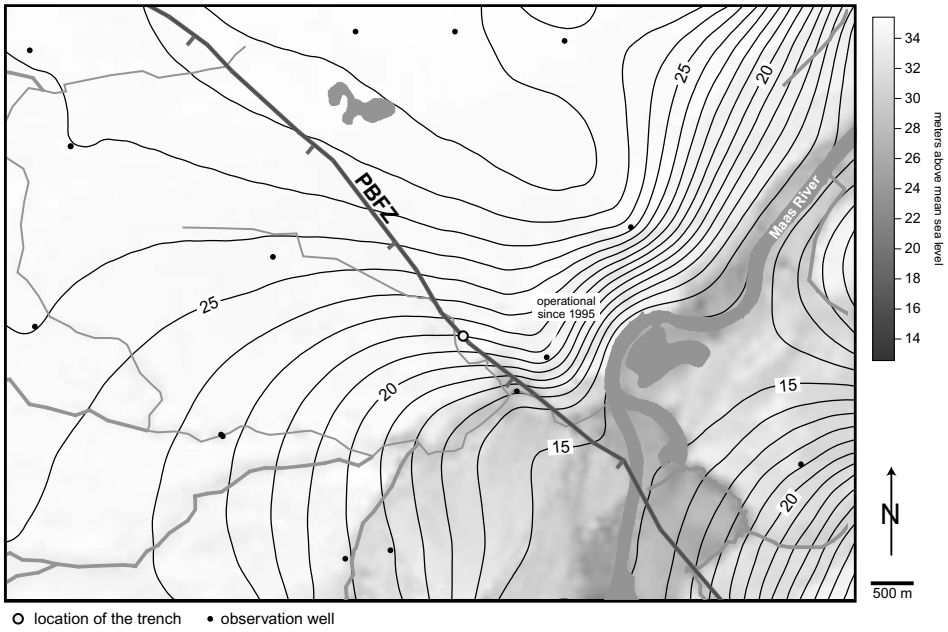

Figure 2.14: Regional groundwater flow pattern superimposed on the topographic height of the area, in the vicinity of the site of Figure 2.12 (Peel Boundary Fault Zone=PBFZ). This shows that the primary control on the direction of groundwater flow is the discharge to the Maas River with a possible local deflection across the southern side of the PBFZ.

to the Peel Boundary Fault Zone. However, one observation well that was placed more recently (Figure 2.14) was not yet operational during the compilation of the groundwater map. Inclusion of this new data point allows for a somewhat different interpretation of the flow pattern; it suggests that flow is likely to be more oblique to the Peel Boundary Fault Zone. The uncertainty on the direction of groundwater flow near the fault zone makes it difficult to place the small-scale observations in a larger regional scale context.

The section of phreatic groundwater levels as recorded perpendicular to the Peel Boundary Fault Zone (Figure 2.13b) suggests that the fault zone acts as a groundwater divide at this shallow depth, since groundwater flow is away from the fault zone on both sides of the fault. The gradient of groundwater flow on the footwall block is very small, while on the hanging wall the gradient is significant. If groundwater flow is assumed more or less perpendicular to the fault zone, recharge of groundwater must take place close to or in the fault zone. Observations on the

trench walls show that recharge may indeed take place on the Peel Block, in a zone flanking the main fault plane. There, conjugate sets of small cm-wide deformation bands have developed as a result of fault activity. These deformation bands have a spacing of about $50\ \mathrm{cm}$ and their occurrence extends about two meters onto the footwall. Also, these small deformational structures are internally bleached which is interpreted to indicate that they form preferential paths to vertical infiltration of water [*Miedema and Jongmans*, 2002].

If a hydraulic conductivity of around $10\ \mathrm{m/day}$ is assumed for fine sand, a transmissivity value of $80\ \mathrm{m^2/day}$ follows for the upper phreatic aquifer. The thickness of this top layer does not significantly change across the fault zone at this location. So, the transmissivity of the aquifers on either side of the fault zone is assumed to be $80\ \mathrm{m^2/day}$. A fit of the observed hydraulic heads (Figure 2.15), using an analytical equation [from *Haneberg*, 1995] which is a solution to 2.7, assuming a fault zone width of one meter based on observations in the trench, shows that the fault resistance must be around $4\ \mathrm{days}$ while the fault zone has a specific recharge of $1\ \mathrm{m^2/day}$. This fault resistance value is far less than observed at the site near the village of Uden. This is reasonable, since the fault resistance is considered in the upper aquifer only. Probably, fault resistance will increase with depth since the effectiveness of most important fault sealing mechanisms is based on the amount of throw along the fault plane in combination with depth.

2.4 Discussion and conclusions

The impact of faults on groundwater movements in an active rift system like the Roer Valley Rift System is clearly demonstrated in the lignite mining area in Germany where strong groundwater extraction enhances their effects. Studies in the Netherlands which show the influence of faults are sparse. This is because only detailed mapping of the hydraulic head distribution can reveal locally anomalous high or low hydraulic head gradients. Examples from previous research show that faults may have a pronounced effect on aquifer structure on regional as well as on local scale. This notion may be essential to studies related to groundwater management, groundwater contamination and its environmental impact. In order to improve groundwater flow models, the exact relationship between tectonic structures (*i.e.* faults) and hydrogeology needs to be clarified. Therefore, more extensive and quantitative analysis of the impact of faulting on the hydrogeological buildup of the RVRS is needed, from regional to field scale. Regionally important faults in the Roer Valley Rift System, like the Feldbiss and Peel Boundary Fault Zones have an obvious regional hydrogeological impact since they separate larger hydro-

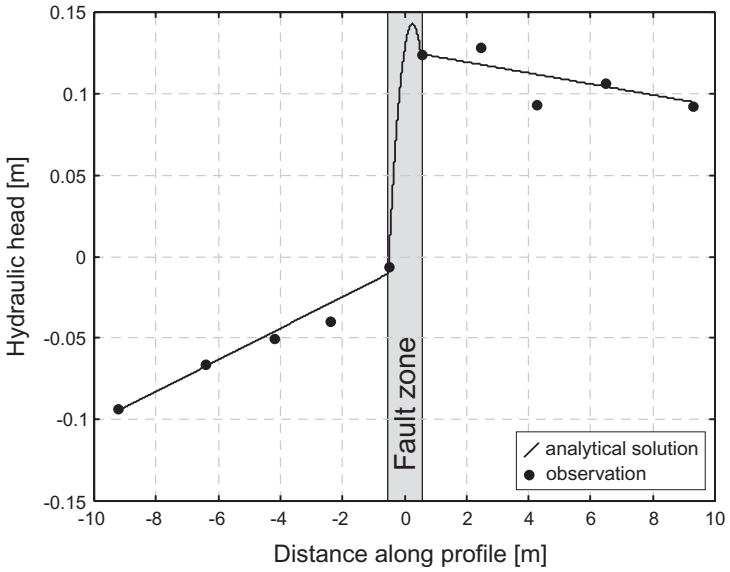

Figure 2.15: Fitted hydraulic head profile over the observed data in the trench using an analytical solution. To explain the observed gradients a specific recharge of the Peel Boundary Fault Zone of around $1\ \mathrm{m}^2$/day is needed in combination with a fault resistance of 4 days ($D_f = 8\ \mathrm{m}$). The transmissivity of the flanking aquifers is here assumed to equal $80\ \mathrm{m}^2$/day. Hydraulic head values are normalized so that the hydraulic head losses on the left and right-hand side of the origin of the system are equal.

geological units. The effect of individual smaller faults is more difficult to assess. Smaller secondary faults will be more frequent and therefore will probably have a strong cumulative effect on internal aquifer structure and small-scale groundwater systems. Observation wells are often too widely spaced to give sufficient information to make a reconstruction of the flow pattern near faults. It is expected that the cumulative effect of a set of small faults, all having a similar orientation that is induced by the regional tectonic stress field, should result in a regional anisotropy of hydraulic conductivity. Thorough analysis of pumping tests or dense groundwater monitoring networks would be needed to reveal such a regional anisotropy. Hydraulic head patterns and their fluctuation over time should give information on the underlying geological buildup of an area and could reveal structures that would otherwise be difficult to detect. However, recognition of steps in the hydraulic head profile resulting from faults, requires detailed information because these kind of subtle jumps in hydraulic head are easily overlooked when data are interpo-

lated. An important conclusion of the present analysis is that faults in the RVRS can form strong barriers to horizontal groundwater flow while vertical groundwater flow may be enhanced. In this scenario, the internal hydrogeological build-up of fault zones is thus strongly anisotropic. At the location of faults normally separated aquifers can be hydraulically coupled which makes the vertical interchange of groundwater between these aquifers possible. This sort of mechanism can have important implications to the spread of contaminated groundwater which may intrude into other aquifers through vertical flow along faults.

3

The internal hydrogeological structure of the Geleen Fault

Abstract

In general, faults cutting through the unconsolidated sediments of the Roer Valley Rift System (RVRS) form strong barriers to horizontal groundwater flow. The relationships between deformation mechanisms along fault zones and their impact on the hydrogeological structure of the fault zone are analyzed in a shallow (0-5 m below land surface) trench over one of the faults in the study area. Recently developed digital image analysis techniques are used to estimate the spatial distribution of hydraulic conductivity at the millimeter-scale and to describe the micro-morphologic characteristics of the fault zone. In addition, laboratory measurements of hydraulic conductivity on core-plug samples show the larger scale distribution of hydraulic conductivity in the damage zone flanking the main fault plane. Particulate flow is the deformation mechanism at shallow depths, which causes the damage zone around the fault, in the sand-rich parts, to have a relatively enhanced hydraulic conductivity. The fault core is characterized by reduced hydraulic conductivity due to clay smearing, grain-scale mixing, and iron-oxide precipitation.

This Chapter is largely based upon: Bense, V.F., Van den Berg, E.H. and R.T. Van Balen, Deformation mechanisms and hydraulic properties of fault zones in unconsolidated sediments; the Roer Valley Rift System, the Netherlands. *Hydrogeology Journal, 11*, 319-332, 2003.

3.1 Introduction

Fault zones can act as barriers or preferential flow paths to fluid flow [*e.g. Knipe,* 1993; *Rawling et al.*, 2001; *Bense et al.*, 2003a]. Fault-zone properties can vary over time, being correlated to episodic changes in the stress regime [*Sibson,* 1981, 2000] or else by truncation / reconnection of aquifers along faults over time [*Mailloux et al.*, 1999]. Faults play a crucial role in the distribution of hydrocarbons because of their capacity to act as seals [*e.g. Bouvier et al.*, 1989; *Møller-Pedersen and Koestler*, 1997; *Smith,* 1980]. Since hydrogeological studies are generally more focussed at shallow depths as compared to studies related to hydrocarbon recovery, there has been less attention paid to the impact of faults on groundwater flow. Recently, *Bense et al.* [2003a] have shown that faults can strongly impact groundwater-flow systems on both regional and local scales. This Chapter aims to contribute to the sparse description and limited understanding of the hydraulic properties of faults in unlithified sediments at shallow depth.

In the Netherlands, poorly consolidated sediment systems constitute the aquifers from which a large part of the Dutch water-supply network extracts its drinking water. In the southeastern part of the Netherlands, these sedimentary aquifers are cut by a set of faults that belong to the Roer Valley Rift System (RVRS) which extend into adjacent areas in Germany and Belgium (Figure 3.1). The results of an outcrop-scale study of the hydrogeological structure of the Geleen Fault (Figure 3.1) are presented in this Chapter. The spatial distribution of hydraulic conductivity is estimated from thin sections of the sediments by application of recently developed image-analysis techniques [*Van den Berg et al.*, 2002, 2003]. The results of the image analysis procedure are compared with laboratory measurements of hydraulic conductivity on several core plugs.

In the first part of this Chapter, a summary of the models that have been proposed in the literature is presented, together with an overview of the deformation mechanisms that play a role in fault-zone formation as a function of burial depth and petro-physical properties of the deformed rock. In the subsequent section, the geological setting of the study area is briefly discussed and the impact of faults on the hydrogeologic system of the RVRS is illustrated with examples from earlier work. Finally, the observations in the trench will be presented and discussed in the light of these existing models, and the techniques which are used in this study are evaluated.

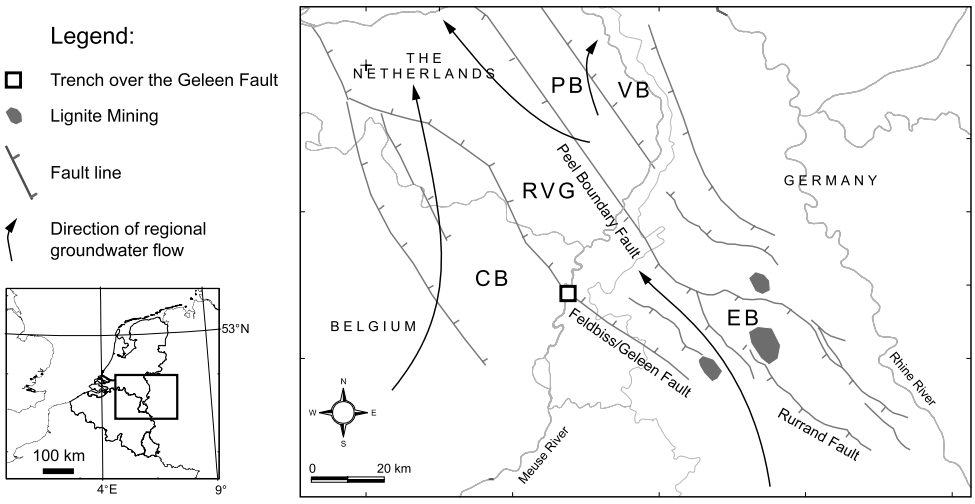

Figure 3.1: Geographic location of tectonic blocks, important faults and fieldwork area within the RVRS (CB = Campine Block, RVG = Roer Valley Graben, PB = Peel Block, VB = Venlo Block, EB = Erft Block). Regional location of study area shown on left.

3.2 Deformation processes within the fault zone

3.2.1 Deformation mechanisms in sand

In clean sand consisting mostly of grains (*i.e.* $<10\ \%$ clay), three deformation mechanisms as a function of burial depth and bulk porosity can be distinguished, namely: *1*) cataclasis, *2*) particulate flow and *3*) cataclastic flow. Cataclastic flow operates at large depths, therefore only the first two mechanisms are relevant in this study and are discussed.

The relation between the mode of deformation and both bulk porosity and burial depth is depicted in Figure 3.2, based on *Fulljames et al.* [1997].

Cataclasis is the crushing of sand grains resulting in a relative increase of finer-grained material. According to the map of deformational features (Figure 3.2), cataclasis is the most common deformation mechanism at depths greater than about $1\ \mathrm{km}$. As a result of cataclasis, deformation bands evolve in sands as a single slip-plane, and following increasing strain, to zones of deformation bands [*e.g. Antonellini and Aydin*, 1994; *Aydin and Johnson*, 1978]. Direct field measurements using portable air-permeameters [*Antonellini and Aydin*, 1994; *Pittman*, 1981] and indirect estimates of hydraulic conductivity [*Lansing Taylor and Pollard*, 2000], have shown

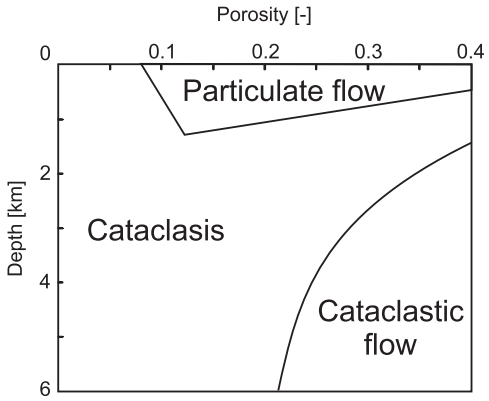

Figure 3.2: Deformation mechanisms of clean sands as a function of porosity and depth [after *Fulljames et al.*, 1997].

that deformation bands in sandstones have a hydraulic conductivity that is reduced by two to more than seven orders of magnitude relative to the host sediment. Laboratory work [*Arch and Maltman*, 1990] and field studies of rigid sandstones [*Antonellini and Aydin*, 1994] show that the reduction of hydraulic conductivity perpendicular to the deformation band is often larger than along strike. Therefore, the distribution of hydraulic conductivity in and around deformation bands in this case is strongly anisotropic.

At shallow depth, less than about $500 - 1000\,\mathrm{m}$, particulate flow rather than cataclasis will be the dominant deformation mechanism (Figure 3.2). As a result of particulate flow, the grains roll past each other without crushing, while the pores within the zone of deformation tend to dilate. Particulate flow also disaggregates the grain fabric. *Fulljames et al.* [1997] state that if no significant diagenesis takes place, the resulting fault gouge has properties not significantly different from the surrounding matrix. This is in contrast to cataclastic processes, described above, that result in a fault gouge with a greatly reduced hydraulic conductivity.

Cataclasis and particulate flow should be regarded as two end members in a spectrum of deformation mechanisms, since the transition with depth from cataclasis to particulate flow is probably more gradual than suggested in Figure 3.2. For example, cataclasis and particulate flow will operate simultaneously when the smaller grains of a sediment can break under the given pressure conditions while the larger grains are too strong and will continue to slide along each other through particulate flow, without breaking.

If the sand contains more than $\sim 10\%$ clay, the result of the deformation will probably always be a reduction in hydraulic conductivity due to the occurrence of a process named ”deformation induced mixing” [*Gibson*, 1998]. This process

involves the compaction and mixing of clay with sand grains, resulting in a more homogeneous distribution of clay than in the undeformed sediment and, therefore, lower bulk porosity.

Clay smearing

Clay smearing is a process that can strongly reduce the effective hydraulic conductivity of a fault zone. In sedimentary successions where clay or shale layers are present, dragging or ductile flow of these layers along the fault plane between the up- and down-thrown source beds, can result in a clay smear along the fault plane [*Fulljames et al.*, 1997; *Smith*, 1980]. Field studies that describe the mechanisms of smearing in more detail have been reported by *Lindsay et al.* [1993] and *Lehner and Pilaar* [1997]. The work of the last authors is based on observations in the German lignite mines that are operated within the RVRS in our study area.

Diagenesis

A diagenetic process like the precipitation of minerals composed of, for example, iron (Fe), or manganese (Mn) oxides, or calcite ($CaCO_3$), can cement an originally permeable fault plane until porosity is partially or almost completely removed [*Knipe*, 1993; *Leveille et al.*, 1997]. *Chan et al.* [2000] show that along the Moab fault zone in southeastern Utah, USA, mobilization and redistribution of iron can occur in multiple episodes related to phases of fluid flow along the fault. *Mozley and Goodwin* [1995] described cementation patterns that reflect palaeoflow directions in unconsolidated sediments.

3.2.2 Hydrogeological fault zone models

Several fault-zone models have been proposed in which the above-described mechanisms and processes are integrated. Evidently, the variation of deformation mechanisms with depth must be reflected in fault-zone models. These models should have a hydrogeological structure as a function of depth. There is however a general consensus about the architectural elements that a fault-zone model should contain. These architectural elements will be discussed below.

Caine et al. [1996] propose on the basis of numerous field studies, laboratory experiments, and numerical-flow models in and near fault zones, that in general the fault zone is built up of three architectural elements, *1*) fault core; *2*) damage zone; and *3*) protolith (undeformed host rock) (Figure 3.3). Although *Caine et al.*

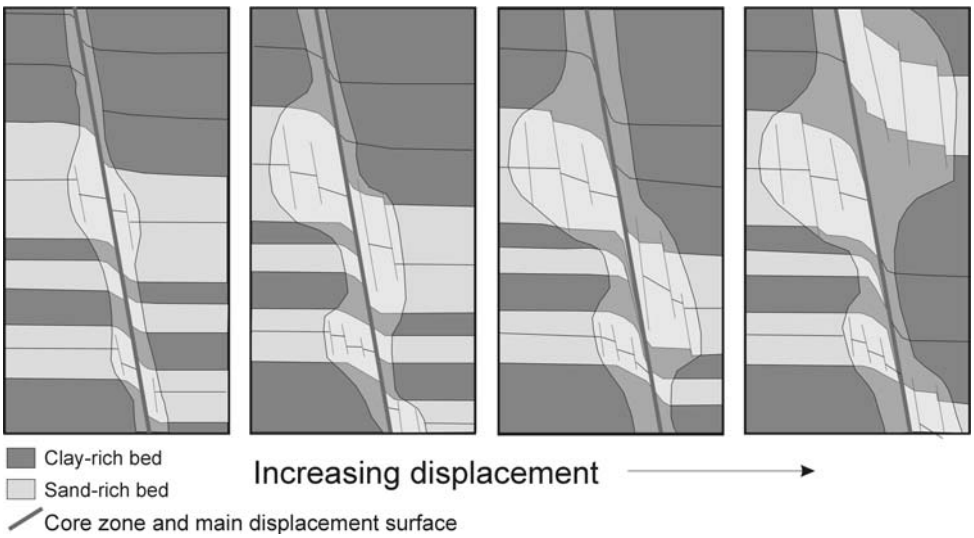

Figure 3.3: Generalized cross-section of fault-zone model showing fault core, damage zone, and protolith [after *Heynekamp et al.*, 1999].

[1996] developed their model of the structural architecture and hydraulic behavior of fault zones for strongly lithified sedimentary deposits and crystalline rocks, this model provides the framework for the construction of models that apply to unconsolidated sediments [*e.g. Heynekamp et al.*, 1999; *Rawling et al.*, 2001].

The fault core is defined as the portion of the fault zone that is the locus of most shear deformation. The damage zone forms the intermediate region between the fault core and the undisturbed protolith. Within damage zones in sandstones, normally most of the deformation is accommodated by the formation of fracture networks and the development of deformation bands, while in the fault core, fracture density is far less [*Andersson et al.*, 1983; *Chester et al.*, 1993].

The hydraulic conductivity of the fault core is dominated by grain-scale permeability changes (*e.g.* cataclasis, shale- or clay smearing) of the faulted rocks and the fault core will therefore normally act as a strong barrier to fluid flow. In the damage zone the spatial distribution of hydraulic conductivity is determined by the hydraulic properties of the fracture- and deformation-band network.

In consolidated rocks, open fractures can enhance the permeability in the damage zone. Conceptually, these types of fault zones are conduits to fluid flow along the fault plane and barriers to flow perpendicular to the fault. *Evans et al.* [1997] show that an increase in bulk hydraulic conductivity of about three orders of mag-

nitude, as a minimum, occurs in damage zones that contain open fractures. If extensive interconnected fracture networks are present, this permeability enhancement can even be several orders of magnitude stronger. One should keep in mind, however, that clean sandstones which are not cemented by early diagenesis will probably be loose and poorly consolidated until they reach a depth of about three kilometer [*Sverdrup and Bjørlykke*, 1997]. Only at greater depths will the rocks have a brittle behavior and will probably be able to support open-fracture networks that are likely to evolve during uplift and unloading due to a reduction of the confining pressure [*Sverdrup and Bjørlykke*, 1997]. Therefore, *Heynekamp et al.* [1999] and, subsequently, *Rawling et al.* [2001] argued that damage zones along faults in unconsolidated sediments do not contain open-fracture networks, but that cataclastic-deformation bands are the main elements in the damage zone (Figure 3.3). The last authors referred to further suggest that in contrast to fault zones in consolidated rock, mixing and rotation of grains at the grain-scale takes place resulting in the development of a mixing zone that is intermediate between the damage zone and fault core. The mixing process of sand and clayey material results in a porosity reduction of the grain fabric [*Heynekamp et al.*, 1999]. *Rawling et al.* [2001] show that large-displacement faults in poorly lithified sediments have little potential as vertical-flow conduits and have a stronger effect on horizontal flow than faults containing open fractures.

3.3 Regional geology and hydrogeology of the study area

The Roer Valley Rift System (RVRS) is located in the southeastern part of The Netherlands, the northeastern part of Belgium, and adjacent parts of Germany (Figure 3.1). The RVRS is a rift system in the southeastern part of the North Sea Basin - the Lower Rhine Embayment - which is part of a Cenozoic mega-rift system that crosses western and central Europe [*Ziegler*, 1994]. The RVRS has a complex Mesozoic and Cenozoic tectonic history, comprising several extension and inversion phases. The current extension phase started during the Late Oligocene [*Geluk et al.*, 1994]. The RVRS comprises the northern part of the Campine Block in the south, the Roer Valley Graben in the center, the Peel Block, and the Venlo Block in the northeast (Figure 3.1). The Roer Valley Graben is separated from the adjoining blocks by the Feldbiss Fault Zone in the south and the Peel Boundary Fault Zone in the north, which were the most active fault zones during the Quaternary [*e.g. Houtgast and van Balen*, 2000]. The central Roer Valley Graben is filled with up to

$1200\ \mathrm{m}$ of sediments of Late Oligocene - Recent age, comprising fine-grained marine deposits overlain by a relatively thin sequence (less than $50\ \mathrm{m}$) of medium- to coarse-grained fluvial-deltaic deposits of Pleistocene age. The same sequence has a total thickness of up to $200\ \mathrm{m}$ on the Peel Block [*Geluk et al.*, 1994]. The coarse-grained fluvial deposits in the top of the sequence form the main aquifer in this area. The direction of regional groundwater flow is indicated in Figure 3.1.

Regionally extensive faults in the RVRS, like the Feldbiss and Peel Boundary Fault Zones have an obvious regional impact on the hydrogeology since they separate relatively large hydrogeological units. For example, the low conductivity of the Rurrand Fault (Figure 3.1) is of crucial importance for the planning of the large-scale lignite mining in the German part of the RVRS. Mining is concentrated on the west part of the Erft Block where $\sim 1.5 \cdot 10^9 \mathrm{m}^3$ / year of water is extracted to facilitate mining to a depth of more than $500\ \mathrm{m}$ in open pits [*Wallbraun*, 1992]. The Rurrand Fault is locally supporting hydraulic-head differences of more than $100\ \mathrm{m}$ [*Wallbraun*, 1992]. The effect of individual smaller faults is difficult to assess but smaller secondary faults will be more numerous and therefore will probably have a strong cumulative effect on the internal aquifer structure and on small-scale groundwater systems. Some of these small-scale faults may have a reduced hydraulic conductivity, others may have unchanged properties or their hydraulic conductivity may even have increased as a result of faulting. Studies in The Netherlands which show the influence of faults on the hydrogeology are sparse, probably because only detailed mapping of hydraulic heads can reveal anomalous hydraulic-head gradients which are often associated with faults. *Bense et al.* [2003a] give an overview of field examples of the hydrological conditions around several faults in the RVRS. In this Chapter, the hydrogeological characteristics of the Geleen Fault Zone are discussed as studied in a trenched outcrop. The Geleen Fault Zone is part of the Feldbiss Fault Zone (Figure 3.1).

3.4 Methodology

Image analysis and direct measurement of hydraulic conductivity on core plugs are applied to assess the spatial distribution of hydraulic conductivity around the Geleen Fault. The image-analysis technique is largely based on a method developed by *Van den Berg et al.* [2003] and is briefly described below.

3.4.1 Digital image analysis

3.4.2 Sampling procedure and preprocessing of images

Box-core samples ($10 \times 8 \times 4$ cm) are taken by carefully pushing a box core into the trench wall after the material around it was carefully removed in order to reduce disturbance of the sampled sediment. The box-core samples are air-dried for six to eight weeks and subsequently impregnated with blue epoxy resin. Thin-sections with a standard thickness of ~ 25 mm are prepared and digitally scanned (~ 80 pixels / mm) using transmitted light. Within the resulting image 'training-areas' are defined from which the spectral information is extracted that is used to classify each pixel in the image as either 'pore space' or 'grain'. Based upon the training areas a Standard Maximum Likelihood classification is carried out using a remote sensing software package. This procedure outputs a binary image wherein pore space and grains are separated. The ratio of pore space to the total area of the image gives a direct estimate of the porosity (ϕ [-]) of the sample material. The individual grains in this binary image are separated from each other using the Digital Cutting Method (DCM) [*Van den Berg et al.*, 2002]. The DCM makes it possible to estimate values for specific surface area per unit grain volume (S_{sp} [m^{-1}]). Calculations are done by sampling in non-overlapping windows with a pre-specified dimension across a regular grid. The minimum size of this sampling window is found by estimating the minimum Representative Elementary Area (REA) [*Buchter et al.*, 1994] that can be considered the highest resolution at which a specific property can be sampled.

3.4.3 Estimation of hydraulic conductivity

Using ϕ and S_{sp}, an estimate for the average intrinsic permeability (k [m^2]) is calculated for each window by application of the well-known, semi-empirical, Kozeny-Carman relationship [*e.g. Tiab and Donaldson*, 1996], resulting in:

$$k = \left(\frac{1}{K_z {S_{sp}}^2} \right) \frac{\phi^2}{(1-\phi)^3} \tag{3.1}$$

where K_z [-] is the so-called Kozeny-factor that was reported by Carman to be close to five for most porous materials [*Bear*, 1972] and which is the value used in the calculations. Hydraulic conductivity (K [$\mathrm{m/s}$]) for water is then found by the relation:

$$K = k \frac{\rho_w g}{\mu} \tag{3.2}$$

where the gravitational acceleration constant $g = 9.81\mathrm{m/s^2}$; the dynamic viscosity of water (at 13 °C) $\mu = 1.22 \cdot 10^{-3}$ $\mathrm{Ns/m^2}$ and the density of water $\rho_w = 1000$ $\mathrm{kg/m^3}$. In the following sections, K is presented in units of $\mathrm{m/day}$.

Accuracy of the image analysis procedure

The value of K, as calculated from a 2-D digital image of a thin section, should be considered only as an estimate of the real hydraulic properties of the sampled sediment. The Kozeny-Carman equation is used as a semi-empirical model in which uncertain sediment characteristics, for example tortuosity, are lumped into the Kozeny factor (K_z). Moreover, caution should be applied when comparing the estimated average values of K of different samples. From tests with the image-analysis method it became clear that the image-classification routine *i.e.* the conversion from a Red, Green, and Blue image to a binary image (see section on Sampling procedure and pre-processing of images) is sensitive to bias as a result of differences in the definition of training areas, between the images. As a result, pixels that are classified as "*pore*" in one image could have been classified as "*grain*" in another image if other training areas had been used. This effect biases the estimated total porosity because when relatively more pixels are classified as "grain" than in a second image, porosity is underestimated relative to the first image. The effect is of less impact to the estimated values of S_{sp} because that parameter is calculated by the ratio between grain perimeter and grain surface.

3.4.4 Laboratory measurements of hydraulic conductivity on core plugs

In addition to the estimation of hydraulic conductivity based on image analysis of thin sections, core-plug samples were taken in the field for a direct measurement of hydraulic conductivity in the laboratory. These samples were taken by carefully pushing 0.019×0.06 m ($radius \times length$) sample rings into the sediment. As with the box cores, the sediment outside the sample volume was excavated in order to reduce sample disturbance.

The hydraulic conductivity (K) of the core plugs was determined using a conventional constant-head permeameter. The samples were saturated with deaerated and disinfected water in a two-day period. The actual experiment consisted of flowing water through the sample with five different fluxes (q). The corresponding hydraulic-head potentials (H) were monitored using a high-precision differential pressure transducer (Druck LP 5000). The measured hydraulic-head differences

Sample	K [m / day]	S_{sp} [m^{-1}]	ϕ [-]
B1			
Mean	7.7	33,168	0.33
σ	3.4	4,663	0.049
B2			
Mean	15.3	36,031	0.41
σ	4.6	2,611	0.032
B3			
Mean	22.1	28,879	0.45
σ	8.8	2,103	0.042

Table 3.1: Overview of measured values of porosity and volumetric specific surface, and calculated hydraulic conductivity of samples B1, B2, and B3.

were corrected for internal-system resistance. Subsequently, the hydraulic conductivity was calculated by determining the slope of a straight line, fitted through the five q-H pairs. On the basis of the fit of this line, the precision of the procedure is estimated to be ± 1.8 m / day.

3.5 Hydrogeology of the Geleen Fault

The Geleen Fault was studied in detail in a trench with a depth of about 5 m. Along the trench no observation wells were available, though at a location nearby over the Feldbiss Fault, where the geology is comparable, there is a hydraulic-head difference of about 5 m in the phreatic surface over a distance of 25 m. This indicates that the Feldbiss Fault has a strong resistance to horizontal groundwater flow at a shallow depth. The geology of the trench is described by *Houtgast et al.* [2002], and is summarized below. The estimates on the age of the different sedimentological units is based upon the work of the authors last referred to.

In the trench over the Geleen Fault, four distinct units (A, B, C, and D) close to the fault (Figure 3.4) were visible. In the footwall block, sand, and some clay of fluvial origin (units A, B, and C) were visible. These four units are estimated to have an age of about 250 ka. In the hanging-wall block, loess (unit D) juxtaposes these units. Unit D is younger than units A, B and C, and has an estimated age between 30 and 60 ka. The sedimentological characteristics of units A, B, C, and D are summarized in Table 3.1.

Hand borings and a Ground Penetrating Radar survey revealed that at shallow depth the Geleen Fault has a throw of approximately 5 m. Units A, B, and C, described in the footwall block, could therefore not be seen in the hanging-wall block where only unit D was exposed (Figure 3.4). Deformation structures directly

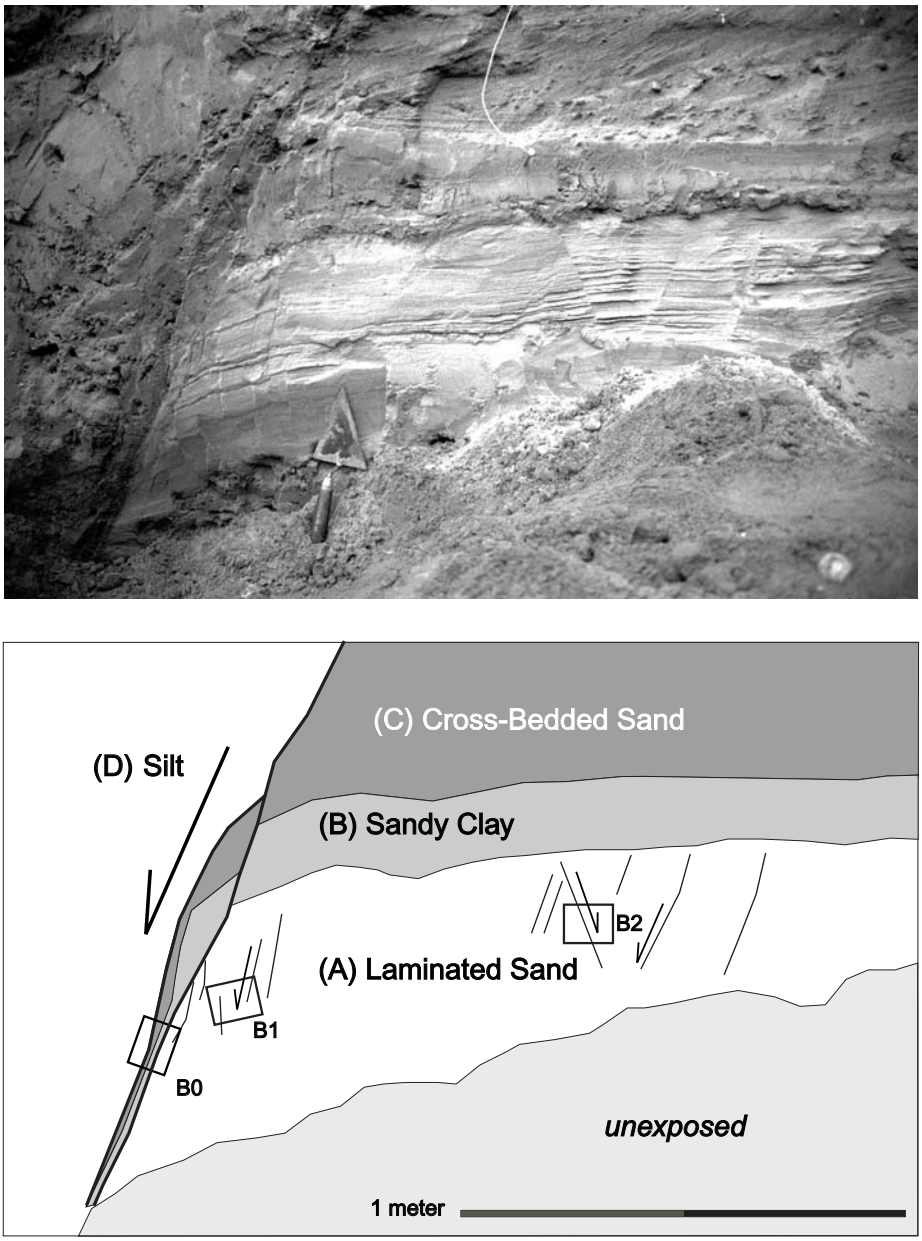

Figure 3.4: Overview of sampling locations for box cores B0, B1, and B2 in the trench over the Geleen Fault. For a description of units A, B, C, and D see Table 3.1 and the text.

Figure 3.5: The wall of the trench over the Geleen Fault during sampling of box cores and core plugs.

related to fault movement were visible in units A and B. Unit D was largely disturbed by slump and cryoturbation structures. In unit A, four box-core samples (B0, B1, B2 and B3; Figure 3.5) were taken for digital-image analysis in order to visualize the distribution of hydraulic conductivity associated with these structures and 13 core-plug samples were taken in Unit A to measure hydraulic conductivity in the laboratory for comparison to the results from the image-analysis procedure.

In the following sections, the macro-scale morphological characteristics of the Geleen Fault in the trench are first described. Subsequently, the results of digital-image analysis on the box cores and the laboratory measurements of hydraulic conductivity on the core plugs are presented.

3.5.1 Macroscale morphology

The Geleen Fault consists of a fault core that is flanked by a damage zone, consistent with the generic model of fault-zone architecture presented above (section 3.2.2; Figure 3.3).

The fault core of the Geleen Fault is shown in great detail in Figure 3.6. The fault core is the zone where almost all fault movement has taken place. This zone has a width of only 10 cm. Unit B, consisting of clay inter bedded with sandy laminae, is the source bed for a gently folded clay smear that is present along the fault plane. The clay smear has a maximum thickness of approximately two centimeters. It was

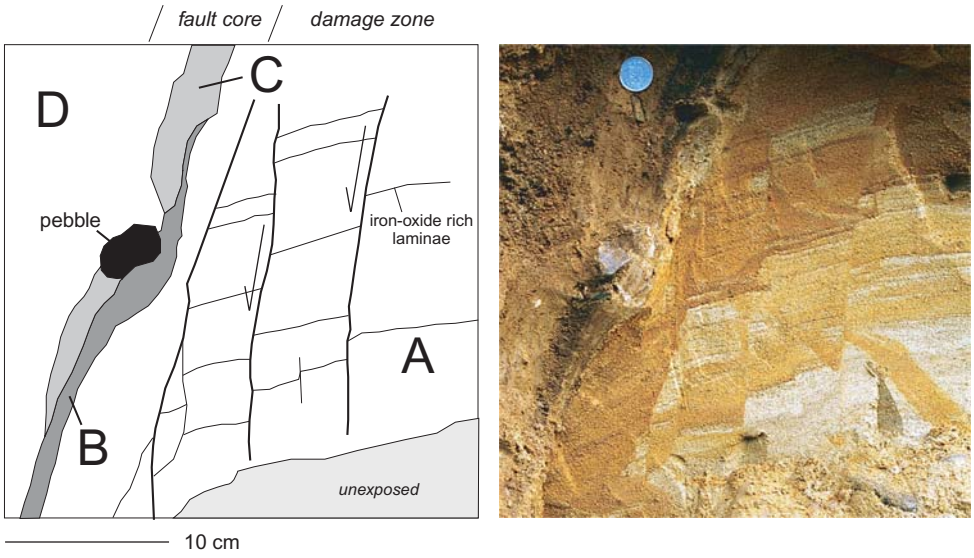

Figure 3.6: Photograph of the fault core of the Geleen Fault showing the morphology and lithological variation within the fault core. Gravel pebbles cause discontinuities in the clay smear.

not possible to determine whether the clay smear was continuous along the whole throw of the fault (~ 5 m). Though along strike, the smear could be discerned along the whole width of the trench (~ 2 m). Figure 3.6 also shows that gravel pebbles trapped in the fault plane cause discontinuities in the clay smear. Apart from the ductile clay smear, the dark sand of unit A is also dragged into the fault plane. Consequently, the fault core has an extremely heterogeneous composition.

A thin section of sample B0 shows the morphology of the fault core in detail (Figure 3.7). The width of the complete fault core approximately coincides with the total width of this image (~ 7 cm). A detailed look at sample B0 reveals that along the edge of the clay smear mixing of sand and clay has taken place during deformation (Figure 3.7). Also, a result of fault movement is the re-orientation of grains along several slip planes oriented parallel to the direction of the main fault plane (Figure 3.7). Whereas the smearing of clay along the fault plane takes place through ductile deformation, discrete micro-faults indicate brittle deformation.

The damage zone is defined as the zone in which these micro faults occur but do not have a vertical throw of more than ~ 10 cm, as is the case in the fault core (Figure 3.6). The micro-faults form a network with orientations parallel and con-

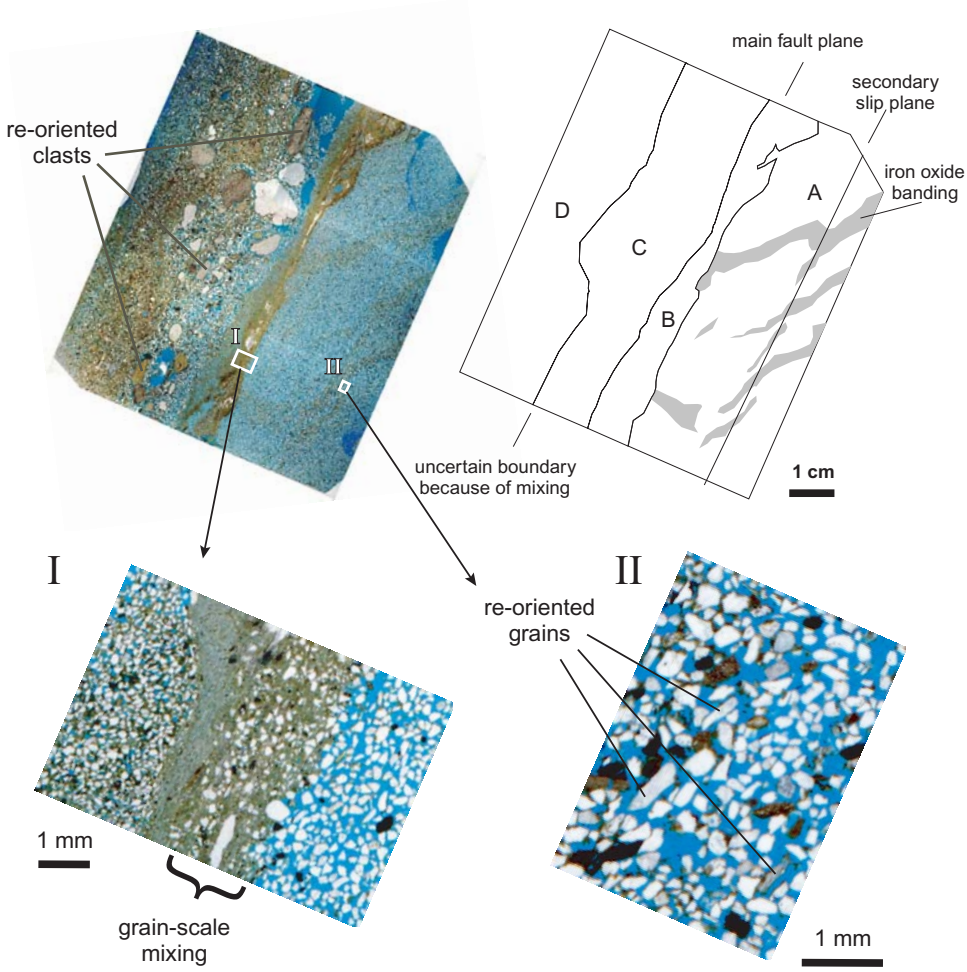

Figure 3.7: Thin section of sample B0 showing the morphological aspects and composition of the fault core in detail and at different scales. Re-orientation of grains and larger conglomerates of grains (clasts) in the fault core along discrete bands is accentuated by patterns of iron-oxide distribution. Mixing of clay and sand is visible but a distinct ”mixed-zone” has not yet developed at this stage of fault-zone formation.

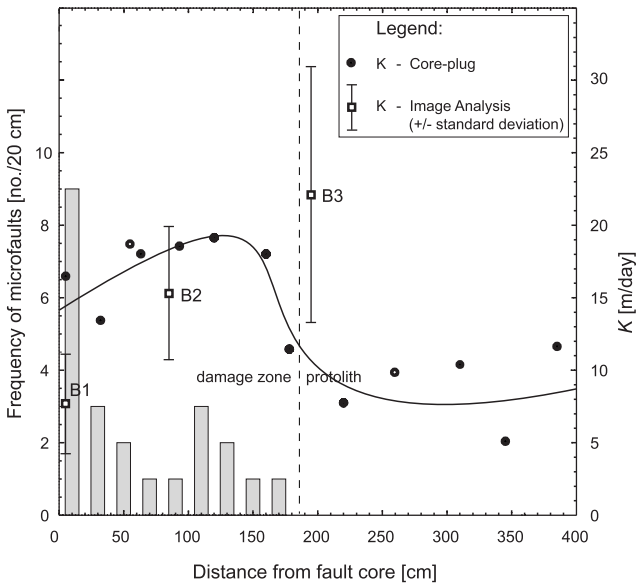

Figure 3.8: Plot showing the density of micro-faults in unit A decreases with distance from the fault core. A trendline following the K-values from core-plug measurements has been added for clarification.

jugate to the main fault orientation. Figure 3.8 shows the density of micro-faults parallel to the main fault plane in relation to the distance from the fault core. From this plot the damage zone in unit A is estimated to have a width of about $2\ \mathrm{m}$. In contrast, the sandy clay that forms unit B shows deformation expressed in the form of low-amplitude folding between a distance of 0 to $50\ \mathrm{cm}$ distance from the fault core (Figure 3.5). This zone is regarded as representing the width of the damage zone in unit B. The damage zone in unit A (sand) is thus about four times wider than in unit B (mainly clay). The width of the damage zone in unit C where no discrete micro-faults were visible, could not be assessed.

3.5.2 Hydraulic conductivity

The results of the laboratory measurements on core plugs to determine hydraulic conductivity are presented in Figure 3.8 together with the mean hydraulic conductivity estimated from thin sections of box-core samples B1, B2, and B3.

The values of hydraulic conductivity as measured on core plugs in the laboratory shows a weak correlation with the density of micro-faults as observed in the

field. In a zone of about $2\ \mathrm{m}$ from the fault core (the damage zone), hydraulic conductivity is almost doubled compared to the zone in which no micro-faults were found.

The REA for ϕ was determined on four places on the image prepared from thin-section B2, by making measurements in a window with increasing surface area (Figure 3.9). Although the REA for S_{sp} is not necessarily the same as that for ϕ, *Van den Berg et al.* [2003] show that a negligible error is made when assuming that the REA for both parameters has approximately the same value. In the following calculations a sampling window with a size of 125×125 pixels ($\sim 2.4\ \mathrm{mm}^2$) is used on the basis of the trend seen in Figure 3.9, which shows that the value of ϕ stabilizes at this window size. Table 3.1 shows the mean values and standard deviations (σ) of K, S_{sp}, and ϕ for sample B1, B2, and B3 as calculated by application of equations 3.1 and 3.2. Figures 3.10a-i shows the spatial-distribution maps of ϕ, S_{sp}, and K of these samples. The image-analysis technique allows for a further assessment of the relation between the spatial distribution of hydraulic conductivity within each sample from the transition between the fault core and the damage zone, the middle of the damage zone, and outside of the damage zone. The differences and the observed trends between the three samples are discussed below.

Sample B1 was taken immediately adjacent to the fault core at the transition between the fault core and the damage zone. The spatial distribution pattern of S_{sp} (Figure 3.10b) shows that higher values occur in the upper part of the image above two prominent sedimentary laminae. This increase of the specific surface area correlates with areas where secondary minerals precipitated preferentially between the quartz grains. Laboratory analysis shows that these minerals are iron oxides. Figure 3.11 shows how iron oxides are forming bridges between individual grains in conformity with theoretical work done by *Berner* [1980] who showed that grain contacts are energetically the most favorable locations for mineral precipitation during early diagenesis. On some places in B1 pore space is completely filled and porosity is reduced to zero.

The structure of the micro fault that cuts through this sample is prominent in the resulting spatial-distribution maps of ϕ, S_{sp}, and K (Figure 3.10a-c). This anisotropy has a vertical throw of several centimeters. Particulate flow is clearly recognized in the thin section as the deformation mechanism, resulting in the rotation of grains near the slip face (Figure 3.12), while broken and crushed grains, typical for cataclasis, are absent.

Sample B2 was taken in the middle of the damage zone over a anisotropy that has a throw of several millimeters. The resulting spatial-distribution maps of ϕ,

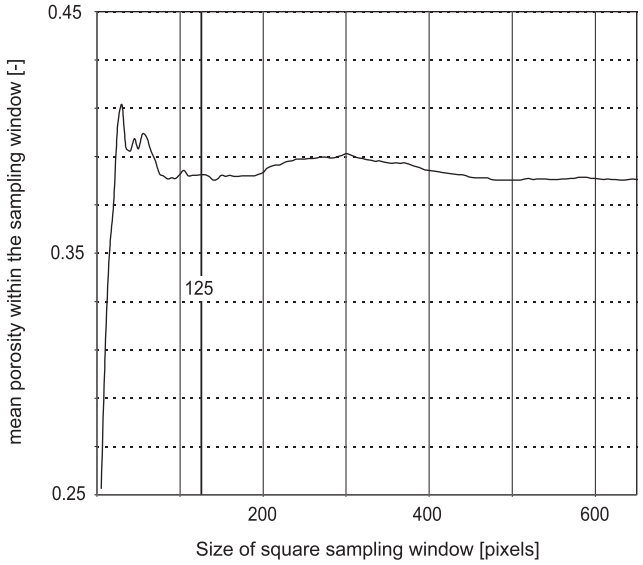

Figure 3.9: Plot showing that at a window size of around 125×125 pixels the mean value of porosity within the window stabilizes when the window is further increased. Therefore, based upon this plot, a window size of 125×125 pixels is used for the image analysis so as to represent the highest resolution at which a reliable estimate of porosity is obtained from the digital image.

S_{sp}, and K (Figure 3.10d-f) for this sample show more diffuse patterns than those for B1. The rotation of grains, indicating a zone of particulate flow, although essentially invisible anisotropy because it is only a few grains wide, is shown in diagram on Figure 3.4. The map for S_{sp} (Figure 3.10e) clearly shows the fine sedimentary lamination in the sample since iron oxides in the finer-grained laminae increase the volumetric specific surface. However, the resulting contrasts are not as strong as in sample B1 because the secondary precipitation of iron oxides is less extensive in B2, which is also translated into a larger bulk value of ϕ and K in sample B2.

Sample B3 is situated outside the damage zone where no micro-faults could be identified. Only a part of this sample could be used for the image analysis due to problems with entrapment of air in the sample, which lead to incomplete impregnation. The resulting images (Figure 3.10g-i) show to some extent the same pattern as visible in sample B2. In samples B1 and B2 the original (sedimentary) permeability contrasts are enhanced by iron-oxide precipitation. In sample B3 the permeability contrasts resulting from primary sedimentary structures appear to be

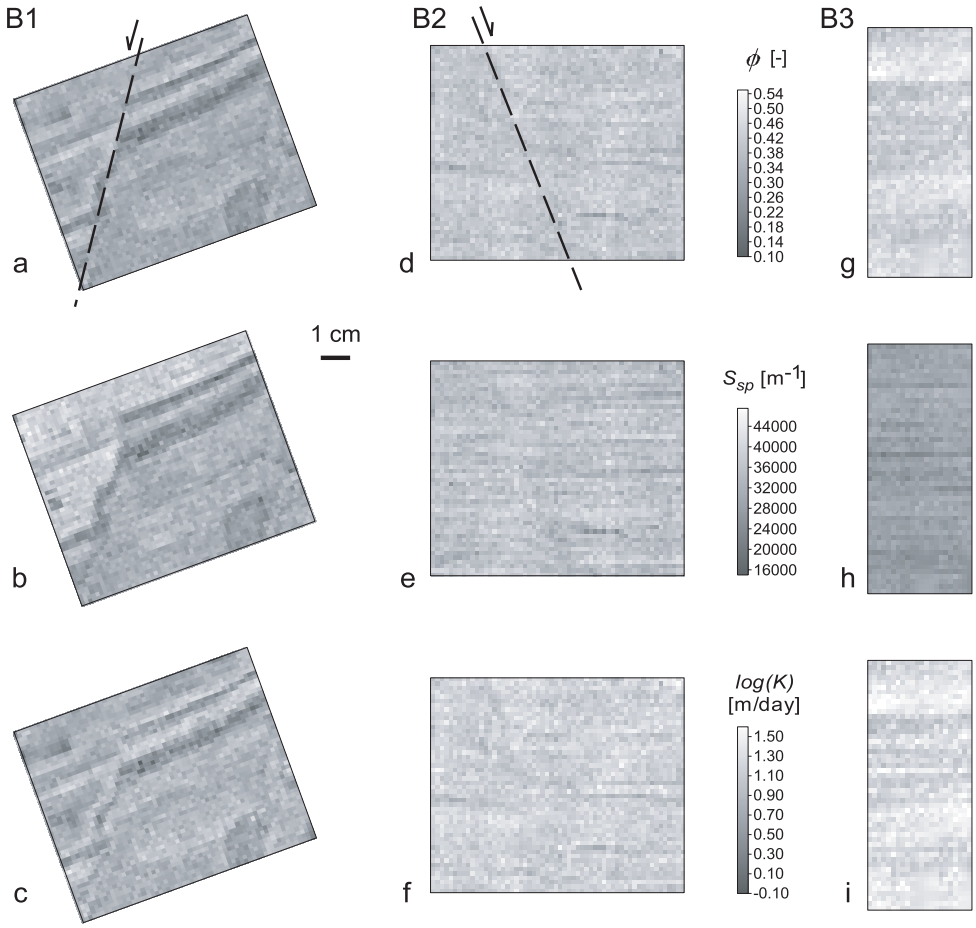

Figure 3.10: The spatial distribution of porosity (ϕ), specific surface (S_{sp}), and hydraulic conductivity (K) for sample B1 (*a, b, c*), B2 (*d, e, f*), and B3 (*g, h, i*) respectively.

overprinted by iron-oxide precipitation that generally occurred in beds comprised of sets of sedimentary laminae.

3.6 Discussion

In this section the observations made in the trench over the Geleen Fault are further interpreted and the results are placed in the context of existing fault-zone models. First, the results of the image-analysis procedure are compared to pub-

lished data for S_{sp}. The estimated values of K are evaluated using the results from the core-plug measurements.

Carman [1938] reports values of $1.5 \cdot 10^4$ to $2.2 \cdot 10^4 \mathrm{m}^{-1}$ for S_{sp} of well-sorted clean sand. For samples B1, B2, and B3 the average values for the volumetric specific-surface area are $3.2 \cdot 10^4 \mathrm{m}^{-1}$, $3.6 \cdot 10^4 \mathrm{m}^{-1}$ and $2.9 \cdot 10^4 \mathrm{m}^{-1}$ respectively. These are almost twice as high as the literature values, which can be explained in two ways. The grain-size distribution of these sands shows that there is some fine fraction in the bulk sample that may cause S_{sp} for these specific sediments to be higher than for the well-sorted clean sand used by *Carman* [1938]. Probably of more importance is the effect of iron-oxide precipitation of an irregularly shaped coating around individual grains (Figure 3.11), which physically increases the specific-surface area. The degree of iron-oxide cementation increases towards the fault core which is reflected in a simultaneous increase of S_{sp} in the same direction (Table 3.1). Note also that, although the specific-surface area is increased by moderate iron-oxide precipitation on the grains, sample B1 (Figure 3.10b) shows that when iron-oxide cementation is stronger and pore space becomes sparse, S_{sp} is ultimately strongly reduced.

A fairly good match exists between K values resulting from the laboratory measurements on the core plug and the image-analysis procedure. However, the results of the image analysis suggest that the hydraulic conductivity decreases towards the fault core, while the laboratory measurements show a doubling of hydraulic conductivity in the damage zone relative to the undisturbed sediment.

When comparing both results, the following should be taken into account. The core-plug samples a surface (only the 2D distribution of hydraulic conductivity is concerned here) that is almost one order of magnitude smaller than that of the box core ($1.1 \cdot 10^{-3} \mathrm{m}^2$ vs. $8.0 \cdot 10^{-3} \mathrm{m}^2$). Although there exist lateral variations of K in the sampled sediment, which is highlighted in the standard deviations calculated for the box-core samples, the core plugs still have a large enough sample area to be locally representative. The lateral variability of K over a short distance, based on the core-plug measurements, especially in the damage zone, is small (Figure 3.8).

In addition to the remarks made in section 3.4.3, it is concluded that although the results from image analysis give a reasonable estimate of the saturated hydraulic conductivity of the sediment, the specific value of the image-analysis procedure is that it provides an image of the spatial variability of K within a sample. If the lateral variability of K is discussed, the distribution of hydraulic conductivity based on the core-plug samples should be considered to be more accurate.

3.6.1 Macroscopic structure and deformation mechanisms

The macroscopic morphology of the Geleen Fault as described in the section on Digital-Image Analysis, is consistent with the model proposed by *Heynekamp et al.* [1999] (Figure 3.3). In that model the width of the damage zone is primarily controlled by the grain-size distribution of the faulted sediments. In the clay-rich parts of a sequence the damage zone is narrow relative to the sand-rich parts. The same relationship is found in the present study on the Geleen Fault.

The fault core of the Geleen Fault at the location of the trench will form a barrier to groundwater flow, as both clay smearing and grain-scale mixing strongly increase the resistance of the fault zone to horizontal groundwater flow. Gaps in the clay smear caused by gravel pebbles may however form preferential flow paths (Figure 3.6). In addition, grain-scale mixing in the fault core results in a clay-sand fabric that will also add to the reduced hydraulic conductivity of the fault core, since pore bodies are forcefully filled with clay and porosity is reduced to practically zero. The strong preferential orientation of grains along numerous slip planes within the fault core as shown by qualitative image analysis (Figure 3.7; B0), is likely to result in a strongly anisotropic distribution of hydraulic conductivity because along the fault plane hydraulic conductivity will tend to be higher than in the direction perpendicular to it. The magnitude of this anisotropy could not be assessed since core-plug samples were taken only along the strike of the fault plane.

In the damage zone, thin sections show that particulate flow is the dominant deformation mechanism as would be expected near the surface. The intensity of deformation, using the macroscopic density of micro-faults as an indicator (Figure 3.8), decreases away from the fault core. The resulting increase in hydraulic conductivity in the damage zone relative to the undisturbed sediment is shown by the core-plug measurements. In addition, image analysis shows that the amount of iron-oxide precipitation increases towards the fault core, proportional to the amount of deformation.

3.6.2 Evolution of hydraulic conductivity in the damage zone

Two post-depositional, syn-tectonic, processes have altered the porosity of the sediment in opposite ways. On the one hand, diagenetic precipitation of iron oxides has caused a reduction of porosity, while on the other hand deformation due to particulate flow increases porosity along micro-faults (slip planes).

The observed variation of hydraulic conductivity within the damage zone is interpreted using an analysis of the distribution of iron oxides within the damage zone. It appears that iron-oxide distribution is linked to primary sedimentary

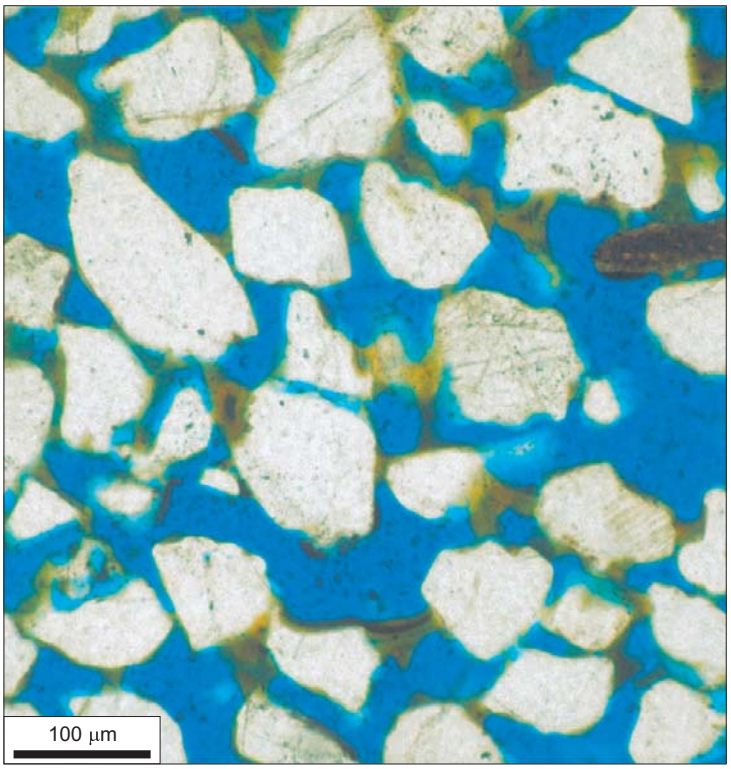

Figure 3.11: Thin section of sample B1 showing the bridges of iron oxides that developed in the sediment after deposition.

heterogeneities, as well as to secondary heterogeneities resulting from tectonic deformation. Thin sections show that iron oxides are preferentially precipitated along relatively fine-grained laminae. Induration of the oxides is probably accomplished by repeated wetting and drying during periods of pronounced water-table fluctuation. It is envisaged that when the groundwater table is lowered, water is retained in the relatively fine-grained laminae that have a greater water-retention capacity. While the larger pores in the coarser surrounding layers are filled with air, the iron-bearing water within the fine laminae is oxidized.

To explain the increasing degree of iron-oxide precipitation towards the fault core, it is suggested that deformation processes, *i.e.* the disaggregation of the grain fabric by particulate flow, primarily increased permeability significantly in the damage zone. As observed in outcrop and thin section, deformation is stronger

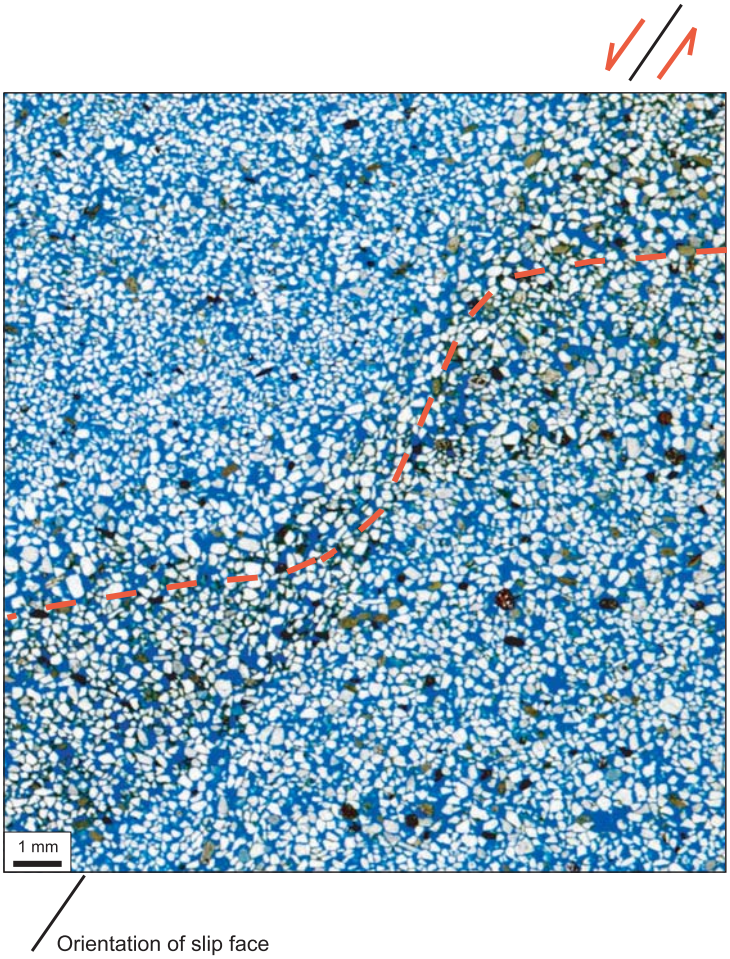

Figure 3.12: Detailed image from thin section of a part of sample B1, showing how particulate flow along a narrow slip plane accommodates a vertical throw of about one centimeter. The dashed line shows how one stratigraphic level is offset by the deformation band.

closer to the fault core. Therefore, the primary enhancement of hydraulic conductivity will have been more intense closer to the fault core. In addition, deformation resulted in an anisotropic distribution of hydraulic conductivity because of the rotation of grains towards an orientation preferentially parallel to the fault plane. These two combined effects will have focused fluid flow along the fault plane through the damage zone, which explains the stronger cementation with iron oxides as observed now. *Nelson et al.* [1999] propose a similar process to explain the development of a 'cementation halo' related to enhanced fluid flow in the damage zone, in the description of well-exposed outcrops that are studied as analogs of hydrocarbon reservoirs. The difference from the present study is that *Nelson et al.* [1999] observed the development of the cementation halo in strongly lithified sediments in a fault zone where hydraulic conductivity is enhanced through fracturing within the damage zone. The depth to which the mechanism described previously is valid is dependent on the depth to which particulate flow disaggregates the grain fabric. The deformation map (Figure 3.2) indicates that particulate flow will be the dominant mechanism from the surface till to at least $750\ \mathrm{m}$ burial depth.

3.7 Conclusions

The spatial distribution of hydraulic conductivity has been described in a trenched outcrop over the Geleen Fault, that cuts through unconsolidated sediments. The Geleen Fault is shown to be a hydrogeologically heterogeneous and anisotropic feature. In the hydrogeological characterization of this fault zone, image-analysis techniques proved to be valuable tools to use as an addition to direct measurements of hydraulic conductivity. Quantitative-image analysis gives insight to the link between tectonic structures and the associated variation of hydraulic conductivity. Qualitative interpretation of thin sections showed how mixing and re-orientation of grains in the fault core and the damage zone of the Geleen Fault impact hydraulic conductivity.

The observations in the trench over the Geleen Fault illustrate that in poorly lithified sediments at shallow depths, particulate flow is an important deformation mechanism in "clean" sand. Thin sections show that particulate flow at shallow depth is likely to significantly disaggregate the grain fabric. Therefore the damage zone that has formed in the sandy deposits around the Geleen Fault will probably act as zones of enhanced fluid flow at shallow depth. These observations are an addition to existing hydrogeological models of fault zones as described in the literature [*e.g. Rawling et al.*, 2001; *Caine et al.*, 1996] that are largely based on deformation through cataclasis.

4

Geothermal patterns as tracer for shallow groundwater flow around the Peel Boundary Fault Zone near the village of Uden

Abstract

In this Chapter it is shown how profiles consisting of closely spaced (≤ 10 m) temperature measurements at shallow depth, obtained at several instances during one season, provide a detailed record of lateral variations in vertical groundwater flow. This is illustrated by a field study around the Peel Boundary Fault zone that cuts through the unconsolidated, siliciclastic deposits that occur in the southeastern part of the Netherlands. This regionally important fault forms at many locations a strong barrier to horizontal groundwater flow and therefore induces complex groundwater flow patterns. Temperature anomalies (over 2 °C) are observed over short distances. These anomalies reverse over the season. Numerical modeling of coupled groundwater flow and heat transport demonstrates how the temporal and spatial variations of sub-surface temperature are the result of the interaction between seasonal fluctuations in surface temperature and spatial variations in groundwater flow. In addition to the horizontal profiles, temperature-depth profiles obtained in groundwater observation wells were used to constrain the larger-scale characteristics of the groundwater flow system. In order to simulate the observed geothermal patterns it appeared to be essential to account for the long-term changes in surface temperature. Although, groundwater temperature data are commonly used to constrain groundwater flow fields on regional scale or to calculate vertical groundwater velocities at point locations beneath small streams, the present study is one of the first to integrate these different scales and incorporate the impact of recent climate change.

This Chapter is largely based upon: Bense, V.F. and H. Kooi, Temporal and spatial variations of shallow subsurface temperature as a record of lateral variations in groundwater flow, *Journal of Geophysical Research, 109*, B04103, doi:10.1029 / 2003JB002782, 2004.

4.1 Introduction

For many decades, subsurface temperature measurements have been used to constrain both relatively deep, regional groundwater flow systems [*e.g. Smith and Chapman*, 1983; *Forster and Smith*, 1989; *Person et al.*, 1996; *Mailloux et al.*, 1999; *Buttner and Huenges*, 2003] as well as more shallow, small scale groundwater flow [*e.g. Andrews and Anderson*, 1979; *De Jong and Geirnaert*, 1979; *Bravo et al.*, 2002]. The key feature that is exploited to study these systems is that advection of heat by vertical upward or downward groundwater flow causes vertical temperature-depth profiles to become more convex or concave respectively, relative to the "undisturbed" geothermal gradient. Quantitative relationships developed by *Bredehoeft and Papadopulos* [1965]; *Stallman* [1965]; *Domenico and Palciauskas* [1973] allow to estimate one-dimensional vertical flow rates from geothermal data. Additionally, *Lu and Ge* [1996] present a method to evaluate the temperature effects of horizontal groundwater flow in semi-confining layers.

At shallow depths (< 20 m), the interpretation of geothermal data is more complicated because seasonal changes in surface temperature tend to propagate to these depths. *Stallman* [1965] analyzed the exponential damping of surface amplitude and phase shift for groundwater flow and developed a type-curve method, which was subsequently applied and modified by other workers [*e.g. Boyle and Saleem*, 1979; *Cartwright*, 1979; *Taniguchi*, 1993]. Moreover, *Lapham* [1989] presented one-dimensional numerical simulations of the seasonally changing temperature regime at shallow depth to calculate vertical groundwater flow velocities under small streams.

Kukkonen and Clauser [1994]; *Taniguchi et al.* [1999a, b] show that, also at greater depth, temporal changes in surface temperature can usually not be neglected in the interpretation of temperature-depth data for groundwater flow since climate change and changes in surface environmental conditions induce considerable curvature in temperature profiles up to depths of about 300 m. The effects of climate warming are globally recorded in the thermal regime and inversion techniques are widely applied to infer the rate and magnitudes of recent surface warming from temperature-depth profiles [*e.g. Huang et al.*, 2000; *Beltrami*, 2002].

At very shallow depths (< 0.5 m) diurnal temperature fluctuations dominate. Downward propagation of the diurnal heat wave is damped or enhanced by upward and downward flow in the same way as seasonal signals. Methods have been developed that combine measurements of surface temperature and of the temperature at shallow depth beneath small streams to monitor the rates of surface water-ground water interaction at specific locations [*e.g. Silliman and Booth*, 1993; *Ronan*

et al., 1998; *Constantz et al.*, 2002]. Also, *Van Wirdum* [1991] demonstrated the use of shallow temperature-depth measurements in peat to infer vertical groundwater flow velocities. *Csónka* [1968] and *Cartwright* [1974] have attempted to use shallow horizontal soil temperature profiles to discern areas of groundwater recharge and discharge, and *Krcmár and Máším* [1970] reported to have mapped small faults based upon the seasonally changing pattern of soil temperature at a depth of $1.5\ \mathrm{m}$. In spite of the great potential power and elegance of this technique, however, this work has had little impact. The significance of observed temperature patterns observed by *Cartwright* [1974] has remained obscure because large and non-trivial corrections had to be made for the presence of a vadose zone in the soil profile. *Csónka* [1968] obtained intriguing measurements in streams in the Netherlands but he did not fully recognize the significance of his findings. Also *Krcmár and Máším* [1970] did not give a complete interpretation of the patterns they observed around shallow faults.

Here, the approach of horizontal temperature profiling is revisited and the full potential of the methodology is demonstrated. The field data that are presented in this study were gathered in a wetland-like area around a shallow fault zone in the southeastern part of the Netherlands. Repeated measurements have been done of the horizontal temperature profile below a ditch that runs perpendicular to the fault scarp. These measurements were done at a shallow depth ($0.5\ \mathrm{m}$) below the stream bottom by pushing a thermistor built into the tip of a plastic pole into the soil. It is proposed that the strong temperature anomalies ($\sim 2\ ^{\circ}\mathrm{C}$) that occur in these profiles are the result of the interaction between a seasonally fluctuating surface temperature and variations in groundwater flow velocities close to the surface. In order to test the validity of this interpretation, the observed horizontal temperature profiles are evaluated in the context of the larger scale hydrological system around the fault zone. Therefore, the observations from the horizontal temperature profiles are combined with temperature-depth data from groundwater observation wells and measurements of the electric conductivity of both groundwater samples and surface water. A numerical model was developed that incorporates both the interaction of a seasonally fluctuating surface temperature with shallow groundwater flow as well as the impact of groundwater water flow on the sub-surface temperature on a larger scale. Moreover, as suggested in other studies, for a correct interpretation of the deeper thermal regime it was essential to consider the effect of recent surface warming.

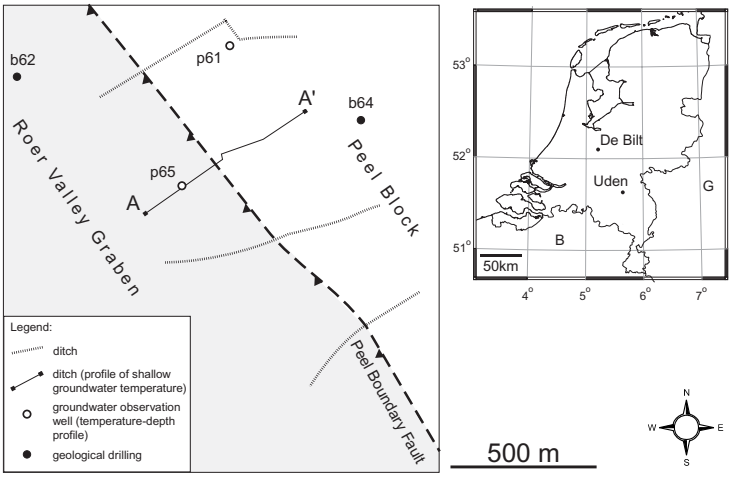

Figure 4.1: Location and simplified map of study area in the southeastern parts of the Netherlands close to the village of Uden (B=Belgium, G=Germany). Location of boreholes that are used in this study are indicated.

4.2 Site description

The field site discussed in this Chapter is located close the village of Uden along the Peel Boundary Fault Zone (PBFZ) (Figure 4.1) that is part of the regionally extending Roer Valley Rift System (RVRS) [*Ziegler*, 1994; *Michon et al.*, 2003]. At this location the PBFZ forms a small fault scarp with a height of ~ 3 m. Recent studies show that faults in the unconsolidated Quaternary and Tertiary sediments of the RVRS exert an important impact on the local and regional groundwater flow system [*Wallbraun*, 1992; *Bense et al.*, 2003a]. Faults in the RVRS generally impede groundwater movement while at the same location they can form the locus of focused pathways of vertical exchange of groundwater between otherwise separated aquifers. Outcrop studies carried out by *Bense et al.* [2003b] and *Lehner and Pilaar* [1997] show that clay smearing, particulate flow of grains and re-orientation of grains can explain the typical heterogeneous and anisotropic characteristics of fault zones in the RVRS. Moreover, these studies show that at shallow depth fault zones in the RVRS are generally limited to a width of less than ~ 10 m.

4.2.1 Geology

The description of the geology of the field site is based upon two borings from either side of the PBFZ (b64 & b62; Figure 4.1). A top layer consisting of fine grained Quaternary aeolian sands is present on both sides of the fault. While in the Roer Valley Graben (RVG) this top unit has a thickness of ± 20 m, on the Peel Block (PB) it is only a few meters thick. These fine sands are covering an aquifer that is built up of coarse to very coarse fluvial sands, of Quaternary age. On the PB a thick sequence of Miocene marine fine to very fine sand is found below the upper aquifer while in the RVG the main aquifer is underlain by a sequence of Quaternary fluvial clay, coarse sand and gravel.

4.2.2 Hydrology

At many locations along the eastern side of the PBFZ small wetland-like areas have formed at places where very shallow groundwater tables occur even during the driest periods of the season. In observation well p61, situated in the PB, the hydraulic gradient indicates upward flow during the whole season. In contrast, in observation well p65, located in the topographically lower RVG, downward flow is inferred. Groundwater seepage is observed on the PB as strongly mineralized water flowing into ditches at localized spots.

These upward flow and localized seepage phenomena on the higher parts on the PB and downward flow on the RVG are interpreted to be caused by the low permeability of the PBFZ (Figure 4.2). Aerial photographs show the heterogeneous nature of groundwater seepage in the distribution of wet and dry areas in fields where the bare soil is visible (Figure 4.3). It is hypothesized that lithological heterogeneity in the cover layer on the PB causes the observed focused discharge of groundwater in discrete zones.

4.3 Methodology and field data

Geothermal and geochemical data were gathered at the field site during a field campaign in the season 2002-2003. Temperature-depth profiles were measured in groundwater observation wells p61 & p65 (Figure 4.1) once a month. Both shallow groundwater temperature as well as the electric conductivity (EC) of the ditch water along A-A' were routed three and two times respectively during the field campaign. Additionally, EC was measured of groundwater samples extracted from the filters in the two available groundwater observation wells.

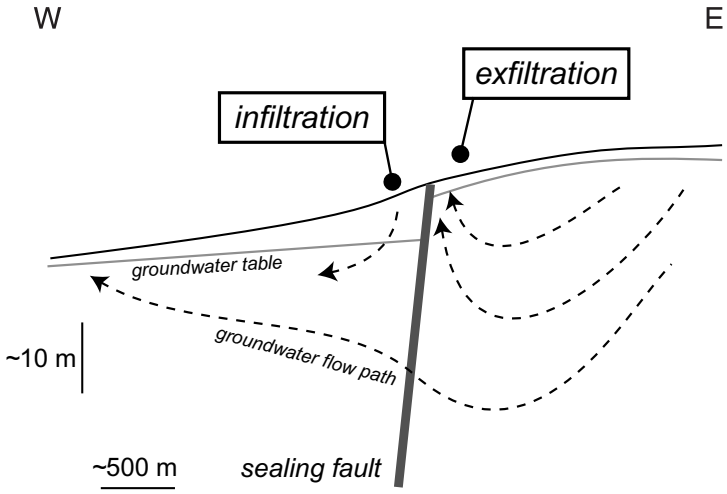

Figure 4.2: Schematic hydrological section showing the topographically driven groundwater flow pattern around the Peel Boundary Fault Zone as inferred from groundwater table measurements and regional hydraulic head data. A small wetland has developed just upstream of the fault where groundwater seepage occurs (exfiltration) as a result of the low permeability of the fault zone.

4.3.1 Geothermal data

A winch with a thermistor probe attached on one end of a cable was used for measurements in the two observation wells (p61 & p65). Both wells have a diameter of 2.54 cm which is small enough to minimize problems with instability of the water column through convective flow as a result of the temperature gradient present in the well [*e.g. Sammel*, 1968; *Cartwright*, 1979]. The instrument was fitted with a YSI Series 400 thermistor. The practical precision of the temperature measurements based on field experience and the specified precision of the thermistor is in the order of $1 \cdot 10^{-2}$ °C. The temperature sensing element was carefully lowered into the well in order to minimize a possible disruption of the original profile. In the top 25 m of the aquifer temperature was logged with intervals of 1 m, below this depth, each 2 m a temperature was logged. Figure 4.4 shows the time-series of temperature-depth profiles that were obtained in wells p61 & p65.

Measurement of temperatures below the ditch along A-A' was carried out in March 2002, September 2002 and January 2003 (Figure 4.8a). Measurements were conducted with a plastic stick with a thermistor (YSI 400 series) built into its tip. This device is pushed into the ground so that the temperature at a desired depth

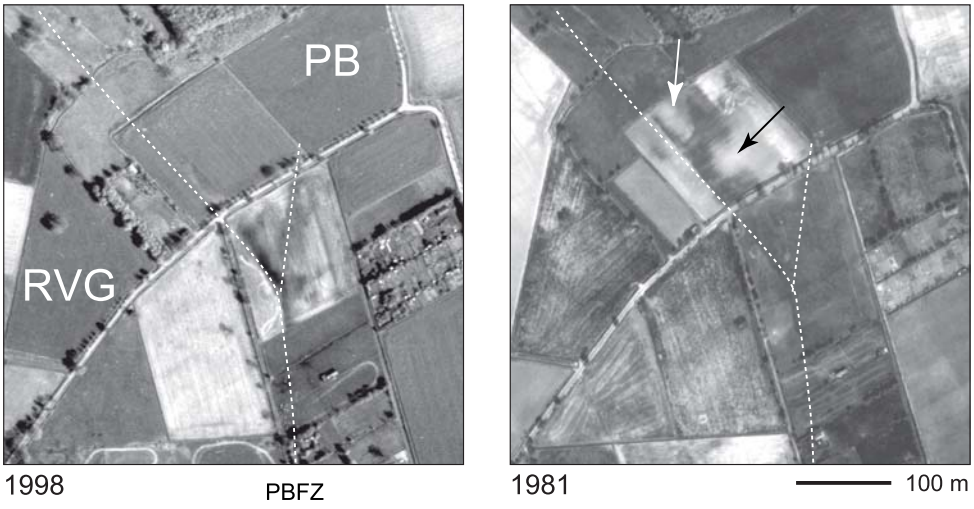

Figure 4.3: Aerial photographs taken in 1981 and 1998 show the heterogeneous nature of seepage zones north of the fault scarp. Dashed lines indicate fault lines. Arrows show the location of dry spots in wet seepage zones which are associated with lithological heterogeneities in the cover layer. RVG = Roer Valley Graben; PB = Peel Block; PBFZ = Peel Boundary Fault Zone.

can be measured after the temperature of the thermistor has stabilized. In this study, measurements were done at a depth of $50\ \mathrm{cm}$ below the bottom of the ditch. The limited strength of the stick did not allow us to probe to much greater depth. Measurements were done with a spacing of around $10\ \mathrm{m}$. The ditch has typically only several cm of water.

It can be shown based upon basic heat-conduction theory [*Stallman*, 1965; *Boyle and Saleem*, 1979], that for conditions in the Netherlands, diurnal temperature variation at a depth of $50\ \mathrm{cm}$ are less than $\sim 0.4\ ^{\circ}\mathrm{C}$. Because acquisition of each temperature profile took several hours only (typically from around 10 A.M. to 2 P.M.) only a systematic trend in the profile may, therefore, be induced with a magnitude of $\pm 0.1\ ^{\circ}\mathrm{C}$. The maximum error in temperature reading that could occur when the depth of measurement is inaccurate (*i.e.* when the measuring stick is pushed too deep or too shallow) is in the same range.

4.3.2 Electric conductivity

Measurements of EC were carried out using a simple field EC-meter with a precision of $\pm 2\ \mu\mathrm{S/cm}$. Next to the EC routing of the water in the ditch along A-A', groundwater samples were taken from the two groundwater observation wells (p61 & p65) at three different depths (Table 4.1). To ascertain that the in-situ groundwater at the depth of the filter was sampled, each well was pumped in advance until the total volume of the well had been flushed three times. Figure 4.8b presents the results of the EC measurements along A-A'.

4.4 Analysis of individual field data

In this section the field observations are first qualitatively described and analyzed individually as each data source holds a piece of information at a specific scale both spatially and temporal. Subsequently, it will be shown in the next section how these individual observations and their interpretation fit together into one model of coupled heat transport and groundwater flow around the PBFZ.

4.4.1 Temperature-depth profiles

The impact of seasonal surface temperature variation is the most conspicuous feature of the temperature-depth profiles as depicted in Figure 4.4. Qualitative comparison of the temperature-depth profiles for well p65 & p61 first shows that the profiles in well p61 are vertically somewhat compressed compared to the profiles observed in well p65 (Figure 4.4). Moreover, the funnel-shaped envelope of the curves in the upper $15\ \mathrm{m}$ of the profiles appears to be slightly deflected to the right (higher temperatures). This suggests that the seasonally averaged temperature increases towards the surface. In order to be able to trace possible transient signals resulting from variations of mean surface temperature with a lower frequency than the annual cycle, the seasonal variation was filtered out in the following way. It is assumed that the amplitude of annual variation of temperature (T_z [°C]) at a depth z [m] can be described by a harmonic function [*Stallman*, 1965; *Boyle and Saleem*, 1979] stated as:

$$T_z = \overline{T}_z + \Delta T_z \sin\left(\frac{2\pi t}{\tau} + b\right) \tag{4.1}$$

where b [s] denotes the phase shift of the sine function, $\overline{T}_z$ is the estimated average temperature at depth z over a one year period, ΔT_z is the estimated annual variation of temperature at depth z and τ is the duration of one year in s. An optimizing routine was applied (Nelder-Mead Simplex method) to estimate values for

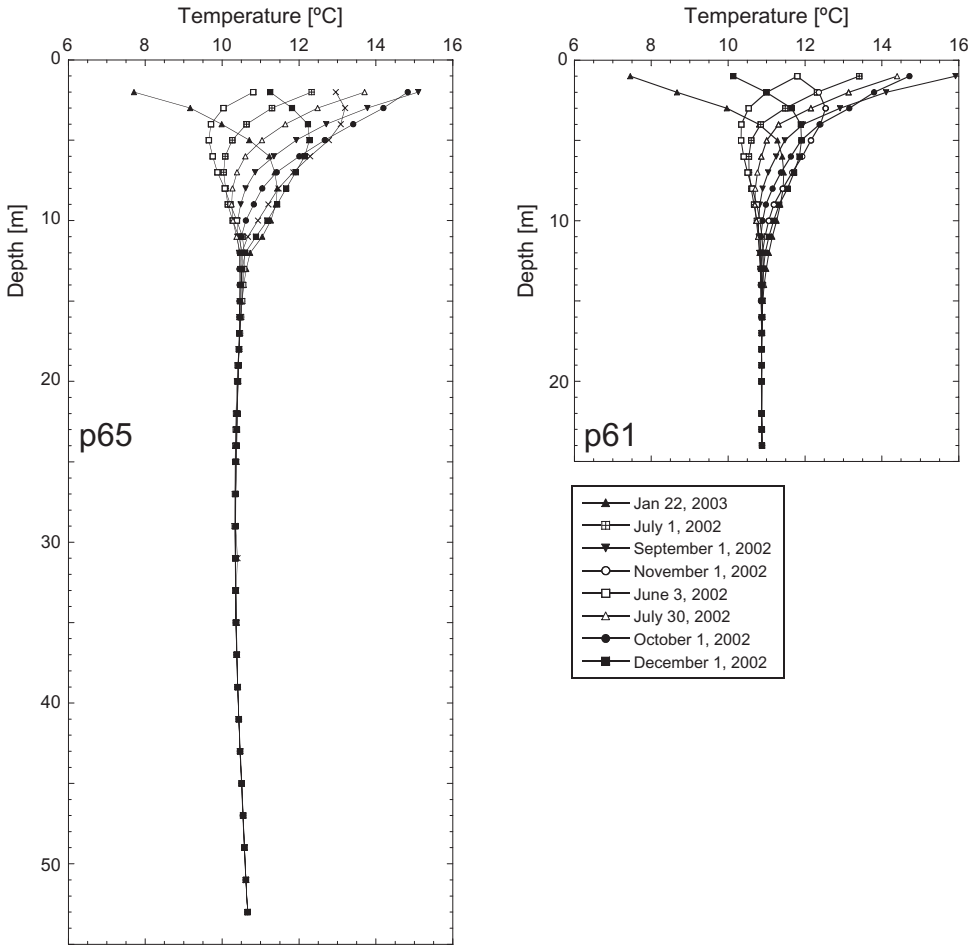

Figure 4.4: Observed temperature-depth profiles in wells p61 & p65 between May 2002 and January 2003. The upper $\sim$15 m of the profiles show the impact of the seasonal fluctuation of surface temperature.

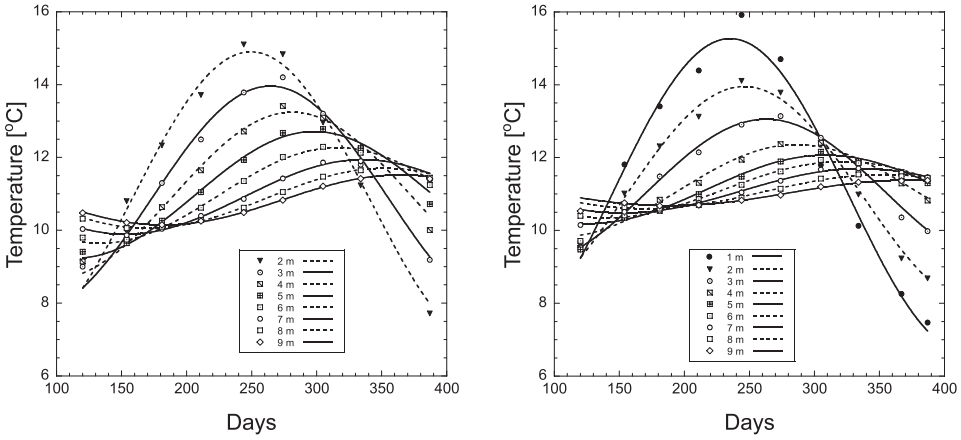

Figure 4.5: Fitted sine-curves (lines) for the temperature-depth data (symbols) from well p61 & p65. On the horizontal axis is time in days after January 1, 2002.

$\overline{T}_z$, b and ΔT_z for each depth at which a time-series of temperature was measured (Figure 4.5).

Figure 4.6 displays the "corrected" temperature-depth profiles in wells p61 & p65. The typical "C"-shape of the profiles that is prominently present in both wells is observed in most parts of the world and generally attributed to global warming [*Sebagenzi et al.*, 1992; *Čermák et al.*, 1992; *Huang et al.*, 2000; *Beltrami*, 2002]. Small amplitude wiggles are observed in the top $\sim 10\ \mathrm{m}$ in Figure 4.6. As the profiles of well p61 & p65 show a similar trend with depth, these shallow wiggles are interpreted to be transient signals resulting from variations in annually averaged surface temperatures.

The temperature-depth data were further analyzed for signals of groundwater flow using the type-curve method as described by *Taniguchi* [1993]. The method requires that the amplitude of annual variations of groundwater temperature at several depths (relative to a reference depth z_0) and the thermal properties of the aquifer are known. Combining the estimates for ΔT_z obtained this way with the following parameter values for the sediments of thermal conductivity $\kappa = 2.5\ \mathrm{W/m^{\circ}C}$, the specific heat of the saturated aquifer $c = 2013\ \mathrm{J/kg^{\circ}C}$ and the density of the saturated aquifer $\rho = 2105\ \mathrm{kg/m^3}$ [*De Jong and Geirnaert*, 1979], allows to plot the data to $\beta-$type curves (Figure 4.7). Surprisingly, the data of both wells fit for negative values of β which would indicate downward flow [*Taniguchi*, 1993] on both sides of the fault. However, this result is in conflict with the ob-

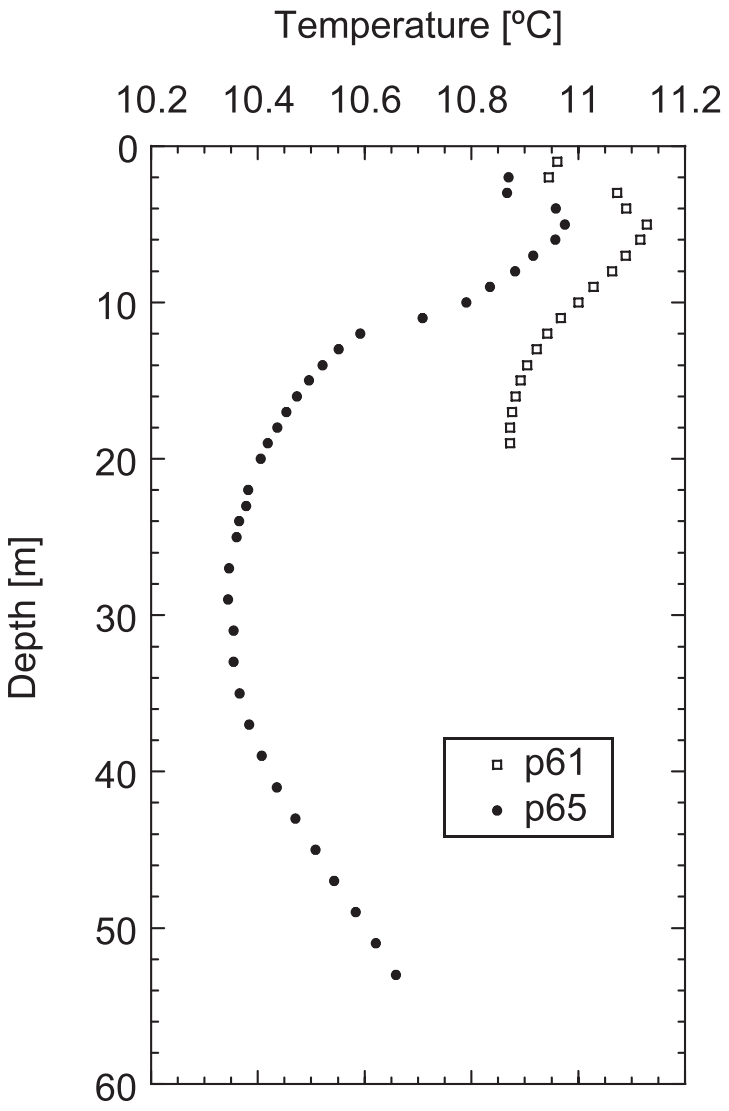

Figure 4.6: The average temperature-depth profiles (over the period May 2002 and January 2003) as observed in well p61 & p65. The annual variation in the upper part of the profiles has been removed by following the procedure as described in the text. The typical "C"-shape that these profiles show is found on a global scale and is attributed to surface warming over the last tens of years.

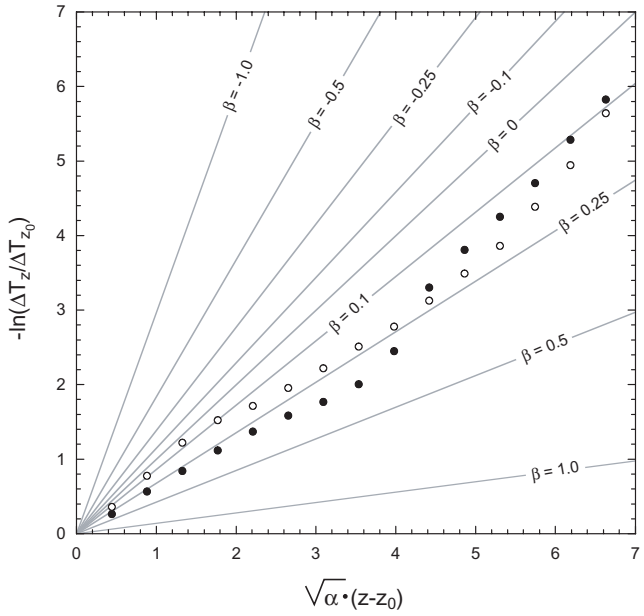

Figure 4.7: Non-dimensional plots of temperature data at well p61 (○) and well p65 (●) according to a method described by *Taniguchi* [1993], $z_0 = 2$ m, $\alpha = c\rho/\kappa\tau$. Positive values for β represent downward groundwater flow, however, this is in contradiction with observed hydraulic head gradients in the same wells.

served hydraulic gradients. Possibly, transient temperature signals other than the seasonal fluctuation at the surface are corrupting the applicability of the method described by *Taniguchi* [1993]. Moreover, the contrast in vertical groundwater flow velocities between recharge and discharge area at the present field site are far less pronounced than in the Tokyo metropolitan area where this method was originally tested. The latter analysis is included for sake of completeness, but the results are deemed not to be of much use.

4.4.2 Horizontal sections of temperature and electric conductivity

The horizontal temperature data that were gathered in the ditch along section A-A' are shown in Figure 4.8a. Lateral temperature contrasts of over 2 °C along A-A' are observed during both winter (January) and summer (September). Groundwater temperatures below the ditch on the RVG show far less lateral variation compared to the PB east of the PBFZ. Moreover, significant lateral variations exist in the ampli-

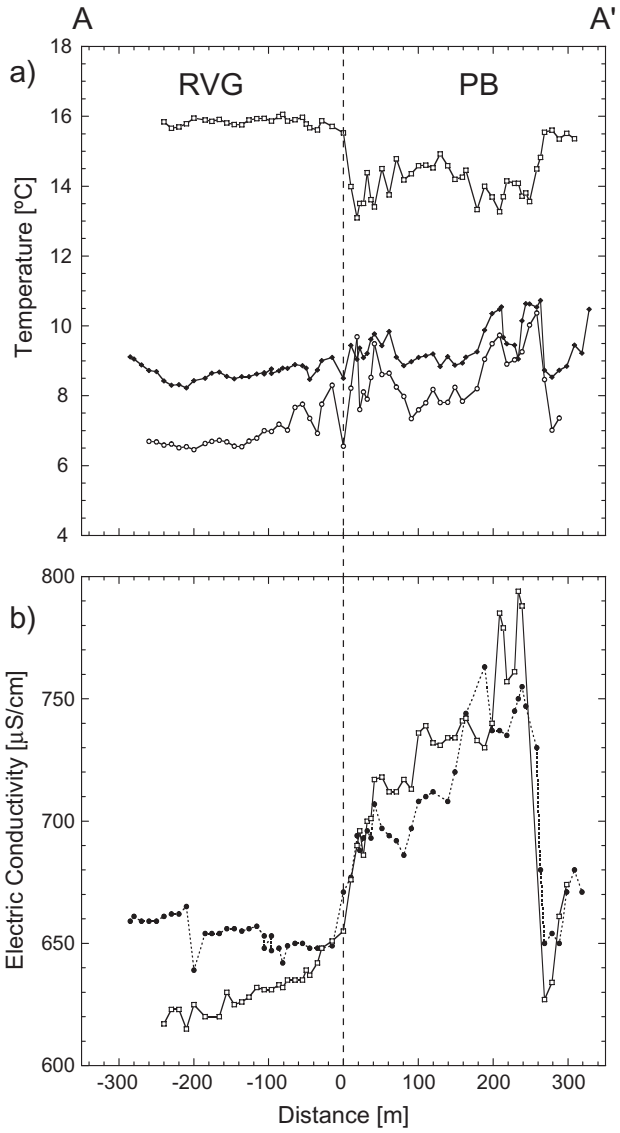

Figure 4.8: *a*) Horizontal profiles of the soil temperature at a depth of 0.5 m below the ditch along section A-A'. *b*) EC of the water in the ditch at the same locations in March (●), September (□) and January (○). The vertical dashed line indicates the location of the PBFZ. The sites on the PB where strong temperature anomalies are observed largely correlate with patterns in the distribution of EC in the ditch which suggests that at these locations discharge of relatively highly mineralized ground water occurs.

tude of seasonal temperature variation at shallow depth. Especially on the hanging wall (RVG), seasonal temperature variations are notably larger than on the higher, and wetter areas upstream of the fault scarp. As a result, the temperatures on the PB are anomalously low compared to the lower lying areas during summer (September) while in winter time (January) groundwater temperatures in the wet areas on the PB are up to $2\ ^{\circ}\mathrm{C}$ warmer. Figure 4.8 shows that the areas which show the least seasonal variation in temperature coincide with locations where relative strongly mineralized water (high EC) flows into the ditch, which suggests that these places are the locus of enhanced upward groundwater flow.

Figure 4.9 shows how the observed temperature anomalies and their reversal from summer to winter can be qualitatively understood from the interaction between the seasonal temperature variation at the surface and the groundwater flow regime just below the ditch. In the top $\sim 5\ \mathrm{m}$ of the sub-surface, vertical temperature gradients are very large compared to the background geothermal gradient. This is especially true during summer and winter. Infiltration and exfiltration of groundwater cause the vertical temperature profile to be deflected downward and upward, respectively, as a result of advection of heat [*e.g. Constantz et al.*, 2003, Figure 4.9]. Due to the high near-surface temperature gradient, relatively small lateral differences in infiltration or exfiltration rates can cause groundwater temperature close to the surface to vary considerably laterally. Comparison of the depicted temperature profiles for infiltration and exfiltration (Figure 4.9) demonstrates that during winter time a zone of exfiltrating groundwater causes a positive temperature anomaly, whereas in summer time a negative anomaly is produced. These reversals are apparent in Figure 4.8.

The results of the EC routing carried out in March and September 2002 yield comparable patterns (Figure 4.8b). The EC of water in the ditch along A-A' in the RVG averages around 600-650 $\mu S/\mathrm{cm}$ while on the PB the EC of the water in same ditch varies between 700-750 $\mu S/\mathrm{cm}$. The fault scarp forms the abrupt boundary separating these two domains. A lower EC downstream is due to the fact that dissolved solids are rapidly oxidized immediately after the discharging water reaches the surface. An even more pronounced contrast between the PB and RVG is found in the EC measurements of the groundwater samples from the shallow filters of wells p61 & p65 (Table 4.1). Mixing of high EC groundwater with surface water with a low EC smoothes the differences between the PB and RVG in the ditch water. Therefore, the contrast between the PB and RVG section of the ditch is larger by the end of the summer (September) when the surface water contribution from upstream areas is relatively small.

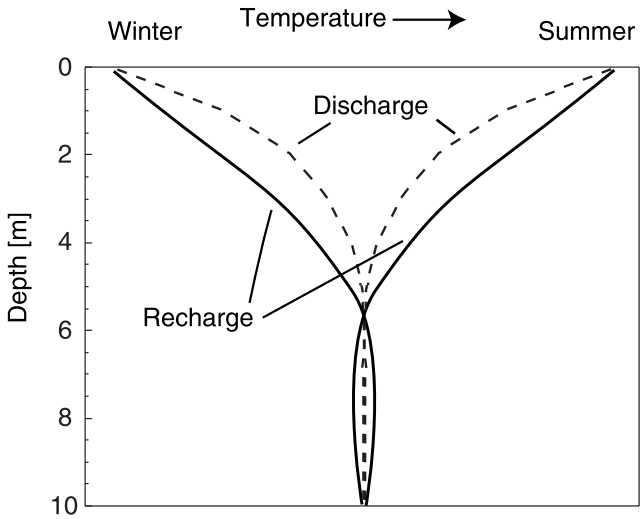

Figure 4.9: Qualitative sketch showing the difference in vertical temperature gradients between an area of exfiltration and infiltration during winter and summer. Relative small differences of the temperature gradient near the surface as a result of advective heat transport through vertical groundwater flow will result in significant temperature anomalies in horizontal profiles of groundwater temperature.

Sample	*Depth* [m below surface]	*EC* [$\mu S/\mathrm{cm}$]
p65-1	3.5	463
p65-2	17	885
p65-3	54	357
p61-1	3	856
p61-2	15	697
p61-3	24	365

Table 4.1: Electric Conductivity of groundwater samples from well p65 & p61

4.5 Numerical modeling

In this section, the individual field data that are discussed above are brought together in a numerical simulation of the system. Therefore, the model was set-up to yield the general characteristics of the field site based upon reasonable parameter values. The model describes both the relatively small scale phenomena associated with the interaction of shallow groundwater flow and seasonal temperature fluctuations close to the surface that are recorded in the horizontal profiles of temperature, and the deeper temperature data from the temperature-depth profiles that yield information on the larger-scale groundwater flow patterns. The aim of the model was to test the validity of the interpretations that were proposed in the latter section in a consistent framework. Therefore, not much emphasis was put on optimization and calibration. The modeling was carried out using a generic Finite Element modeling tool (FlexPDE software [*PDE Solutions*, 2003]) that is used for the coupled solution of the governing equations.

A 2D vertical cross-sectional model was constructed along A-A' in which a source term accounts for lateral inflow towards the ditch perpendicular the model section. The latter occurs because the ditch is draining and recharging below and above the fault, respectively. Figure 4.10 shows part of the complete model domain that is $1250\,\mathrm{m}$ long and $400\,\mathrm{m}$ high. Groundwater flow in the sectional model is in quasi steady-state, only varying over time as a result of the temperature dependency of hydraulic conductivity, K $[\mathrm{m/s}]$. The hydraulic boundary conditions are constant. The temperature regime is transient as both the seasonal fluctuation of temperature at the surface and the longer term annual variation of the mean surface temperature are implemented.

4.5.1 Groundwater flow

The following equation is used to model steady state flow in the model section (unit thickness):

$$\nabla \cdot \vec{q} + q_{lat} = 0 \tag{4.2}$$

where $\vec{q}\,[\mathrm{m/s}]$ is the Darcy velocity and q_{lat} $[\mathrm{s}^{-1}]$ is the two-sided (total) lateral inflow perpendicular to the section. The nabla operator (∇) applies to the 2D section only.

Groundwater flow is towards the ditch on the PB, draining the underlying aquifer and away from the ditch (recharging the aquifer) in the RVG. Therefore, two different values for the lateral inflow towards the section via the ditch, $q_{lat,PB}$ and $q_{lat,RVG}$, were defined for the PB and RVG respectively.

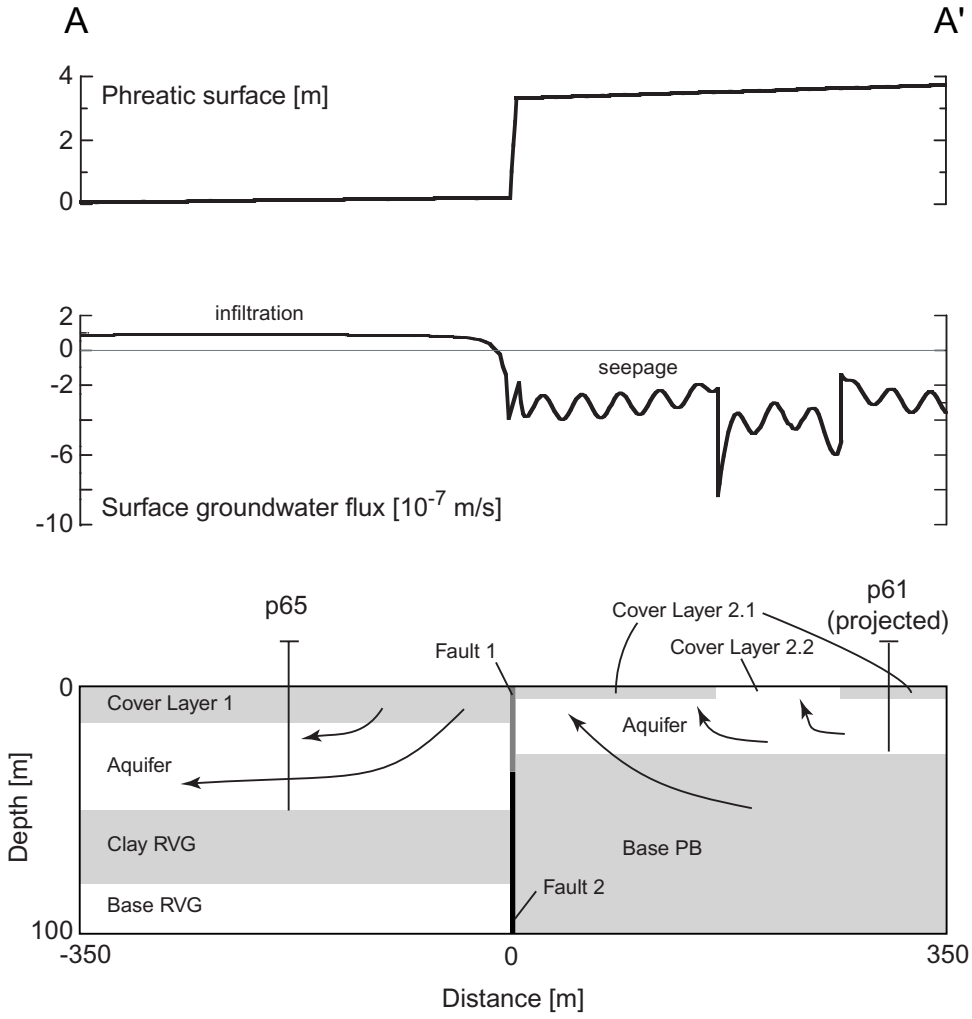

Figure 4.10: Hydrogeological cross-section over the PBFZ along A-A' showing the groundwater flow patterns in the model, the phreatic groundwater level (the upper boundary condition of the numerical simulation) and the resulting groundwater flux at the surface.

Unit	*Description*	*Permeability* (k)
Aquifer	Coarse Sand	$4.62 \cdot 10^{-11}$
Cover layer 1	Fine Sand - aeolian	$1.5 \cdot 10^{-11}$
Cover layer 2.1	Fine Sand - aeolian	2.9 - $4.8 \cdot 10^{-12}$
Cover layer 2.2	Medium Sand	1.2 - $1.9 \cdot 10^{-11}$
Clay RVG	Clay	$1.5 \cdot 10^{-16}$
Base RVG	Sand	$1.5 \cdot 10^{-11}$
Base PB	Fine Sand - marine	$2 \cdot 10^{-12}$
Fault 1	Mixture of Clay and Sand	$7.7 \cdot 10^{-14}$
Fault 2	Mixture of Clay and Sand	$2.7 \cdot 10^{-15}$

Table 4.2: Permeability (k) values used in the numerical simulation. Unit names refer to Figure 4.10.

Darcy's Law is implemented as:

$$\vec{q} = -K \nabla h \tag{4.3}$$

where h [m] denotes hydraulic head. Hydraulic conductivity is defined as $K = k\frac{\rho_w g}{\mu}$ in which k is intrinsic permeability [m^2], $\rho_w = 1000\ \mathrm{kg/m^3}$ is the density of water, $g = 9.81\ \mathrm{m/s^2}$ is the gravitational acceleration constant and $\mu = 1.22 \cdot 10^{-3}$ $\mathrm{Ns/m^2}$ is the dynamic viscosity of water (at $13\ ^\circ\mathrm{C}$). The temperature dependency of μ is explicitly taken into account . Values of μ and, hence, K vary by a factor of two in the model because near surface groundwater temperature ranges from about $3\ ^\circ\mathrm{C}$ to $18\ ^\circ\mathrm{C}$. Although the density of water, ρ_w, is also a function of temperature, the temperature effect on ρ_f in the same temperature range is only $\sim 2\ ‰$.

Hydraulic head is fixed at the top of the model following the hydraulic gradients that were measured in earlier studies [*Stuurman and Atari*, 1997; *Bense et al.*, 2003a] (upper panel in Figure 4.10). The left- and right-hand side of the model domain are constant head boundaries with a value in accordance with the upper boundary condition so that over the left and right boundaries flow is horizontal.

Table 4.2 summarizes the hydraulic properties of the units, as used in he simulations. Only a few direct field measurements of the hydraulic properties of the different hydrogeological units are available for the study area. Here parameter values are used that were compiled from earlier studies [*Bense et al.*, 2003a; *Stuurman and Atari*, 1997]. The top-layer on the PB is assigned an heterogeneous permeability distribution using a sine-function distribution ($k = 2.9 \cdot 10^{-12}\mathrm{m}^2$ to $4.8 \cdot 10^{-12}\mathrm{m}^2$). A zone of higher permeability ($k = 1.2 \cdot 10^{-11}\mathrm{m}^2$ to $1.9 \cdot 10^{-11}\mathrm{m}^2$) is modeled within the top-layer. The amount of heterogeneity in the top layer of the model on the

PB is regarded to be reasonable as it is in the same range as reported by *Bierkens* [1994] based upon laboratory measurements on similar sediments. The fault zone is schematized as a five-meter wide zone with a width w [m] of low permeability that has a resistance r [day] defined as $\frac{w}{K}$. The upper ($z < 30$ m) and lower part of the PBFZ are assigned values of r_1 (Fault 1) and r_2 (Fault 2), respectively. This distinction has been made because it is likely that the resistance of the PBFZ significantly increases with depth. The borehole records for b64 & b62 (Figure 4.1) show that no clay is present in the upper part of the stratigraphy which makes it unlikely that in the upper part ($z < 30$ m) of the system clay smearing has occurred along the fault plane. It is shown in Chapter 2 that r_1 can be estimated as $\sim$100 days based upon an analysis of hydraulic head gradients on either side of the fault which is the value that is used in the present study.

4.5.2 Heat transport

The following equation is used for the simultaneous transfer of heat and fluid through heat conduction and advection in an isotropic and homogeneous medium [e.g *Stallman*, 1960]:

$$c\rho\frac{\partial T}{\partial t} + c_w\rho_w\vec{q}\nabla T + c_w\rho_w T_{lat}q_{lat} - \kappa\nabla^2 T = 0 \tag{4.4}$$

in which the term $c_w\rho_w T_{lat}q_{lat}$ represents the source term to count for the lateral inflow of water with temperature T_{lat} perpendicular to the modeled section. The operators ∇ and ∇^2 apply to the 2D section only.

At the base of the model domain ($z = 400$ m) temperature is fixed at 20 °C, following a geothermal gradient of ~ 25 °C/km, which is in accordance with values recorded in deeper wells [*Stolk*, 2000]. This gradient corresponds to a heat flow of $2.5 \cdot 0.025 = 62.5$ mW/m^2 for $\kappa = 2.5$ W/m°C which is in reasonable agreement with published heat flow data for the Netherlands [*e.g. Van Balen et al.*, 2002]. The left and right sides of the model domain were assigned a linear thermal gradient. The temperature of the water in- or out-flowing perpendicular to the section (q_{lat}) is assumed to equal the temperature in the section so that ($T_{lat} \approx T$). Hence, the effect of possible heat conduction perpendicular to the section is not taken into account in the present model.

The distribution of thermal properties in the model was assumed to be homogeneous. Representative values for these sediments were used as given by *De Jong and Geirnaert* [1979] and subsequently *Stolk* [2000] which yield $\kappa = 2.5$ W/m°C, $c = 2013$ J/kg°C, $\rho = 2105$ kg/m^3.

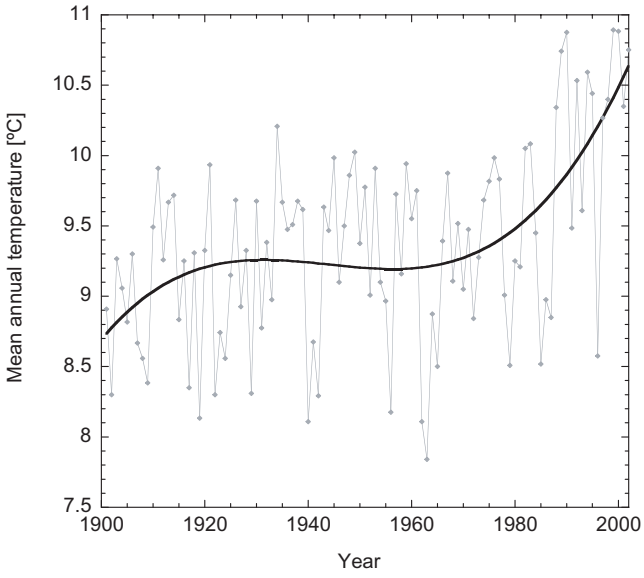

Figure 4.11: The mean annual air temperature as recorded at the De Bilt meteorological station (see Figure 4.1 for location). The solid line is a polynomial fit of the data. Up to the year 1960 this trend line is used to mimic surface temperature in the numerical model. Thereafter, the actual mean annual temperatures are used to constrain the simulation of the temperature field around the PBFZ.

4.5.3 Modeling strategy

Transient model calculations start for the year 1900. Initial conditions are obtained by calculating a steady-state temperature field using a surface temperature representative for the year 1900 based upon the available meteorological record of air temperature at De Bilt meteorological station (Figure 4.11). Subsequently the surface temperature is allowed to increase following the trend in mean annual air temperature up to the year 1960. Proceeding from that date, the history of the annual average temperature ($\overline{T}$) is used in a stepwise manner to forward calculate the temperature field up to the year 2000.

Surface temperature (T_s) for the year 2001 and 2002 is represented by a sine-function:

$$T_s = \overline{T} + \Delta T_s \sin 2\pi t/\tau \tag{4.5}$$

in which the value for the amplitude of annual surface temperature variation (ΔT_s)

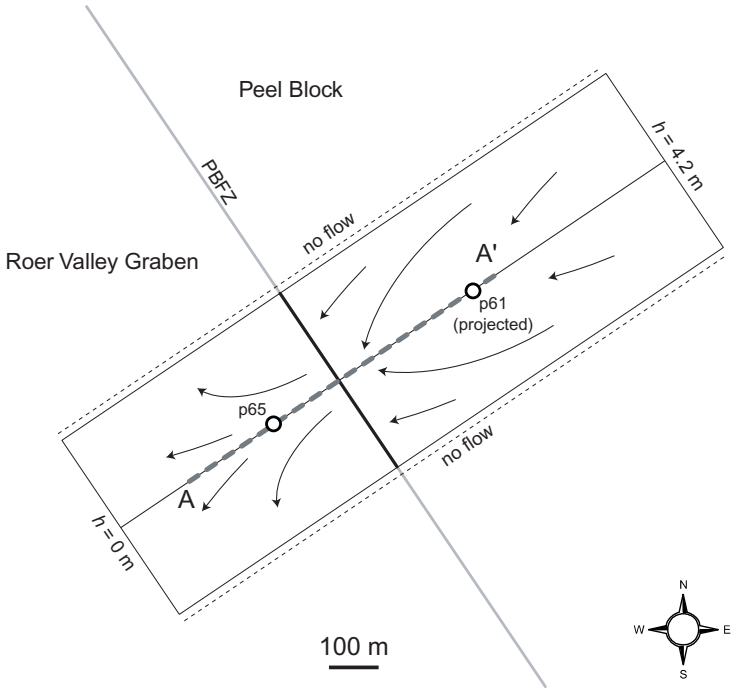

Figure 4.12: Mapview of the schematized groundwater flow system at the field site with the hydraulic boundary conditions of the groundwater flow model used to estimate the groundwater flux towards the ditch along A-A'.

was chosen in agreement with observed temperature records at De Bilt meteorological station.

The values of permeability and thermal properties of the hydrogeologic units were fixed in the model. Only the values for $q_{lat,PB}$ and $q_{lat,RVG}$ were optimized using "trial and error" by visual comparison between observed and simulated temperatures. No simultaneous optimization of both temperature data and hydraulic heads has been carried out by for example *Woodbury and Smith* [1988] or *Bravo et al.* [2002]. The middle panel in Figure 4.10 shows the resulting flux of groundwater at the surface.

It was tested whether the optimized values of $q_{lat,RVG}$ and $q_{lat,PB}$ are reasonable in the context of the local groundwater flow pattern as shown in Figure 4.12. Therefore, a simple 3D groundwater flow model was constructed of which the boundary conditions and extent are shown in Figure 4.12. The model consisted of three domains; RVG, PBFZ and PB of which each was assigned a representative

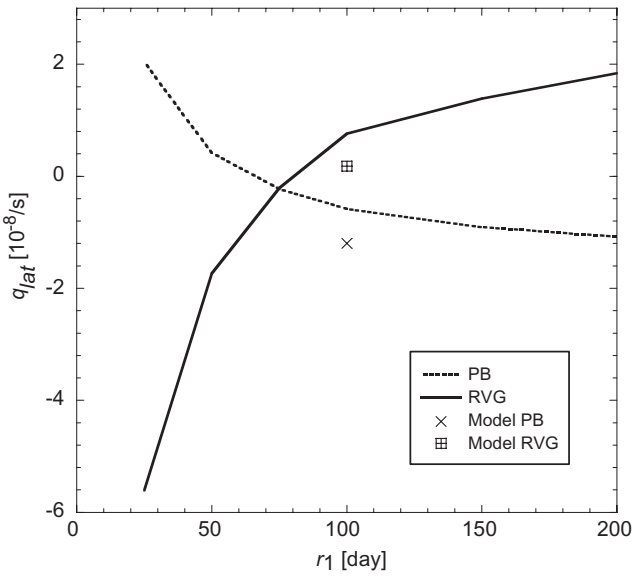

Figure 4.13: The variation of lateral inflow into the ditch ($\vec{q}_{lat}$) for the aquifer on the RVG and PB as a function of the fault resistance (r_1) as calculated using the secondary groundwater flow model. Also indicated are the values for $\vec{q}_{lat,RVG}$ and $\vec{q}_{lat,PB}$ that are used in the simulation.

hydraulic transmissivity (the product of the vertically averaged K and the thickness of the aquifer) which was calculated using the "Cover Layer" and "Aquifer" unit for the RVG and PB, and "Fault1" for the PBFZ.

The total amount of calculated in / outflow to / from the ditch has been averaged along the length and height of the aquifer for the up- ($q_{lat,PB}$) and downstream part ($q_{lat,RVG}$) respectively. Figure 4.13 shows the calculated rates of in / out flow to the ditch as a function of r_1. In case r_1 is low (<75 days) infiltration occurs on the PB and groundwater discharge occurs in the lower lying areas in the RVG. For values of r_1 above ~ 75 days, groundwater discharge will occur in the higher areas while infiltration is starting to occur in the lower lying areas. Figure 4.13 shows that the optimized values for $q_{lat,RVG}$ and $q_{lat,PB}$ for $r_1 = 100$ days can be regarded as reasonable estimates as they fairly close match those inferred from the 3D groundwater flow model.

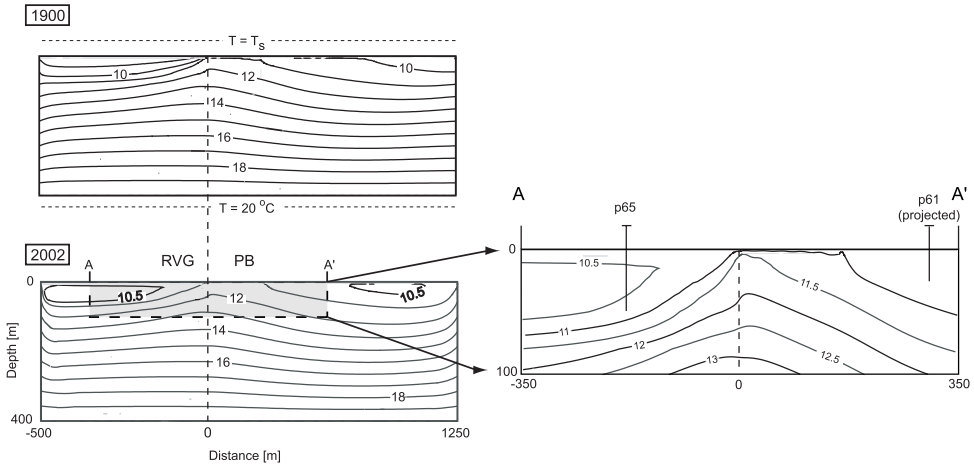

Figure 4.14: Temperature distribution (isotherms are labeled in °C) in the absence of seasonal temperature variation at the surface as calculated for the year 1900 and 2002 for the entire model domain. The PBFZ is located along the dashed line. The grey area indicates the extent of the cross-section shown in Figure 4.10.

4.6 Results and discussion

The upper panel in Figure 4.14 shows the initial steady state temperature distribution for the year 1900. Upward groundwater flow on the PB as a result of the low-permeable fault zone causes the temperatures to be higher there than at the same depth in the RVG. The lower panel in Figure 4.14 shows the calculated temperature distribution for the year 2002 in the absence of seasonal annual variations of surface temperature. As a result of surface warming over the last century, the thermal contrast between discharge area and recharge area is dramatically reduced.

In order to be able to compare the field data to the simulation results, observation well p61 is projected onto A-A'. Since well p61 is located along the ditch north of A-A' (Figure 4.1), it is assumed that similar groundwater flow conditions are met at well p61 as around the ditch along A-A' at the same distance from the fault scarp.

Comparison with the field data (Figure 4.15) shows that the shape of the deeper observed temperature-depth profiles can be reasonably well explained by a net increase in mean annual surface temperature as recorded in the meteorological record from De Bilt in combination with the estimated rates of groundwater flow in the system. However, it appears that the temperature in the upper part of the system is generally higher (several tenth's of a °C) than the model prediction. This effect

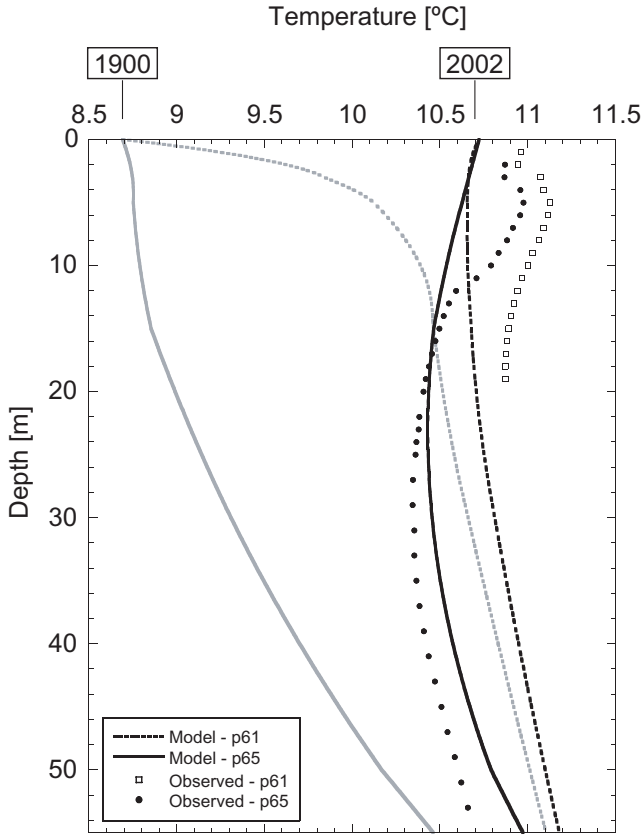

Figure 4.15: A comparison of the observed temperature-depth profiles in the absence of seasonal temperature variation at the surface, with the results of the simulation shows that in the upper part of the profiles the simulated temperatures are too low relative to the observed patterns. Several reasons to explain this discrepancy are discussed in the text.

is stronger for the discharge area (p61) than for the recharge area (p65). As the signal of the seasonal variations largely overprints these deviations, results improve when the seasonally fluctuating surface temperature is implemented in the simulation. The amplitude and damping with depth of the simulated temperature-depth profiles compare well to the observed data from well p61 & p65 (Figure 4.16).

Several reasons can be considered for the observed differences between calculated and observed temperatures at shallow depth ($<10\,\mathrm{m}$). First, De Bilt meteorological station is located at $\sim 50\,\mathrm{km}$ lateral distance from the field site where the mean annual surface temperature is not necessary representative for that around

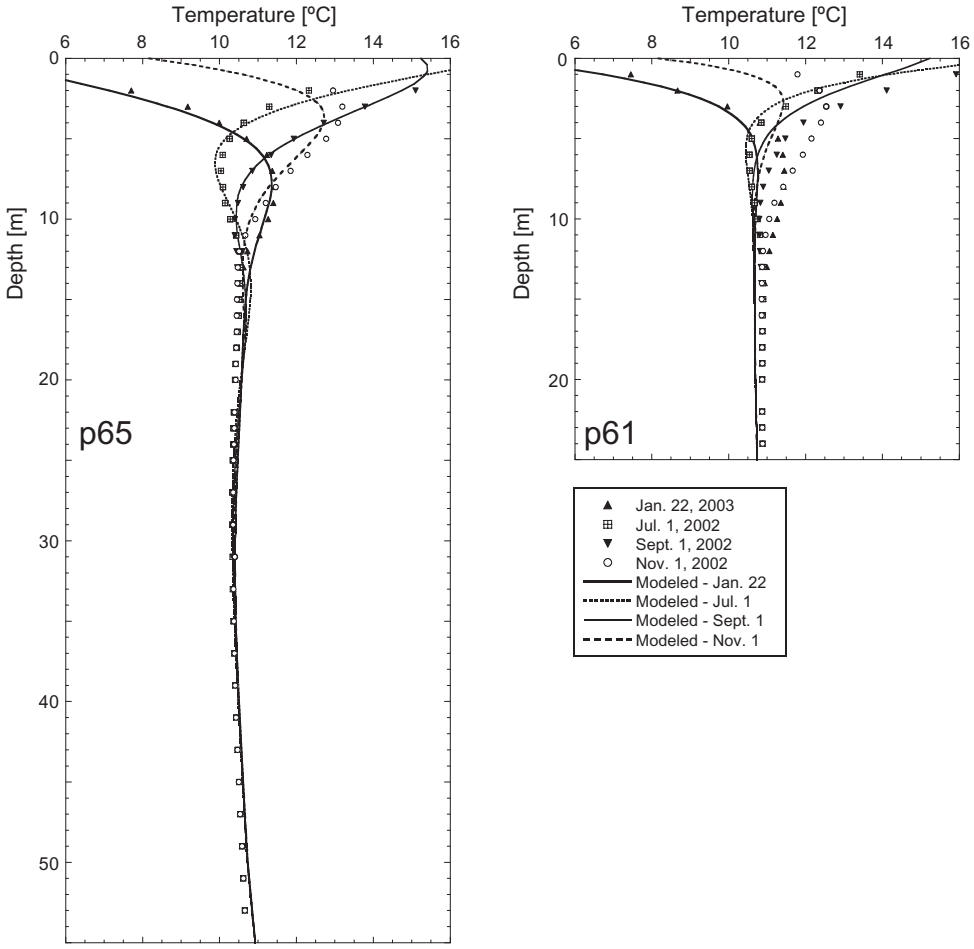

Figure 4.16: Model-data comparison of temperature-depth data in which the seasonal surface temperature variation is included. The seasonally fluctuating surface temperature is mimicked using a sine-function with amplitude, mean and phase-shift in accordance to observations at De Bilt meteorological station.

Uden. However, based upon an inspection of maps of regional variation of mean annual temperatures in the Netherlands at the Royal Meteorological Institute of the Netherlands, this effect must be of minor impact. Probably of more importance is the effect that there can exist a significant difference between the air temperature as documented in meteorological records and the soil-temperature as recorded in the geothermal record [*e.g. Putnam and Chapman*, 1996; *Beltrami*, 2001]. Several studies have shown that changes in either vegetation cover or groundwater depth can significantly impact soil temperature [*Lewis and Wang*, 1998; *Taniguchi et al.*, 1999b]. Another effect is that groundwater flow will become transient if for example the intensities of groundwater seepage and recharge differ significantly between winter and summer, which will induce additional disturbances of the geothermal regime. Moreover, in case the surface temperature is significantly different from the sine function that is applied in the simulation, if for example during periods of snow cover temperature is fixed at $0\ ^{\circ}\mathrm{C}$ deviations between simulated and observed temperatures can be expected [*Lapham*, 1989]. The present model does not include any of these processes that possibly explain the observed misfits in the upper part of the profiles because groundwater flow is kept stationary over the season, the aquifer is assumed to be saturated, local effects of vegetation cover are not considered and the surface temperature is simulated as to vary sinusoidally over the season.

The synthetic sections of horizontal soil temperature at a depth of $50\ \mathrm{cm}$ show the same inversion over the season as observed in the field data set, which supports the initial analysis of the observed patterns (Figure 4.17). As the thermal properties in the model are uniform, the simulated temperature patterns are solely the result of differences vertical groundwater flow close to the surface (Figure 4.10). In reality, the thermal properties of the aquifer will slightly vary laterally. Preliminary modelling results show that, in case of extreme, unrealistic, lateral contrasts of the thermal conductivity of the cover layer ($\kappa = 1$ to 4 $\mathrm{W}/^{\circ}\mathrm{Cm}$), these lateral variations can be reflected in temperature anomalies with a comparable magnitude as observed around the PBFZ. However, the sediments around the PBFZ are believed to be relatively homogeneous and since a strong correlation between EC anomalies and shallow temperature patterns was observed it is believed that the observed temperature anomalies close to the surface are mainly caused by differences in vertical groundwater flow.

The depth at which measurements are carried out with the described method of horizontal profiling is of considerable importance. Figure 4.9 illustrates that the amplitude of temperature anomalies due to the interaction of lateral variations in groundwater flow and seasonal surface temperature change increase in the first

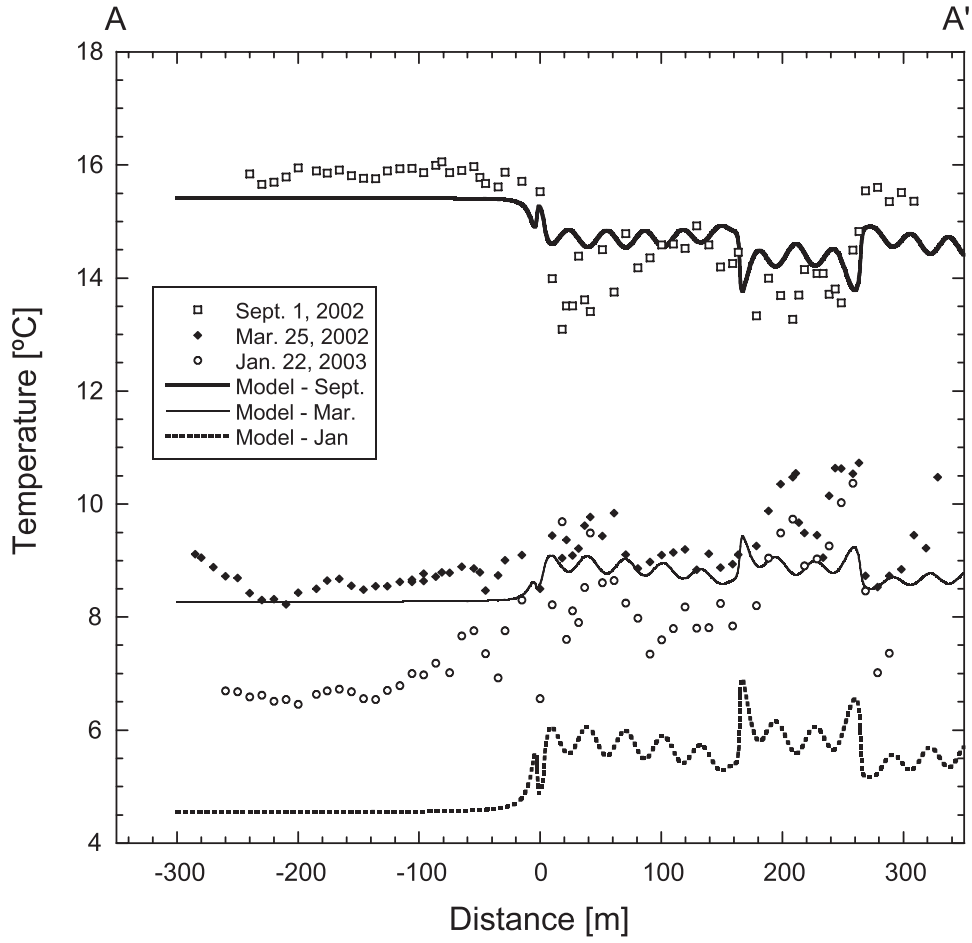

Figure 4.17: Model-data comparison of the horizontal temperature profiles along A-A' at a depth of 50 cm below the surface. The heterogeneity of the groundwater flow field can reasonably explain the observed temperature anomalies and their reversal over the season.

meters below ground surface and that an optimal depth of measurement exists. Ideally, measurements should just reflect the interaction between seasonal surface temperature changes and groundwater flow without complications by temperature signals associated with diurnal surface temperature changes. Measurement at relatively large depth has the additional advantage that relatively short-term surface temperature variations that are superimposed on the seasonal signal are largely damped. In the current study, the employed measurement depth of $0.5\ \mathrm{m}$ apparently sufficed to bring out anomalies that are the result of interaction between groundwater flow and seasonal temperature change. These considerations are useful in choosing an appropriate depth of measurement in a field campaign. Detailed meteorological, rather than simple sine-functions, records may be incorporated in numerical modeling to refine the interpretation of seepage and infiltration rates, rather than representing surface temperature by a simple sine function.

4.7 Conclusion

The geothermal regime around a shallow fault zone in the Netherlands was simulated by incorporating into one model both a seasonally fluctuating surface temperature as well as the longer term surface warming over the last century . The present study shows how complex transient geothermal patterns at shallow depth can be understood by coupling transient heat transport to steady-state groundwater flow. It is shown that for a correct simulation of the observed geothermal patterns at larger depth it is essential to incorporate the impact of recent surface warming in the numerical model. Constraining the simulation with observed meteorological data showed that there is a significant discrepancy between air temperature and the ground surface temperature that is recorded in the geothermal regime, a finding which has been reported in other studies.

In the present study it is shown that subtle variations in groundwater flow velocities ($\sim$2 to $4 \cdot 10^{-7}\mathrm{m/s}$) close to the surface produce significant ($\sim 0.5\ ^{\circ}\mathrm{C}$) temperature anomalies as a result of the interaction of seasonal surface temperature variation and groundwater flow. Therefore, horizontal profiles of shallow groundwater temperature should be a promising tool to asses the small scale heterogeneity of surface-groundwater interaction which is a key issue in for example wetland research [*e.g. Hunt et al.*, 1997, 1998; *Bravo et al.*, 2002] and more general hydrologic studies concerning the estimation of water budgets, groundwater recharge and groundwater quality [*e.g. Silliman et al.*, 1995]. A field method based upon this mechanism provides an important extension to existing methods since shallow horizontal temperature profiling can be used, unlike the other available methodologies

that rely on elaborate field instrumentation at selected sites, to carry out extensive regional mapping in large detail. Such an approach may, therefore, be employed in the prospecting of key zones of groundwater discharge or recharge that are so essential to the management of a variety of groundwater systems that are dominated by hydrogeological heterogeneity and associated preferential flow of groundwater and dissolved contaminants or nutrients.

5

The effect of fault relay and clay smearing on groundwater flow patterns in the Lower Rhine Embayment

Abstract

Faults strongly impact groundwater flow in the unconsolidated sediments of the Lower Rhine Embayment. Hydraulic head maps show that many individual faults form a barrier to fluid flow while relay structures in these faults are sites of hydraulic contact between otherwise separated aquifers. The fluid flow patterns around the Rurrand Fault close to the largest open pit mine in the Lower Rhine Embayment is one of the first well documented examples of fluid flow around a fault relay zone. The effect of clay smearing could be quantified using the Shale Gouge Ratio (SGR) method which is common in hydrocarbon related studies but has not been applied to groundwater flow data so far. The effect of fault relay zones on groundwater flow is analyzed using numerical simulations. It is concluded that fault relay needs special consideration in the evaluation of the sealing capacities of faults in sedimentary basins. Moreover, it is demonstrated that the SGR-methodology is a promising tool for the estimation of fault zone hydraulic properties in hydrogeological modeling.

This Chapter is largely based upon: Bense, V. F. and R.T. Van Balen, The effect of fault relay and clay smearing on groundwater flow patterns in the Lower Rhine Embayment, *Basin Research*, 16, p.397-411, 2004.

5.1 Introduction

Faults have an important role in the distribution of fluids, hydrocarbons and groundwater in sedimentary basins [e.g *Smith*, 1980; *Knipe*, 1993; *Aydin*, 2000]. Recent studies show the impact of faults to groundwater flow patterns at shallow depth in the Roer Valley Rift System (RVRS) [*e.g.* <500 m; *Bense et al.*, 2003a]. The hydraulic behavior of faults cutting through unconsolidated sediments at shallow depth is likely to be different from that of faults at depths where rocks are lithified (>1000 m) as fault permeability is a function of burial depth and the rheological properties (*e.g.* strength) of the faulted rock [*Rawling et al.*, 2001; *Bense et al.*, 2003b]. Moreover, the heterogeneous and anisotropic distribution of permeability in fault zones is difficult to characterize and needs extensive field studies. Therefore, the development of generic models of fault zone hydrology remains elusive. Recent empirical representations of fault properties to predict fault zone in petroleum reservoir models has shown promise [*e.g. Fristad et al.*, 1997; *Yielding et al.*, 1999; *Harris et al.*, 2002]. The Shale Gouge Ratio is one of the most widely applied of these algorithms relating the clay- or shale content of the faulted lithology and fault throw [*e.g. Yielding et al.*, 1997; *Freeman et al.*, 1998]. *Doughty* [2003] calculated fault zone parameters for an exhumed fault in the Rio Grande Rift, New Mexico, and argued that of all available algorithms the SGR-algorithm is best capable of predicting fault zone hydraulic properties on the outcrop scale, although this was not rigorously tested.

The area of the Lower Rhine Embayment (LRE) is the southward continuation of the RVRS. These rift systems are part of the Neogene Rift System in western Europe that also comprises the Upper Rhine Graben [*Ziegler*, 1994; *Michon et al.*, 2003]. Figure 5.1 shows an overview map of the LRE. On many places in the RVRS and the LRE faults form strong barriers to fluid flow [*Wallbraun*, 1992; *Bense et al.*, 2003a; *Bense and Van Balen*, 2003]. Field studies [*Ernst and De Ridder*, 1960; *Lehner and Pilaar*, 1997; *Bense et al.*, 2003b] show that clay smearing along the fault plane is the most important mechanism to account for the observed low permeability of faults in the RVRS and LRE. Despite the sealing properties of faults in these areas, there are locations where there exists lateral hydraulic continuity between otherwise compartmentalized aquifers. These locations are found to coincide with relay zones that exist where fault zones have an *en échelon* structure of over-stepping segments.

In this Chapter the SGR-approach is used to predict fault zone hydraulic properties, based upon geological and groundwater flow data around the Rheindahlen Fault situated in the LRE. Values of SGR are calculated at four locations along the Rheindahlen fault in the LRE which are compared to observed hydraulic head

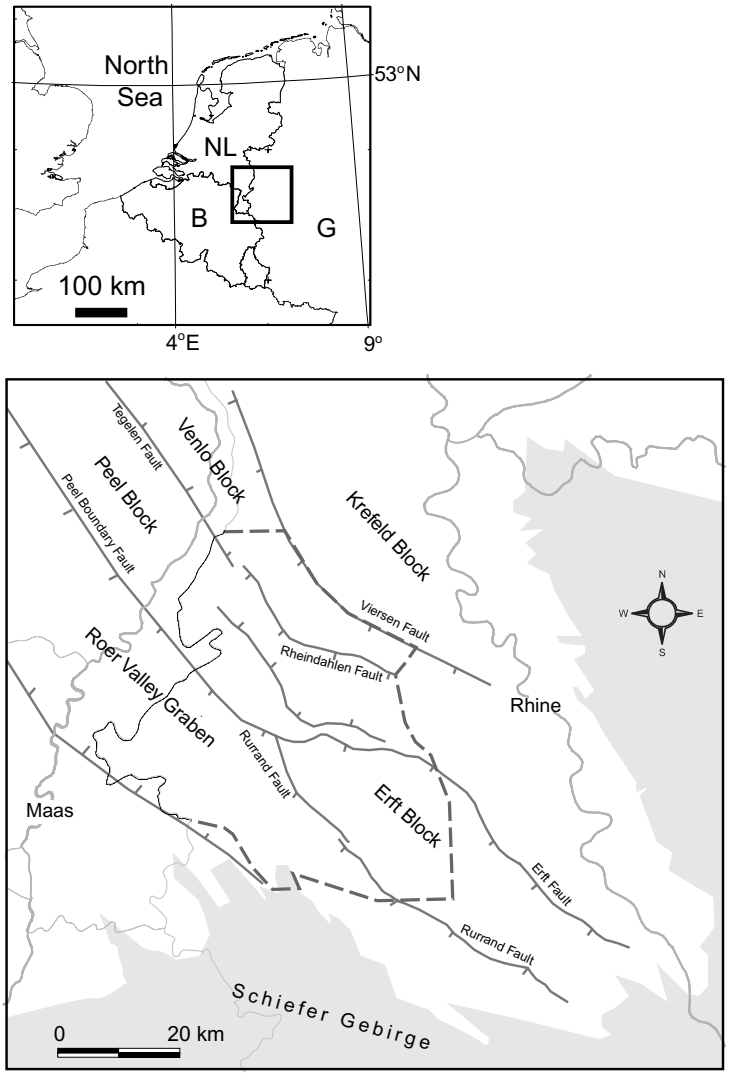

Figure 5.1: Tectonic overview map of the Lower Rhine Embayment with the locations of the tectonic blocks and faults as mentioned in the text. The grey area represents the Schiefer Gebirge (NL = The Netherlands, G = Germany, B = Belgium, R = Rhine River, M = Maas River). The dashed line indicates the extent of Figure 5.5.

differences across the fault zone. In addition to this analysis, groundwater flow simulations were carried out to better understand the effect of fault relay structures on groundwater flow. The results of these simulations are compared with the observed groundwater flow field around the "Hambach" open pit mine that is located close to a regionally important relay zone in the Rurrand fault. Around this relay zone the groundwater flow is exceptionally well constrained as a result of a very dense network of groundwater flow observation wells.

In the next sections, first the geological setting of the LRE is described and a background on the hydrological impact of fault zone processes (e.g. clay smearing) and fault segmentation in unconsolidated sediments, is provided. Subsequently, the groundwater flow patterns in the LRE are discussed in relation to faults. Based upon this discussion the two case-studies will be introduced, which are further analyzed in this Chapter.

5.2 Geological setting of the Lower Rhine Embayment

The LRE has formed at the northwestern margin of the Schiefergebirge (Figure 5.1). Subsidence took place along NW-SE trending faults. During the Tertiary a thick sediment pile was deposited consisting of shallow-marine sand [*Schäfer et al.*, 1996]. During the Miocene, a coastal plain with swamps and forests developed. The peat layers that formed during this period are today mined as lignite in large open pits. During the Pliocene, the North Sea retreated further and fluvial systems developed which were dominated by the Rhine River. Basin subsidence ceased, tectonic uplift took place and fluvial terrace gravel spread widely to cover the area. Figure 5.2 shows the lithological units which comprise the Venlo Block (for location see Figure 5.1)

The normal-faults that developed in this extensional regime are syn-sedimentary (*i.e.* fault throw increases with depth). The Rurrand Fault, which is known as the Peel Boundary Fault in the Dutch part of the system, separates the Roer Valley Graben from the Peel Block in the north and the Erft Block in the south. The Venlo Graben north of the Peel Block is delineated by the Wegberg Fault in the south (in the Netherlands known as the Tegelen Fault) and the Viersen Fault in the northeast.

5.3 The impact of faults on fluid flow

The most direct impact of faults on fluid flow is that, as a result of fault throw, confining units can be juxtaposed against aquifers resulting in a blocking of fluid

Name & Description	Age	Maximum Thickness [m]	V_{clay} [%]	ID
Gravels and coarse sands	Late-Pleistocene & Holocene	40	5	Q
Tegelen and Reuver Clay	Late Pliocene - Early Pleistocene	20	80	TR
Hauptkies	Late Miocene - Early Pliocene	80	5 - 60	8
Neurather Sand	Middle Miocene	180	5 - 60	6D
Frimmersdorf Lignite		20	30	6C
Sand		50	5 - 60	6B
Mörken Lignite		50	30	6A
Cologne Sand	Early Miocene	> 100	5 - 60	5

Figure 5.2: General stratigraphical column of geological and corresponding hydrological units discerned on the Venlo Block. V_{clay} is the typical volumetric clay content.

flow. Two additional aspects of faults that can have a strong impact on fluid flow are discussed in the following paragraphs. These are (1) tectonic processes (deformation) along the fault plane that impact the fault zone hydraulic properties and (2) the impact of horizontal and vertical segmentation of faults on fluid flow around the fault zone.

5.3.1 Fault zone processes

In sedimentary successions where clay or shale layers are present, dragging or ductile flow of these layers along the fault plane between the up- and down-thrown source beds, can result in a clay smear along the fault plane [*e.g. Smith*, 1980; *Knipe*, 1993; *Lindsay et al.*, 1993; *Fulljames et al.*, 1997]. Clay smearing is a process that can strongly reduce the effective hydraulic conductivity of a fault zone [*e.g. Takahashi*, 2003]. Field studies in the open pit lignite mines [*Lehner and Pilaar*, 1997] and a trenched outcrop over the Geleen Fault show that clay smearing is occurring along faults in the RVRS as well [*Houtgast et al.*, 2002; *Bense et al.*, 2003b, Chapter 3]. How-

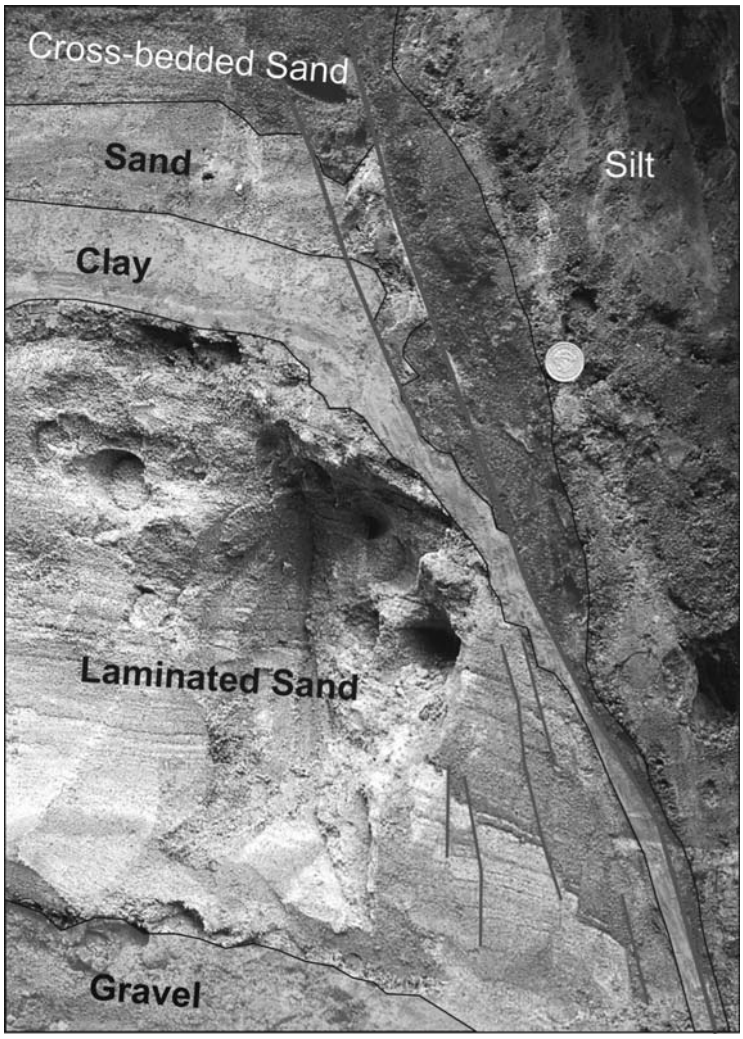

Figure 5.3: Clay smear in unconsolidated sediments in a trenched outcrop over a secondary fault in the Roer Valley Rift System. The coin has a diameter of 2 cm.

ever, the latter studies show that next to clay smearing, drag or injection of sand and gravel along the fault plane also occurs (Figure 5.3).

Because both clay and sand can be dragged into the narrow fault core, the permeability of the fault core is expected to be strongly anisotropic so that it is enhanced along the fault plane while perpendicular to the fault plane permeability

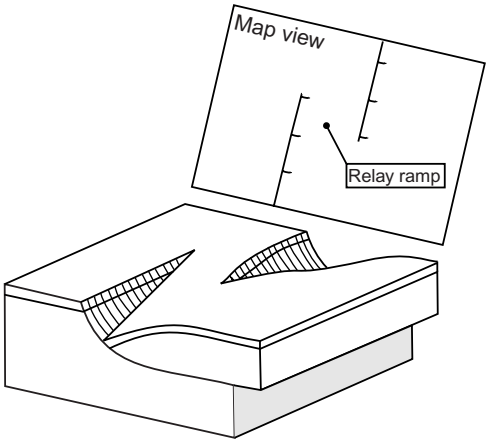

Figure 5.4: Overstepping fault segments are separated by a relay zone [redrawn after *Larsen*, 1988]. The different fault traces are overstepping (or *en échelon*) in map view.

can be very low. A tectonically deformed zone (*i.e.* damage zone) flanking the fault core can potentially form a preferential flow path in unconsolidated sediments because the deformation bands developing in the damage zone through particulate flow can have an slightly enhanced permeability [*Bense et al.*, 2003b]. Cataclasis (*i.e.* the breaking and crushing of grains) that strongly reduces pore space and permeability along deformation bands is believed to be the dominant deformation mechanism only at depths larger than 500-1000 m [*e.g. Antonellini and Aydin*, 1994; *Fulljames et al.*, 1997; *Bense et al.*, 2003b].

5.3.2 Fault zone structure

Normal faults that develop in extensional tectonic regimes are segmented. They are generally composed of arrays of overstepping segments [*e.g. Peacock and Sanderson*, 1994; *Walsh et al.*, 1999, 2003]. In the RVRS the overstepping nature of faults is the result of structural inheritance combined with a present day stress field that is oblique to the fault structure [*Houtgast et al.*, 2002]. Fault relay- or transfer zones occur on places where fault displacement is transferred from one fault segment to another. Figure 5.4 shows, schematized, the structure of such a zone.

Whereas a fault zone process such as clay smearing reduces the effective fault zone permeability, in contrast, relay structures can be the locus of hydraulic contact in an otherwise compartmentalized reservoir [*Larsen*, 1988]. *Peacock and Sanderson* [1994] argue that fault relay zones in their first stages of evolution will be the places where foot wall and hanging wall will be connected while in later stages, when the different fault segments start to interact, secondary fractures will develop and

progressively connect both segments. In the North Sea Basin [*Morley et al.*, 1990], relay ramps in this later stage of their evolution are a trap for hydrocarbons.

Faults can also be vertically segmented [*e.g. Childs et al.*, 1996], which is observed in both outcrop [*Burhannudinnur and Morley*, 1997] and on seismic sections [*Morley and Burhannudinnur*, 1997]. As a result of vertical segmentation it can be expected that preferential flow paths exist in the fault zone that would otherwise be absent.

5.4 Groundwater flow patterns in the Lower Rhine Embayment

On a regional scale, groundwater flow in the study area is from south to north, from the Schiefergebirge towards the North Sea. At a local scale groundwater flow is driven by smaller scale topographic features and directed towards the Rhine and Maas Rivers. As a result of the regional-scale lowering of the groundwater table in the lignite mining area that started at regional scale in the mid 1950s, the impact of the faults on groundwater flow in the area has become increasingly important [*Spelter and Schneider*, 1989; *Peukert and Helmbold*, 2000]. The impact of faults on groundwater flow patterns in the area is assessed by inspection of the hydraulic head maps. These maps are based upon a dense network of groundwater observation wells (typically one for each km^2)

The hydraulic head distribution in one of the deeper aquifers in the lignite mining area and the location of the largest open pit lignite mines (*e.g.* "Hambach" and "Garzweiler") are shown in map-view in Figure 5.5. This map also shows the location of the most important groundwater extraction points at the depth of these aquifers. In the more shallow aquifers, groundwater extraction is concentrated at the location of the open pit mines while in the deeper aquifers, groundwater extraction is concentrated at centralized points in each tectonic block (Figure 5.5). Groundwater lowering in the deeper aquifers causes a regionally extending cone-shaped depression in hydraulic head on the Erft Block and the adjacent tectonic blocks. Regional scale groundwater lowering in the area started in the mid $1950\ \mathrm{s}$. Exploitation of lignite in the area is ongoing with abandoned mines closing and new ones opening. As a result, in combination with the complex regional scale water-management measures, the groundwater flow system is strongly transient. Complex numerical models are used to evaluate the effect on groundwater flow of future extension and deepening of the largest mines (*e.g.* "Hambach" and "Garzweiler") in the area [*Peukert and Helmbold*, 2000].

Figure 5.5 shows that the flow system in the LRE is strongly compartmental-

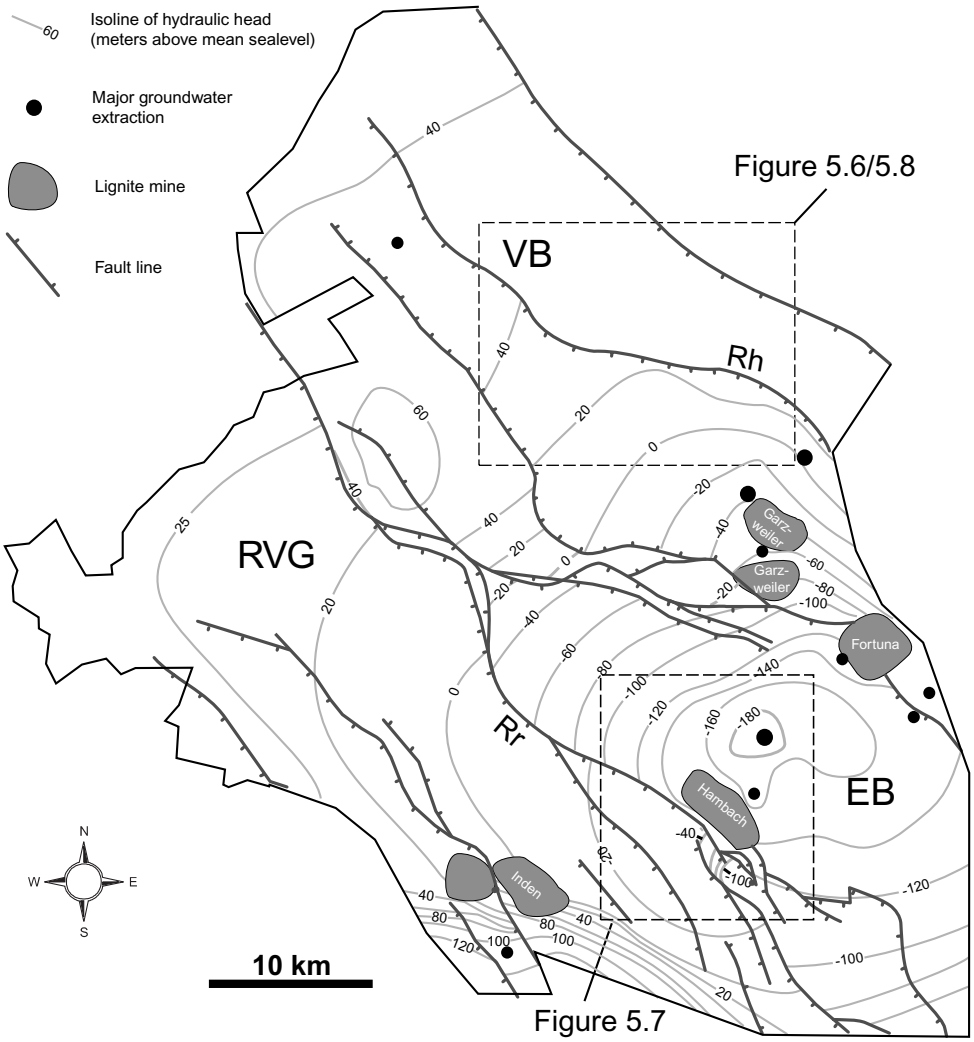

Figure 5.5: Map (extent indicated in Figure 5.1) of the hydraulic head distribution (contours in m) in one of the deeper aquifers (5) in the Lower Rhine Embayment (situation as of October 1987). Groundwater levels are lowered artificially to make open pit mining possible. The distribution of hydraulic heads clearly demonstrates the strong impact of faults on the groundwater flow situation in the area. This map is based upon a dense network of groundwater observation wells that is operated to monitor the regional effects of groundwater lowering in the area (Rh = Rheindahlen Fault, Rr = Rurrand Fault, RVG = Roer Valley Graben, EB = Erft Block, VB = Venlo block)

ized. Most faults are separating areas with strongly contrasting mean hydraulic head values and in many places groundwater flow (more or less perpendicular to the contours of hydraulic head) is parallel to faults. Consequently, faults are zones of very high hydraulic gradients and must have a strongly reduced permeability. Because groundwater flux increases towards the center of the groundwater extraction, the hydraulic head difference over the fault (Δh_f) increases in the direction of the area where the main well fields are situated. For example, Δh_f along the Rurrand Fault at the southern margin of the Erft Block increases from $\sim 20\ \mathrm{m}$ in the north to almost $120\ \mathrm{m}$ close to "Hambach" open pit mine. However, high hydraulic gradients can also be caused by other aquifer properties, for example south of the "Inden"-mine high hydraulic gradients occur as result of the thinning of the aquifer towards the edge of the Schiefergebirge.

5.4.1 Groundwater flow around the Rheindahlen Fault

In the Venlo Block mining activities are concentrated at the "Garzweiler" open pit mines. Figure 5.6 shows the hydraulic head map for aquifer 5 around the Rheindahlen Fault in the Venlo Block and, additionally, the hydraulic head distribution in more shallow aquifers (6B & 6D). Groundwater flow in the Venlo Block is mainly towards the mining area in the south and the lower lying areas in the direction of the Rhine river in the north. In the hydraulic head pattern in the shallow aquifer (6 D) the impact of topography is recognized; however, at larger depth (aquifers 6 B & 5) the impact of the topography-driven flow system is dampened (Figure 5.6). Δh_f varies laterally along the Rheindahlen Fault: it increases towards the south in the direction of the "Garzweiler" open pit mine. Another important observation is that with increasing depth the hydraulic head difference over the Rheindahlen Fault increases. This may be the result of vertical and lateral variations in fault hydraulic properties that are coupled to variations in clay content of the fault zone which, in turn, are linked to lateral and vertical variation in fault throw. Summarizing, groundwater flow patterns in this area, and hence Δh_f, are determined by topography-driven flow as well as fault permeability and induced groundwater flow as a result of de-watering measures around the "Garzweiler" open pit mine.

5.4.2 Fault relay in the Rurrand Fault

Figure 5.5 shows that the cone of depression in the Erft Block is strongly hampered by the Rurrand Fault to propagate into the Roer Valley Graben. However, the sealing behavior of the Rurrand Faults is interrupted at a relay zone close to the "Hambach"-mine. Figure 5.7 shows this location in detail. A dense network of

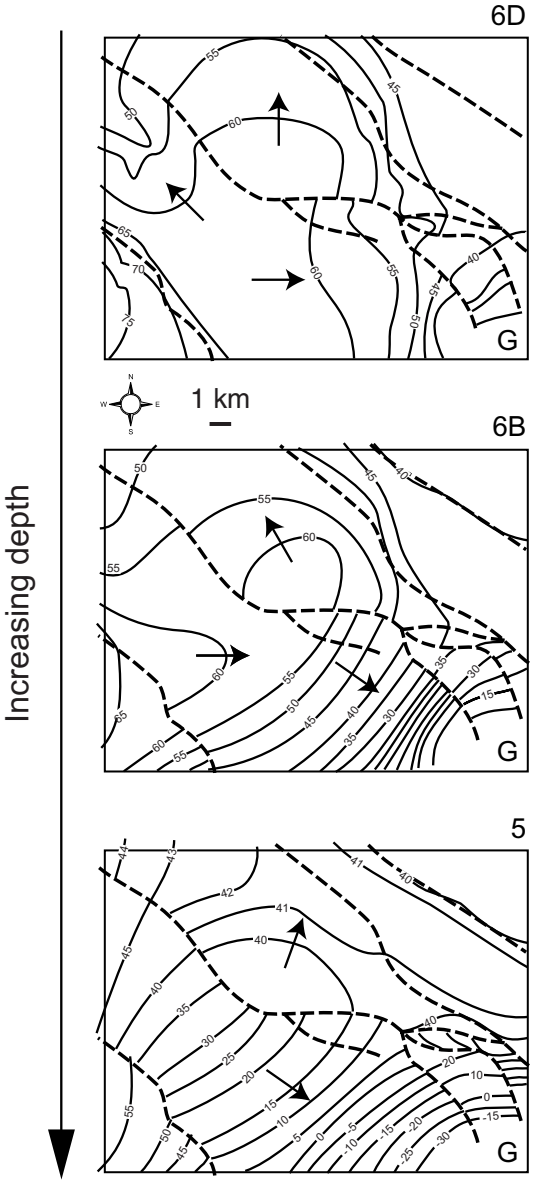

Figure 5.6: Hydraulic head distribution for aquifers at different depths around the Rheindahlen Fault (situation as of November 1996; the extent of this map is shown in Figure 5.5). Aquifer IDs refer to Figure 5.2, "G" indicates the location of the "Garzweiler" mine. The dashed lines indicate fault lines, the arrows indicate roughly the direction of groundwater flow. Contours are in mabove mean sea-level. The maps show how the impact of the topography-driven flow system towards the Rhine and Maas Rivers is decreasing with increasing depth, while the impact of the groundwater lowering measures around the "Garzweiler" mine increases.

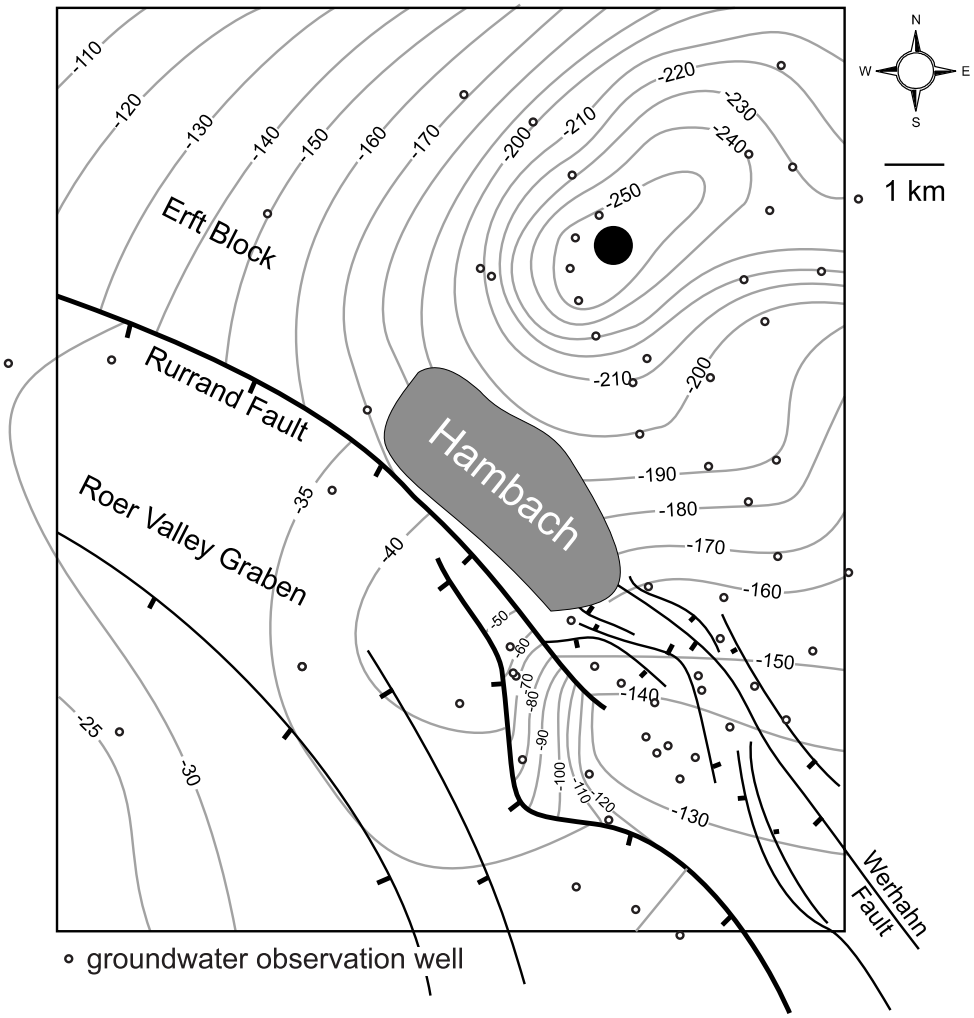

Figure 5.7: Relay structure in the Rurrand Fault close to the "Hambach" open pit mine (situation as of January 1996; the extent of this map is shown in Figure 5.5).

observation wells monitors how groundwater flow is forced through the relay zone that is only around one km wide. The direction of flow is strongly deflected into the relay zone. As a result of the small width of the relay zone, groundwater flux must be high resulting in a steep hydraulic gradient within the relay zone. Moreover, in the Roer Valley Graben the cone-shaped depression is centered around the relay zone. From these observations it is concluded that although the areal extent of the relay structure in the Rurrand Fault is quite limited, its hydraulic properties and structure are major controlling factors on the amount of groundwater lowering in the Roer Valley Graben as a result of the de-watering measures around "Hambach" open pit mine.

5.5 Analysis

In the following sections two scenarios, sealing faults and leaky relay zones, are quantitatively analyzed. First, the Shale Gouge Ratio method is applied in order to estimate the variation of clay content along the Rheindahlen Fault. The calculated SGR-values are compared to observed hydraulic head differences over the fault. Second, to explore the dynamics of the flow system around relay zones as a function of fault properties and the structure of the relay zone groundwater flow simulations were carried out.

5.5.1 Clay smear modeling along the Rheindahlen Fault

Figure 5.8 shows a map of the area around the Rheindahlen Fault that indicates the locations of the groundwater observation wells and cross-sections that are used in the following analysis. Figure 5.2 summarizes the hydrogeological buildup around the Rheindahlen Fault. Bore-hole logs, available for each groundwater observation well, are used to estimate the volumetric clay-content (V_{clay}) of the lithologies flanking the Rheindahlen Fault because no samples of the sediments were available for laboratory analysis. These data are combined with estimates of the amount of throw (θ) which are based upon interpreted geological cross-sections (Figure 5.11). Throw and clay content are combined to calculate the distribution of the Shale Gouge Ratio at the locations where cross-section 413, 433, 453 and 477 intersect the Rheindahlen Fault (Figure 5.11).

Application of the Shale Gouge Ratio algorithm

The Shale Gouge Ratio (SGR) serves as an estimate for the proportion of clay in the fault gouge [*e.g. Freeman et al.*, 1998; *Yielding et al.*, 1997; *Yielding*, 2002, Figure 5.9].

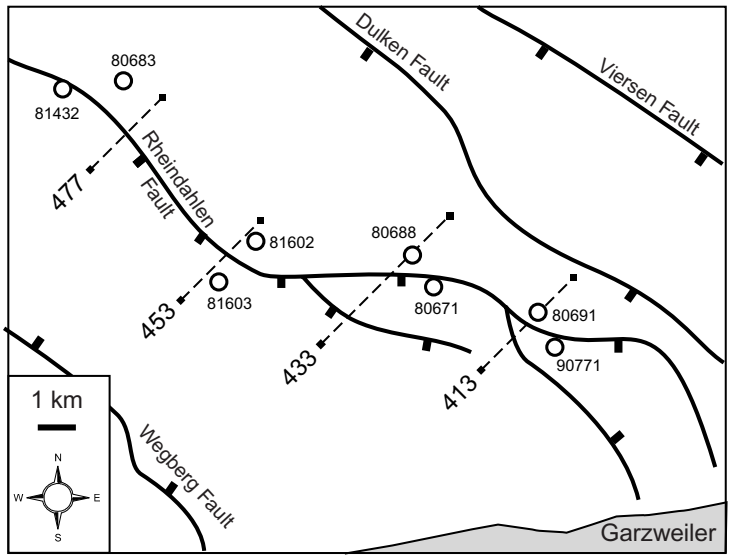

Figure 5.8: Map (extent indicated in Figure 5.5) showing the locations of the cross-sections 413, 433, 453 and 477 (dashed lines) and bore-holes (open circles) used for the modeling of clay smear along the Rheindahlen Fault.

The SGR-algorithm requires a stratigraphical column that is discretized in intervals (Δz) each with an assigned value for V_{clay}. For a given distribution of throw (θ) with depth the SGR along the fault is then calculated via:

$$SGR = \frac{\Sigma(V_{clay} \cdot \Delta z)}{\theta} \cdot 100\% \tag{5.1}$$

The data that are used in this study are non-standard compared to other studies where the SGR-methodology has been applied. In such studies, typically, seismic data are used to map the fault structure in combination with γ-ray logs from deep wells to estimate the shale content of the lithology as a function of depth [*e.g. Harris et al.*, 2002].

In this study, cross-sections 413, 433, 453 and 477 (Figure 5.11) are used as if they were seismic images and are believed to provide a reliable model of fault structure. Throw is determined for key-horizons. Subsequently, fault throw is linearly interpolated between these key horizons and extrapolated above and below the upper- and lowermost key horizons.

The bore-hole logs yield a detailed, verbose description of the local lithological stratigraphy (for an example see Figure 5.10). From these logs average values of

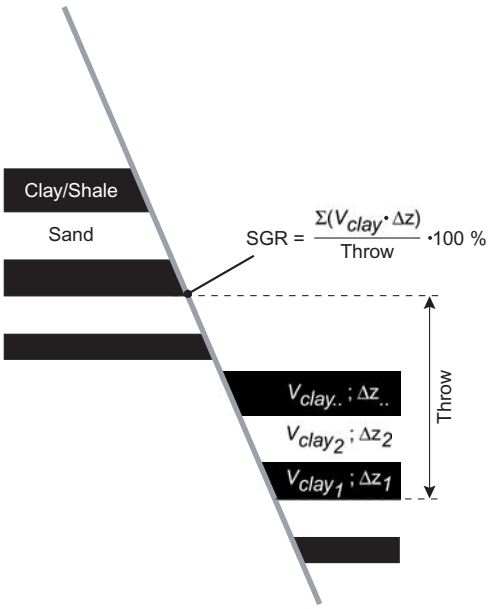

Figure 5.9: The concept of the calculation of the Shale Gouge Ratio (SGR) along a fault plane that is flanked by stratigraphy that consists of an alternation of sands and clay with varying values of V_{clay}.

V_{clay} were estimated in intervals (Δz) of 5 m. As the descriptions in the logs are concise and systematic, these could be converted in a consistent way to an estimate for V_{clay}. Therefore, each lithological description in the log was assigned a specific value of V_{clay}. For example, *"clayey sand"* represents a V_{clay} value of 0.3 (30 %) while *"clay"* is assumed to consist of 80 % of clay. Lignite has comparable hydraulic properties as clay. Also, it is known from field exposures in the "Garzweiler"-open pit mine and from other studies [*e.g. Lindsay et al.*, 1993] that at shallow depth lignite can be smeared along the fault plane. For that reason *Sperrevik et al.* [2002] suggests that the effect of lignite layers should be taken into account in the calculation of SGR. In order to simulate the expected smearing behavior of lignite this lithology has been assigned an arbitrary V_{shale} value of 0.3 in the present analysis. In case the clay-content and the thickness of the units vary considerably over the fault, the V_{clay} estimates and thickness of the unit on both sides of the fault have been averaged.

Figure 5.12 shows the inferred throw- and calculated SGR variations as function of depth together with the distribution of V_{clay} in the flanking lithology at each location and on each section.

The displacement pattern along the Rheindahlen Fault compares well to those found generally in syn-sedimentary fault systems [*e.g. Walsh and Watterson*, 1989;

Gesamtteufe in m bis	Schichtmächtigkeit in m	Bezeichnung der Gebirgsschichten nach Bohrproben und geophysikalischer Messung	Geologisches Profil	Horizontbezeichnung nach SCHNEIDER/THIELE	Teufe in m
0.5	0.5	Mutterboden			
4.4	3.9	Lößlehm			
13.4	9.0	Kies, mit Sandlagen		16	10
14.3	0.9	Schluff, an der Basis sandig			
20.0	5.7	Sand, mit Kieslagen, von 15.1 m bis 16.8 m teilweise mit schluffigen Lagen		8	20
20.7	0.7	Mittelsand–Grobsand, hellgrau, gelblich, feinkiesig – mittelkiesig			
21.2	0.5	Mittelsand–Mittelkies, hellgrau, gelblich, schwach grobkiesig		6E	30
21.7	0.5	Mittelsand, hellgrau, gelblich			
22.0	0.3	Mittelsand–Mittelkies, grau, gelblich			
22.3	0.3	Mittelsand, hellgelb–dunkelgelb, mit schluffigen Lagen im mm–Bereich			
35.3	13.0	K o h l e, von 26.7 m bis 28.7 m teilweise holzig, ab 34.9 m teilweise sandig			40
35.7	0.4	Mittelsand, graubraun–braun, am Top weißlich			
43.0	7.3	Sand			50
45.3	2.3	Mittelsand, grau, bis 44.0 m bräunlich, von 44.0 m bis 45.0 m teilweise schwach grobsandig			
45.5	0.2	Ton–Schluff, grau, bräunlich, mit Pflanzenresten, stellenweise mit Feinsandlagen im mm–Bereich			60
47.0	1.5	Mittelsand, grau, mit wechselnden Grobsand–Anteilen, ab 46.0 m teilweise schwach feinkiesig, an der Basis mit Schlufflagen im mm–Bereich			
53.0	6.0	Mittelsand, grau, bis 47.4 m bräunlich, bei 52.1 m und ab 52.6 m mit Tonlagen im cm–Bereich		6D	70
53.3	0.3	Schluff, graubraun, tonig, feinsandig, mit Pflanzenresten, stellenweise mit Feinsandlagen im mm–Bereich			
54.0	0.7	Mittelsand, grau, am Top grobsandig und am Top stark glimmerhaltig			80
54.2	0.2	Schluff, graubraun, tonig, mit Pflanzenresten, stellenweise mit Feinsandlagen im mm–Bereich			
77.6	23.4	Mittelsand, grau, feinsandig, schwach glimmerhaltig			90
78.9	1.3	Feinsand–Mittelsand, grau, teilweise schluffig			
83.8	4.9	Feinsand–Mittelsand, grau, schluffig, glimmerhaltig, mit Schlufflagen und mit Tonlagen bis 1 cm mächtig			
87.8	4.0	Schluff–Feinsand, grau, teilweise tonig, glimmerhaltig, mit Tonlagen im mm–Bereich			100
91.8	4.0	Feinsand–Mittelsand, grau, stellenweise schluffig, ab 89.4 m mit Pflanzenresten, bis 89.8 m abnehmend mit Schlufflagen		6C	
95.8	4.0	Feinsand–Mittelsand, grau, von 92.6 m bis 93.8 m hellgräulich, bis 92.2 m teilweise schwach schluffig, ab 93.0 m teilweise mit humosen Lagen, von 93.0 m bis 93.3 m mit Feuersteingeröllen bis 3 cm Durchmesser			110
102.6	6.8	K o h l e, teilweise holzig, ab 102.1 m schwach tonig, ab 98.9 m stellenweise mit Vertikalklüftung		6B	120

Figure 5.10: Example of the borehole logs that were used to estimate the V_{clay} values of the lithologies flanking the Rheindahlen Fault.

Childs et al., 2003]. Fault throw increases northward from line 413 ($\overline{\theta} = 77\,\mathrm{m}$). Mean fault throw is maximal along line 453 ($\overline{\theta} = 139\,\mathrm{m}$) and fault throw decreases towards the north to line 477 where $\overline{\theta}$ is $84\,\mathrm{m}$. Figure 5.1 shows that further towards the north the Rheindahlen Fault is not continued. Figure 5.12 shows how throw is increasing with depth at each section. For example, while in section 413 vertical throw at the base of unit 6A is $90\,\mathrm{m}$, at the top of 6C vertical throw is $80\,\mathrm{m}$.

The inferred V_{clay} logs show that the lithology cut by the Rheindahlen Fault is dominated by clean sand with low clay content. The maximum calculated SGR values ($\sim$24 %) occur along section 453 where also on the average θ and V_{clay} are largest. The average SGR values for section 413 , 433 , 453 and 477 are 15.6 %, 17.3 %, 17.0 % and 11.0 % respectively. Figure 5.12 shows that at section 477 and 413 the vertical variation in SGR-values is greater than at the other two sections. The larger throw along 453 and 433 results in a smoothing of the inferred clay-content of the fault zone relative to the other two sections with a lesser throw.

In order to test whether the calculated variation of SGR is related to observed hydrological data around the Rheindahlen Fault, hydraulic head observations are used from the same wells as the lithological logs were available (Figure 5.8). A complex pattern of juxtaposition of the different aquifers exists at the fault. For example, along the fault there can be a trajectory where aquifer 5 is juxtaposed to aquifer 6D while along another trajectory the same aquifer is in hydraulic contact with aquifer 6B. The hydraulic head difference (Δh_f) for each occurring juxtaposition is calculated based upon the piezometric observations within each aquifer where it is assumed that the vertical hydraulic gradient within each aquifer is neglectible (*i.e.* no vertical flow occurs within the aquifer). Finally, the SGR values for each depth interval along which a juxtaposition occurs are then plotted against Δh_f (Figure 5.13). Hydraulic head data from 1990 and 1997 have been used for comparison.

As discussed above, apart from fault permeability additional factors will determine the hydraulic head contrast over the fault. However, it appears that the hydraulic head difference over the Rheindahlen Fault (Δh_f) and the calculated fault properties (SGR) are still strongly related (Figure 5.13) suggesting that fault permeability is the dominant factor controlling the head difference over the fault. However, the relation between Δh_f and SGR is non-unique and, therefore, cannot be directly coupled to fault permeability. With increasing exploitation of the lignite mines over time, groundwater levels are further lowered and groundwater fluxes increase. A small increase in Δh_f between 1990 and 1997 is seen for most analyzed wells (Figure 5.13), but *SGR* variations have a dominant effect. Similar trends are

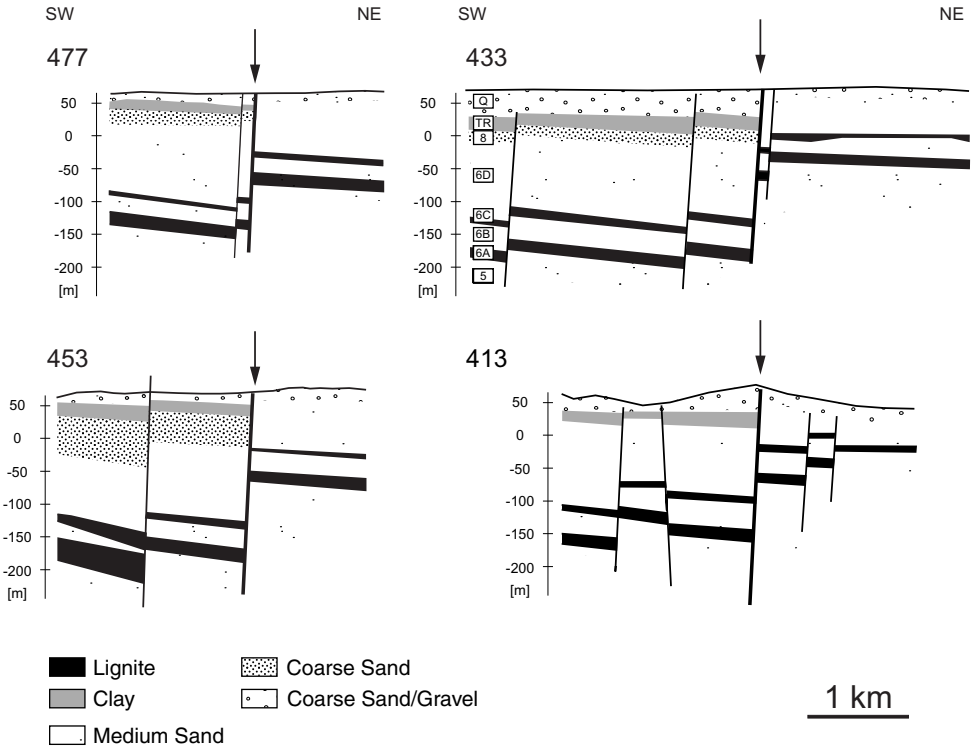

Figure 5.11: Four cross-sections (schematized) over the Rheindahlen Fault showing the variation of vertical throw along the fault and the resulting varying geometries of aquitards and aquifers at the fault. The Rheindahlen Fault is indicated by an arrow.

reported by *Harris et al.* [2002] and *Yielding et al.* [1999] which both describe data from deep hydrocarbon reservoirs.

Fault permeability

In order to be able to incorporate a given fault zone into a groundwater flow model, fault zone hydraulic conductivity (K_f) and fault zone width (w) are required. It is tested whether the SGR-approach leads to reasonable estimates of fault zone hydraulic properties by comparing the results from the SGR-approach to fault

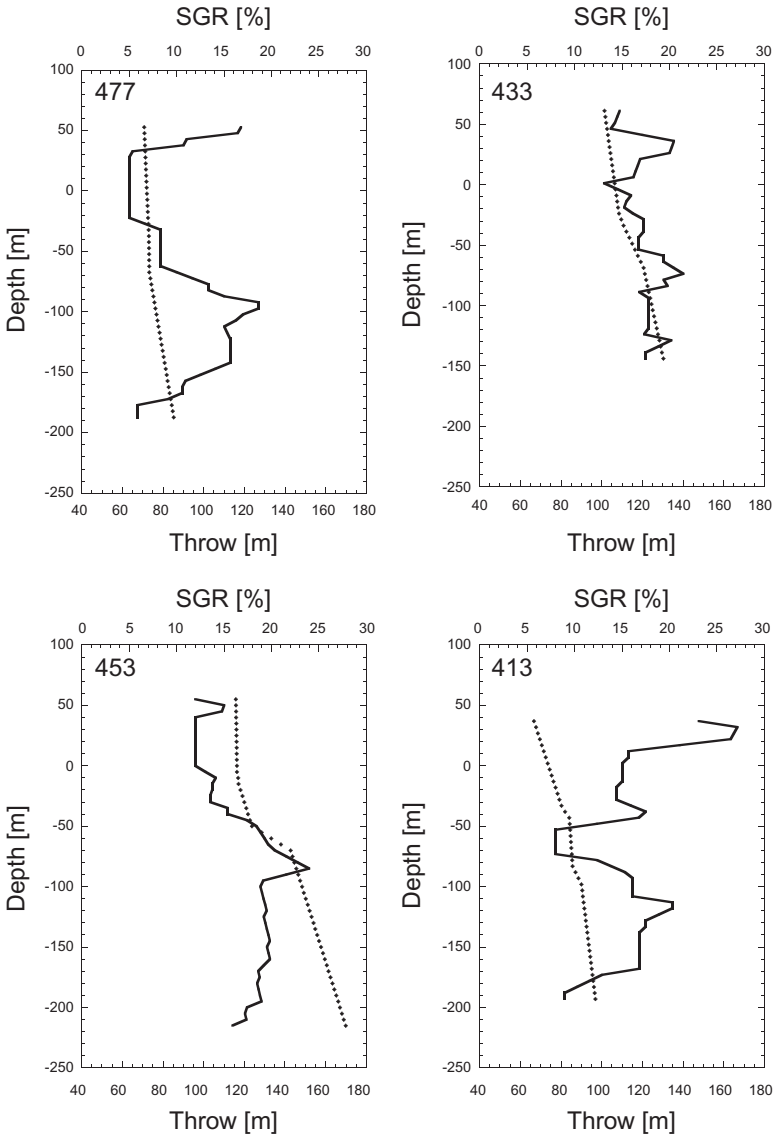

Figure 5.12: The variation of fault throw (dashed line) and SGR (solid line) along the Rheindahlen Fault at the location of sections 413, 433, 453 and 477.

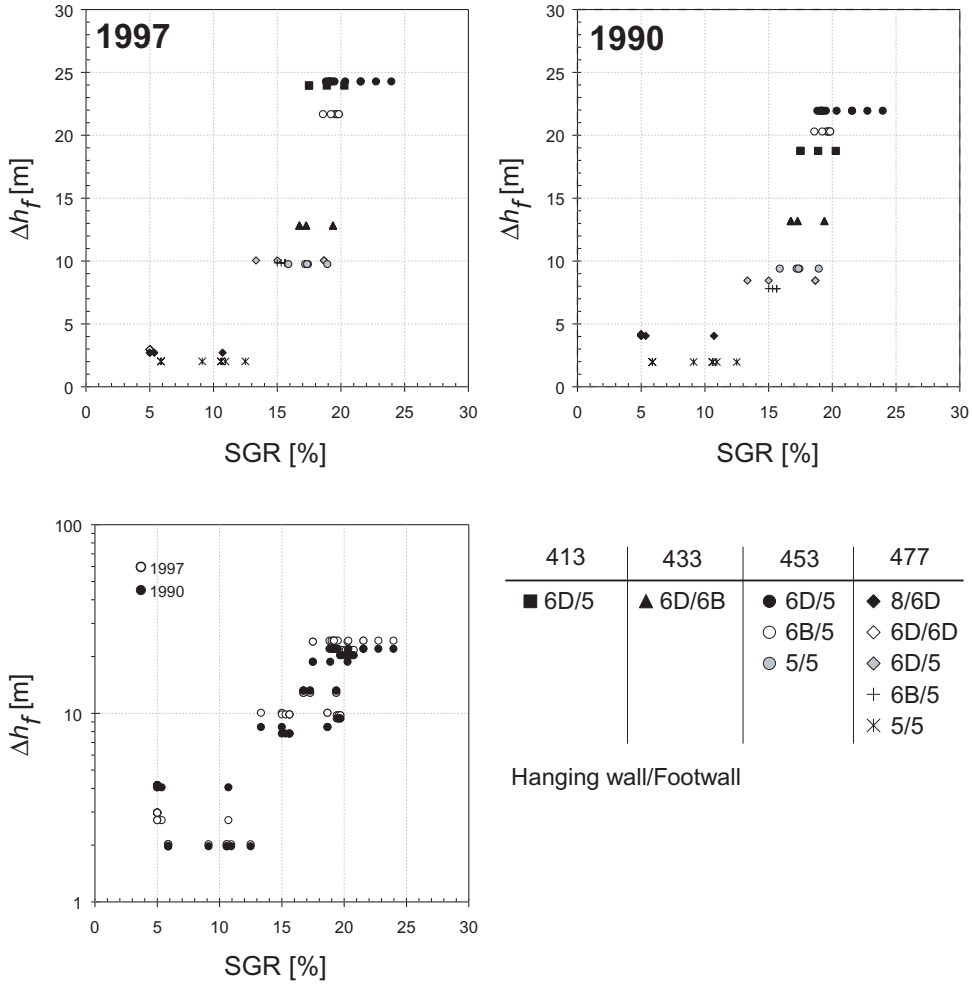

Figure 5.13: Calculated SGR values vs. Δh_f between different hydrogeologic units (see Figure 5.2) over the Rheindahlen Fault along line 413, 433, 453 and 477.

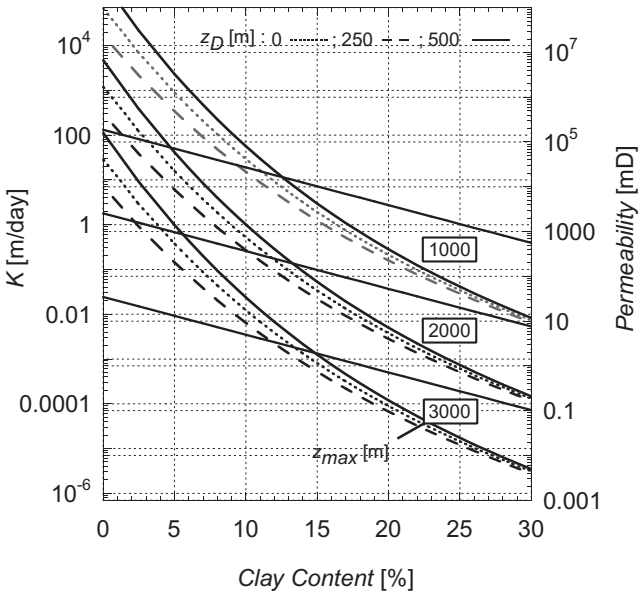

Figure 5.14: The relation between the bulk hydraulic conductivity (K) of the faulted material (curved lines) and undeformed host rock (straight lines), and its clay content, for different scenarios of the depth at the time of deformation (z_D) and maximum burial depth (z_{max}). This plot is based on *Sperrevik et al.* [2002].

zone hydraulic properties that have been inferred independently from numerical groundwater flow models. First it is shown how K_f and w can be estimated from SGR and fault throw respectively using empirical relations.

Empirical data show that the permeability of a given fault gouge is strongly related to its clay content [*e.g. Sperrevik et al.*, 2002; *Yielding*, 2002]. As shown in Figure 5.12, the inferred SGR along the fault plane, an estimate of the clay content of the fault, varies considerably with depth. It is expected that the permeability will vary in a similar way. Several empirical relations have been proposed to calculate fault zone permeability from estimated clay contents of the fault rock [*Manzocchi et al.*, 1999; *Sperrevik et al.*, 2002; *Badleys Earth Sciences*]. Among these, only the relation proposed by *Sperrevik et al.* [2002] seems valid for shallow fault zones (*e.g.* < 250 m depth) because it takes into account both the depth at the time of deformation (z_D) as well as the maximum burial depth (z_{max}). The depth at time of deformation is of considerable importance because the type of deformation mechanism is controlled by the burial depth. Disaggregation zones will form at relatively

shallow depth (< 500 m depth) via particulate flow while at larger depths deformation bands will form through cataclasis [*e.g. Fulljames et al.*, 1997; *Sperrevik et al.*, 2002]. Disaggregation zones have a somewhat higher permeability with respect to the unfaulted host material [*e.g. Bense et al.*, 2003b], while cataclastic deformation bands have very low permeabilities [*e.g. Antonellini and Aydin*, 1994].

Figure 5.14 shows the proposed relation (from *Sperrevik et al.* [2002]) between the estimated clay content and the bulk hydraulic conductivity (K) for faulted and undeformed rocks. According to these curves, with decreasing clay content of a given fault the predictability of its hydraulic properties decreases because the values of z_D and z_{max} are more critical. These curves also predict an increase in permeability (via particulate flow) of clean sand when deformed at shallow depth as compared to the undeformed host material. However, when the clay-content is larger than about 15 % permeability is expected to be lower in the deformation band (via clay smearing) compared to the host material.

Additionally, empirical relations are available to estimate w from fault throw [*e.g. Knott et al.*, 1996; *Manzocchi et al.*, 1999; *Sperrevik et al.*, 2002]. Based upon these, a fault with a throw of, for example, ~ 100 m is estimated to have a width of 1 to 5 m (equation 3 in *Sperrevik et al.* [2002]).

In groundwater flow studies the hydraulic properties of a given fault zone can be quantified using the fault resistance (r) which is defined as [Chapter 2 *Bense et al.*, 2003a]:

$$r = \frac{w}{K_f} \tag{5.2}$$

Wallbraun [1992] and *Spelter and Schneider* [1989] show that, based upon groundwater flow modeling, many faults in the lignite mining area have hydraulic resistances ranging from 100 to 750 days.

The results from groundwater flow studies are compared to those from the SGR-approach, in the following way. The hydraulic conductivity of the aquifers around the Rheindahlen Fault is 10-25 m/day *Wallbraun* [1992]. These aquifers have a $V_{clay} \simeq 10$ %. This sediment is dragged to the fault together with flanking clay-layers ($V_{clay} \simeq 70$ %) resulting in values of fault clay content (estimated via the SGR-algorithm; Figure 5.12) varying between ~ 10 % and 25 %. Based upon the curves proposed by *Sperrevik et al.* [2002] (Figure 5.14) and assuming that the burial depth of these sediments never exceeded 1000 m, the hydraulic conductivity of the fault gouge along the Rheindahlen Fault ranges between 10 and 0.03 m/day. A fault is expected to have a continuous clay smear at $SGR \geq 20$ % [*Sperrevik et al.*, 2000; *Yielding*, 2002]. Consequently, application of equation 5.5.1 shows that a sealing fault ($SGR = 25\%$, $K_f = 0.03$ m/day, $w = 5$ m) will have a resistance of around

$\sim$170 days. This is in reasonable agreement with the values for fault resistance that result from groundwater flow modeling of the area. Trajectories along the fault with SGR-values $\leq 10\ \%$ are expected to have fault properties not very different than the surrounding host material at these shallow depths.

5.5.2 Fluid flow simulation around a fault relay structure

Numerical simulations, in 2D, have been setup in order to study the general characteristics of groundwater flow around a relay structure.

The relay zone in the Rurrand Fault appears to be open for groundwater flow from the Roer Valley Graben to the Erft Block (Figure 5.7). However, the fault segments north and south of the relay zone, are zones of low permeability. In the following modeling study, it was tested how the steady-state groundwater flow field around the relay structure changes with different values for the permeability of the segmented Rurrand Fault in case the relay zone is open for groundwater flow. The results are compared with observed patterns around the "Hambach" open pit mine. First, the model schematization and setup are discussed in the following section.

Modeling setup

A generic finite element package FlexPDE [*PDE Solutions*, 2003] was used to solve the governing groundwater flow equation. Groundwater flow can be described by Darcy's Law as:

$$\vec{q} = -KD\nabla h \tag{5.3}$$

where KD is hydraulic transmissivity of the aquifer (*i.e.* the product of a vertically averaged hydraulic conductivity and aquifer thickness). For steady-state conditions:

$$\nabla \cdot \vec{q} = 0 \tag{5.4}$$

which is the equation that is solved in the numerical simulations presented below.

The model domain has a size of 40×40 km. The left-hand side of the model domain conceptually represents the Roer Valley Graben ($KD = 1000\ \mathrm{m}^2$ / day) that is separated by the segmented Rurrand Fault from the Erft Block ($KD = 500\ \mathrm{m}^2$ / day) on the right-hand side. Both blocks are assigned contrasting values of KD because, as a result of fault throw, aquifer thickness is larger on the downthrown side than on the higher tectonic block. The relay zone is represented as a one km wide zone over which the aquifer linearly thickens from the higher block ($D_f = 100$ m) towards the downthrown block ($D_f = 200$ m). The fault segments are schematized

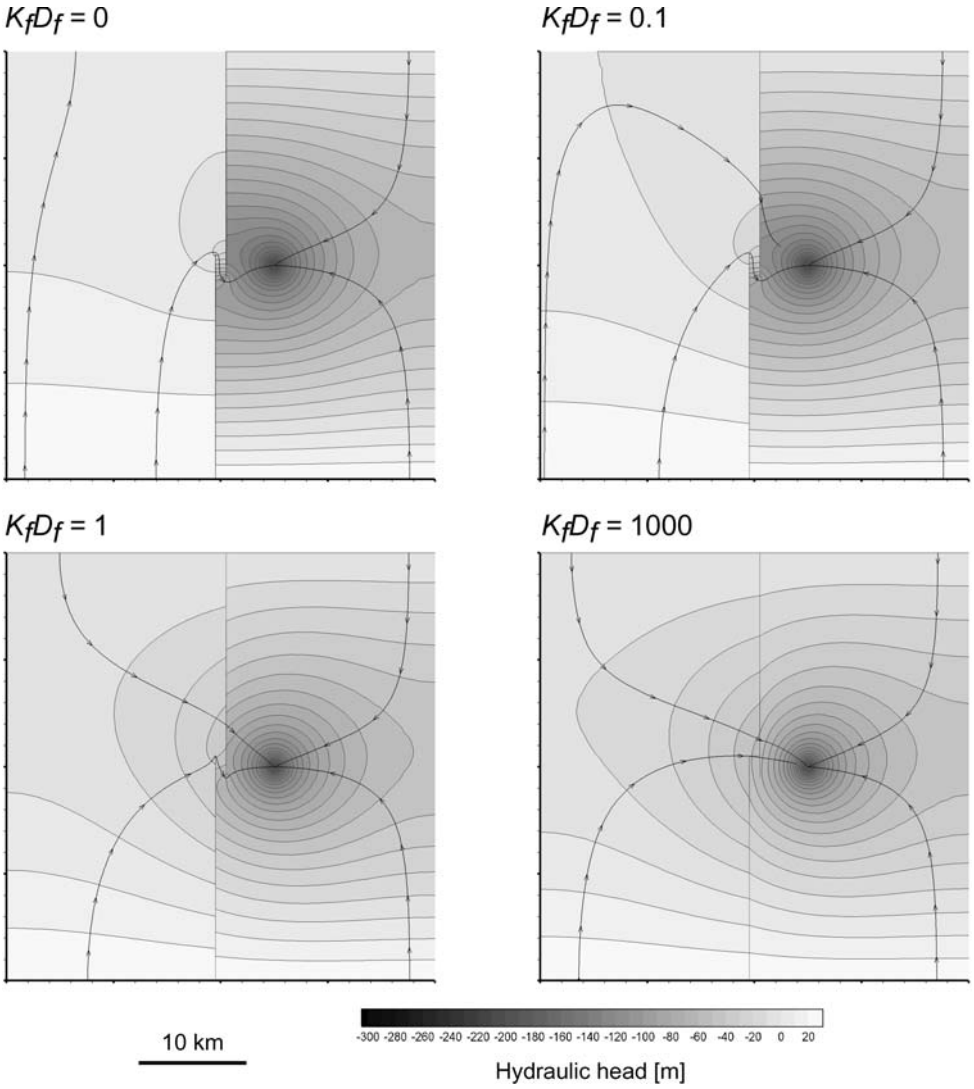

Figure 5.15: Results of numerical simulations of the hydraulic head distribution around an area of major groundwater lowering influenced by a segmented fault zone. As fault zone transmissivity [m^2 / day] is increasing the impact of the fault relay zone is decreasing. Contour interval of hydraulic head is 10 m.

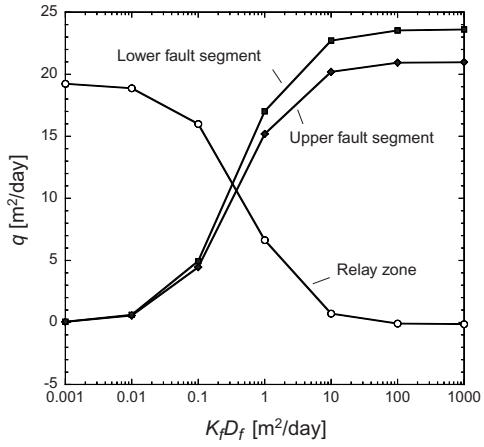

Figure 5.16: Plot of the amount of groundwater flow per unit length over the upper- and lower fault segment, and through the relay zone as a function of $K_f D_f$.

as two $10\ \mathrm{m}$ wide zones with a transmissivity $K_f D_f$, which results in an "open" relay zone when the segments are not linked. It is assumed for simplicity that $K_f D_f$ is constant along the whole strike of the fault.

An area with a fixed low hydraulic head ($-300\ \mathrm{m}$) is implemented on the Erft Block close to the fault relay zone to mimic the area of largest groundwater lowering in accordance with the actual situation (Figure 5.7). The left- and right-hand side of the model domain are no-flow boundaries while at the upper and lower boundaries fixed heads have been assigned in accordance with the observed regional head so that, potentially, groundwater flow is from south to north.

Results

Model runs have been done for fault transmissivities increasing with steps of one order of magnitude starting from the situation that the fault segments are closed for fluid flow ($K_f D_f = 0\ \mathrm{m}^2$ / day) to the situation that the fault segments have the same transmissivity as the flanking aquifer ($K_f D_f = 1000\ \mathrm{m}^2$ / day). The total flux of groundwater flow, for each value of $K_f D_f$, is calculated over the upper fault segment, the fault relay zone and the lower fault segment.

Figure 5.15 shows that when $K_f D_f$ is stepwise increased, groundwater lowering within the Erft Block has an increasingly important impact on the groundwater flow regime in the Roer Valley Graben. Additionally, Figure 5.16 shows that, as can be expected, the flux through the relay is maximal when $K_f D_f$ is small (*i.e.* the fault segments are strong barriers to fluid flow). When $K_f D_f$ is increased, groundwater flow over the upper and lower fault segments also increase while groundwater

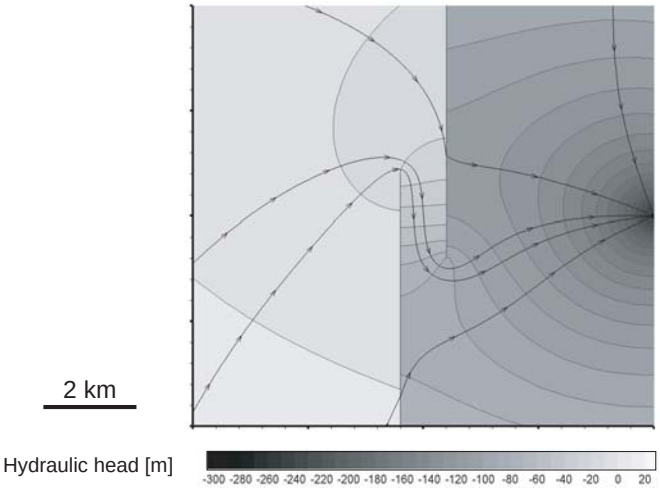

Figure 5.17: Detail of the model presented in Figure 5.15 (for $K_f D_f = 0.1\ \mathrm{m}^2$ / day) showing the groundwater flow pattern around the fault relay in great detail. Contour interval is $10\ \mathrm{m}$. The simulated groundwater flow pattern is very similar to that observed around the "Hambach" open pit mine (Figure 5.7).

flow through the relay decreases. High hydraulic gradients are found in this zone while these gradients are absent when the relay zone is closed.

Comparison of Figure 5.17, which shows the simulated groundwater flow pattern just around the relay zone ($K_f D_f = 0.1\ \mathrm{m}^2$ / day), with Figure 5.7 shows the strong similarity of the simulated groundwater flow pattern with the situation that is found around the "Hambach" open-pit mine. The aquifer thickness at the fault is assumed to be $\sim 50\ \mathrm{m}$, *i.e.* the height over which the two tectonic blocks are juxtaposed. This results in a hydraulic resistance of $5000\ \mathrm{days}$ and a value of K_f of $0.002\ \mathrm{m}$ / day for the Rurrand fault at this location. This value is much lower than that obtained for the Rheindahlen Fault ($\sim 170\ \mathrm{days}$). This might be explained as follows. In contrast with the Rheindahlen Fault the Rurrand Fault is a regionally extending fault (see Figure 5.1), the Rurand Fault has larger throws than the Rheindahlen Fault and cuts through different lithologies. These contrasting characteristics are likely to explain the difference in inferred hydraulic properties. However, this was not extensively tested here.

While steady-state groundwater flow is simulated here, the actual groundwa-

ter flow conditions around the "Hambach" open-pit mine are likely to be transient because pumping rates around the mine are not constant over time. The models that are presented here aim to reproduce in general the observed patterns and should be regarded as first steps in the simulation of groundwater flow around relay zones in sedimentary basins. In future models non-steady groundwater flow can be simulated using the drawdown rates in the mines and fault structure should be represented in 3D.

5.6 Discussion and conclusions

For a correct estimation of SGR-values along a given fault plane reliable information on the clay content (V_{clay}) of the lithologies flanking the fault is essential. In the current study this was difficult as direct measurements of V_{clay} of the sediments flanking the Rheindahlen Fault were not available. Especially the hydraulic and petro-physical properties of the lignite are largely unknown. The V_{clay} values that are used here are best estimates. However, the resulting estimates of the hydraulic properties of the Rheindahlen Fault seem to be reasonable when compared to those inferred from groundwater flow modeling. The advantage of the method applied in this Chapter is that it can be used to make an assessment of the heterogeneity of the fault zone while the fault resistance following from groundwater flow modeling is a vertically averaged value. The effect of anisotropy is not captured in this approach, however, even faults with expected high values for SGR can act as vertical conduit [*Langguth and Ullrich*, 2000]. This should also be considered in the assessment of the sealing capacity of faults.

Apart from the example presented in this Chapter, relay structures are observed on other locations in the rift system. *Houtgast et al.* [2002] show that the Feldbiss Fault Zone (at the southern boundary of the Roer Valley Graben) at a location close to the German-Dutch national border, consists of several individual segments at shallow depth. For the same fault zone, in an area further towards the northwest, an aerial photograph [*Bense et al.*, 2003a] and geoelectrical soundings [*Vandenberghe*, 1982] show fault segmentation (see Chapter 2; Figure 2.4). At this field site hydrochemical data indicate that in this setting the Feldbiss Fault probably forms a preferential path to fluid flow which might be explained by the open structure of the fault.

It is concluded that the structural setting of a fault zone is of considerable importance to the net impact of the fault to fluid flow patterns, additional to the hydraulic properties of the fault itself (*e.g.* Figure 5.15). A general implication for fluid flow within a sedimentary basin is that although it might be possible to make

a sensible estimate of the permeability of a given fault zone (for example via the SGR-approach), in case this fault is strongly segmented a thorough assessment of this segmentation is needed to be able to assign bulk hydraulic properties to the fault. Fault segmentation can be of crucial impact to regional groundwater flow patterns. One of the first well documented examples of fluid flow patterns around a fault relay structure is presented in this study (Figure 5.7).

The insights and techniques summarized above can be used to improve the way faults are implemented in existing hydrogeological modeling studies of sedimentary basins [*Mailloux et al.*, 1999; *Person et al.*, submitted; *Garven et al.*, 1999; *Verweij*, 2003]. So far, fault properties are mostly very uncertain in this kind of modeling studies.

6

Summary and Conclusions

The objective of the work that is reported in this thesis was stated in Chapter 1 as to describe, analyze and quantify the impact of fault zones on groundwater flow in the Roer Valley Rift System and the adjacent areas in Germany that are part of the Lower Rhine Embayment. In this Chapter the outcomes and conclusions of the work presented in this thesis are summarized after which an outlook for possible further research is presented.

6.1 Overview

As only few studies have until now specifically focused onto the impact of faults on groundwater flow in the Roer Valley Rift System and the Lower Rhine Embayment. The overview of hydrologic phenomena associated with faults that is presented in Chapter 2 is believed to form a substantial extension of the present literature on this subject. Moreover, new measurements of shallow groundwater flow as presented show that faults are likely to be vertical conduits while they impede horizontal groundwater flow at the same location. This is an important outcome, relevant to studies that focus to unravel groundwater flow paths at, for example, sites where contaminated groundwater occurs, or to groundwater supply stations that rely on groundwater extraction from faulted sedimentary aquifers.

This thesis is organized in a way which is from small scale (μm) to regional scale (tens of km) and intends to reveal how small scale processes affect the larger scale system. It begins with the smallest scale on the outcrop (Chapter 3) and proceeds to the regional scale effects as observed in the Lower Rhine Embayment (Chapter 5).

In Chapter 2, a general overview of hydrogeological phenomena connected with fault structures and the Roer Valley Rift System is presented based upon existing data which are complemented with new field data gathered during this study. Subsequently, detailed analyses have been made of the various features and processes associated with deformation structures. In the micro-scale study carried out

in the trenched outcrop over the Geleen Fault (Chapter 3), a recently developed image-analysis technique has been applied to unravel the mechanisms of soft sediment deformation close to the surface. The anisotropic nature of fluid flow around fault zones as documented in Chapter 2 can be understood from the fact that clay, as well as sand and gravel, are present and interact along the fault surface. Further analysis shows that the damage zone around the fault core consists of sealing properties through clay smearing, pore-size reduction as a result of grain rotation and diagenetic precipitates (iron-oxidation), as well as enhanced permeability by particulate flow. The resulting strongly anisotropic and heterogeneous conditions cause preferential flow paths and impediments for groundwater flow to exist next to each other.

The study over the Geleen Fault (Chapter 3) and other outcrop studies carried out in the Roer Valley Rift System show that fault zones in this setting are limited in width (only some tens of cm) [*Lehner and Pilaar*, 1997; *Houtgast et al.*, 2002]. As a result, very detailed measurements are needed to reveal the nature of groundwater flow in and around these faults. The study by *Ernst and De Ridder* [1960] clearly demonstrates that this requires placement of groundwater observation wells with a spacing of some tens of meters down to a depth of $\sim 45\ \mathrm{m}$ to be able to unravel the groundwater flow pattern around a small fault in the Venlo Graben in any detail. Chapter 4 presents an alternative method that allows to map, in great detail, the shallow groundwater flow and geothermal regime around the Peelboundary Fault near the village of Uden. This method exploits the interaction of shallow groundwater flow with the seasonal variation of surface temperature to infer near-surface vertical groundwater flow rates. Another important outcome of this study is that for a correct interpretation of the shallow geothermal regime, it is necessary to consider the effect of recent surface warming. The resulting quasi-3D numerical model of coupled heat transport and groundwater flow of the field site near Uden is the first to incorporate simultaneously the effects of long-term changes in surface temperature and the interaction of shallow groundwater flow with the seasonally fluctuating surface temperature.

While Chapter 3 and 4 focus on micro-scale and field-scale respectively, Chapter 5 discusses the effects of faults on regional-scale groundwater flow patterns in the Lower Rhine Embayment. In order to model the hydraulic properties of the faults in this area, techniques originating in the hydrocarbon industry are applied. Despite the complications resulting from the complex groundwater flow situation in the area, a positive correlation is observed between the Shale Gouge Ratio (*i.e.* an estimate of the clay content of the fault gouge based on litho-stratigraphical

data and fault throw) and the hydraulic head differences between both sides of the Rheindahlen Fault. This study has been facilitated by the occurence of strongly enhanced hydraulic gradients as a result of the huge groundwater extractions around the lignite mines in the area. Another important conclusion of this study is that the occurrence of relay zones in segmented faults can be locations where otherwise low permeable faults are open for groundwater flow. The hydraulic head patterns around such an open relay zone is documented and analyzed using numerical groundwater flow models.

The main conclusions of the research reported in this thesis are shortly stated in view of the specific research questions as formulated on page 6 of this thesis:

1. How is the presence of faults in the subsurface reflected in local hydrological conditions within the Roer Valley Rift System?

2. What are the internal structure and associated hydraulic properties of fault zones in unconsolidated sediments?

3. What is the relevance of fault zones to shallow and local groundwater flow paths?

4. What is the impact of the larger scale structure of fault zones on regional groundwater flow?

In answer to the first research question, it is concluded that faults in the subsurface of the Roer Valley Rift System have a strong impact on local and regional hydrological conditions which is reflected in anomalous groundwater flow patterns and associated development of drainage and vegetation (*e.g.* peat development on high parts in the topography).

The research carried out in the trenched outcrop over the Geleen Fault (Chapter 3) shows that faults should be regarded as heterogeneous features which have a strongly anisotropic permeability structure (research objective 2) caused by mechanical deformation. As a consequence of this anisotropy, vertical groundwater flow can be enhanced along faults. Shallow hydraulic head data show that this indeed the case along the Peel Boundary Fault Zone at shallow depth (Chapter 2; Figure 2.15). This shows the importance of faults to shallow groundwater flow paths (research objective 3) as possible conduits between otherwise separated aquifers.

Concerning the last research question, Chapter 5 discusses the effects of clay smearing and fault relay on regional groundwater flow patterns. Exceptionally detailed hydraulic head data from the Lower Rhine Embayment show that fault relay zones can form the locus of hydraulic contact between otherwise separated

aquifers. The regional impact of clay-smearing to groundwater flow was assessed by calculation of the Shale Gouge Ratio (SGR) along the Rheindahlen Fault. The SGR corresponds to the estimated clay content of the fault. Along the Rheindahlen Fault the variation of the hydraulic head difference that exist over the fault is related to the variation of SGR. The SGR-method seems an attractive method for an a priori estimation of fault hydraulic properties related to clay smearing based upon geological data for implementation in hydrogeological modeling. However, a direct conversion from SGR to fault hydraulic properties remains elusive because important effects like fault segmentation, drag of sand along the fault plane and the resulting development of preferential path ways is not captured using the SGR-methodology.

6.1.1 Practical implications

The finding that vertical groundwater flow can be enhanced close to fault zones has important practical implications. Most water supply systems in the southeastern parts of the Netherlands rely on groundwater extractions from deeper aquifers. Water supply managers in this area generally assume that aquifers beneath confining layers will hardly be affected by infiltrating shallow groundwater that is possibly contaminated with, for example, agricultural nutrients or pesticides. However, fault zones may be the loci where protecting clay layers can be discontinuous and shallow groundwater can infiltrate, and might contaminate the deeper aquifer. Indications that deeper aquifers are infiltrated with shallow groundwater at the location of faults in the area of the water supply of the city of Tilburg (for location see Figure 2.1) are found in *Van Zanten* [1996]. Also, studies by *Broers and Buijs* [1997] and *Minnema et al.* [2001] suggest that vertical transport of contaminated groundwater occurs along faults in the Roer Valley Graben and on the Peel Block.

6.2 Future directions

The different studies presented in this thesis provide a basis for future research. In the following, an overview is provided of possible directions this research might take and which improvements are recommended for the methodologies that were applied in the course of this study.

6.2.1 Field methodologies

Outcrop studies [*Lindsay et al.*, 1993; *Lehner and Pilaar*, 1997; *Heynekamp et al.*, 1999; *Sigda et al.*, 1999; *Sigda and Wilson*, 2003, , *e.g.* Chapter 3] are an important

key to characterize the hydrogeologic architecture of fault zones. The applied image analysis technique in combination with core-plug measurements provided a first picture of the fault zone hydraulic architecture of the Geleen Fault at cm scale. Extension of these techniques with field air-permeametry [*e.g. Davis et al.*, 1994] would be an attractive and efficient technique to reveal the larger scale variation of hydraulic conductivity around the fault zone.

Other types of field data that were gathered during numerous field campaigns over the last four years consists of geothermal and chemical data (Chapter 4) and hydraulic head data (Chapter 2). Although these data allowed to infer new insights on the groundwater flow patterns around shallow fault zones, there are remaining challenges in the application of these methodologies.

Geothermal studies in combination with further analysis of the chemistry of groundwater samples can be more extensively analyzed than has been done in Chapter 4. Analyzing the chemical signature of groundwater can reveal its origin and age and, consequently, present and palaeo groundwater flow paths [*e.g. Cook and Herczeg*, 2000; *Post*, 2004]. This approach is likely to yield interesting results as faults are often zones that separate aquifers with contrasting groundwater qualities [*e.g. Bon*, 1968]. Also the work by *Van Zanten* [1996], *Broers and Buijs* [1997] and *Minnema et al.* [2001] shows the potential of geochemical work around fault zones in the Netherlands in combination with the use of isotopes as tracers for groundwater movement.

The possibilities for interpretation of geothermal observations have been explored more extensively than those of the chemical analyses (Chapter 4). The geothermal methods applied at the field site near Uden revealed a very promising methodology that is worthwhile to develop further. A major problem during the field campaign was that it was difficult to push the temperature probe, as used for the measurements in the ditch, deeper than ~ 0.5 m into the ditch sediment. It is shown, however, in Chapter 4 (Figure 4.9) that even stronger horizontal temperature contrasts than observed in this study are expected at a depth of a few meters below the surface. Therefore, a major improvement of the field methodology that was applied here would be to develop field equipment that allows to probe ground temperatures at depths of several meters.

Although in the present study no data have been used from pumping tests that have been carried out over the last tens of years in the Netherlands, some of these field data were obtained in the vicinity of faults and further interpretation of these data may lead to new findings. Several workers already have focused specifically on drawdown patterns around leaky faults so that a first framework for such a

project is available [*e.g. Shan et al.*, 1995; *Maas*, 2000]. As suggested in the discussion part of Chapter 2, one aspect of such a study can be the horizontal anisotropy of hydraulic conductivity that might be recognized in drawdown patterns around pumping wells related to the possible occurrence of large numbers of small faults with a throw in the order of meters.

The possibility of mapping shallow fault patterns in the Netherlands using high-resolution shallow seismic methods has been demonstrated by for example *Tigrek et al.* [2000]. This technique will allow for a detailed analysis of fault patterns on a scale relevant for groundwater supply studies. Studying the structural linkage of shallow faults with those at greater depths in the basement of the Dutch subsurface as demonstrated, for example, by *Dirkzwager et al.* [2000] is of importance for the further assessment of faults on regional fluid flow patterns. In this respect analysis of patterns associated with recent fault activity (neo-tectonics) in the area is crucial [*e.g. Houtgast and van Balen*, 2000; *Cloetingh*, 2000; *Cloetingh et al.*, 2003].

6.2.2 Model studies

In this thesis work it is extensively shown in Chapter 2 and 5 what the regional impact of faults is to the groundwater flow system in the Lower Rhine Embayment south of the Roer Valley Rift System. Numerical groundwater flow models were applied to characterize the groundwater flow field around the Peel Boundary Fault Zone near Uden (Chapter 4) and fault relay zones (Chapter 5). An appealing practical challenge is to evaluate how important uncertainties in fault zone permeabilities are, as implemented in numerical models, to the calculated effect of de-watering activities in the Lower Rhine Embayment on the hydrogeological conditions in the Dutch part of the Roer Valley Graben. The magnitude of this effect is a matter of debate since the 1980s when model studies carried on both sides of the Dutch-German border produced considerable differences [*Olsthoorn*, 1989]. Since then, *Stuurman* [2000] has presented a model that suggests that the impact of the German mining industry on groundwater resources in the Netherlands is considerable. However, this model is very limited in complexity compared to the extensive modeling efforts by the hydrogeological research service of *RWE Power* (the former *Rheinbraun AG*) to simulate and forward calculate the groundwater flow situation in the area [*e.g. Peukert and Helmbold*, 2000].

In Chapter 5, it is shown that there exists a relation between the Shale Gouge Ratio (SGR) and the hydraulic head difference over the Rheindahlen Fault. A concise, direct calibration of the SGR values in this system for fault permeability was not

RWE Power is the company that exploits the open cast mines in the Lower Rhine Embayment

carried out during this study. However, experimental sediment deformation using for example ring-shear devices could be carried out to find out what the relation is between fault zone permeability and SGR under the appropriate confining pressures and taking into consideration the type of sediments found in the area. First steps in that direction were done for example by *Sperrevik et al.* [2000] and, under high confining pressures, by *Takahashi* [2003]. The work presented by *Van der Zee* [2002] forms a prime example how experimental work can improve our understanding of fault zone development and evolution in unconsolidated sediments. Through such an experimental approach, the evolution of fault zone permeability at geological time scales can possibly be better understood. The evolution of fault permeability at geological time-scales is relevant for the understanding and prediction of the present-day distribution of hydrocarbons within a basin [*Van Balen et al.*, 2000; *Verweij*, 2003]. Transient numerical simulations of changing fluid flow patterns around faults of which hydraulic properties evolve during fault movement, have not yet been undertaken. However, the SGR-approach seems a promising tool to simulate the evolution of fault zone permeability over time.

References

Andersson, J. E., L. Ekman, R. Nordqvist, and A. Winberg, Hydraulic testing and modelling of a low angle fracture zone at Finnsjon, Sweden, *Journal of Hydrology, 126*, 45–77, 1983.

Andrews, C. B., and M. P. Anderson, Thermal alteration of groundwater caused by seepage from a cooling lake, *Water Resources Research, 15*, 595–602, 1979.

Antonellini, M. A., and A. Aydin, Effect of faulting on fluid flow in porous sandstones: Petrophysical properties, *American Association of Petroleum Geologists Bulletin, 74*, 355–377, 1994.

Arch, J., and A. Maltman, Anisotropic permeability and tortuosity in deformed wet sediments, *Journal of Geophysical Research, 95*, 9035–9045, 1990.

Aydin, A., Fractures, faults, and hydrocarbon entrapment, migration and flow, *Marine and Petroleum Geology, 17*, 797–814, 2000.

Aydin, A., and A. M. Johnson, Development of faults as zones of deformation bands and as slip surfaces in sandstone, *Pure and Applied Geophysics, 11b*, 931–942, 1978.

Badleys Earth Sciences, FAPS - Traptester 4.2, *http://www.badleys.co.uk*.

Barker, A. P., R. J. Newton, S. H. Bottrell, and J. H. Tellam, Processes affecting groundwater chemistry in a zone of saline intrusion into an urban sandstone aquifer, *Applied Geochemistry, 13*, 735–749, 1998.

Bear, J., *Dynamics of fluids in porous media*, Environmental Sciences Series, Elsevier Publishing Company, Inc., New York, 1972.

Beltrami, H., On the relationship between ground temperature histories and meteorological records: a report on the Pomquet station, *Global and Planetary Change, 29*, 327–348, 2001.

Beltrami, H., Earth's long-term memory, *Science, 297*, 206–207, 2002.

Bense, V. F., and R. T. Van Balen, Hydrogeological aspects of fault zones on various scales in the Roer Valley Rift System, *Journal of Geochemical Exploration*, *78-79*, 317–320, 2003.

Bense, V. F., R. T. Van Balen, and J. J. De Vries, The impact of faults on the hydrogeological conditions in the Roer Valley Rift System: an overview, *Netherlands Journal of Geosciences/Geologie en Mijnbouw*, *82*, 41–53, 2003a.

Bense, V. F., E. H. Van den Berg, and R. T. Van Balen, Deformation mechanisms and hydraulic properties of fault zones in unconsolidated sediments; the Roer Valley Rift System, the Netherlands, *Hydrogeology Journal*, *11*, 319–332, 2003b.

Berner, R. A., *Early Diagenesis, A theoretical Approach*, Princeton Series in Geochemistry, Princeton University Press, Princeton, N.J., 1980.

Bierkens, M. F. P., Complex confining layers. A stochastic analysis of hydraulic properties at various scales., Ph.D. thesis, Universiteit Utrecht, 1994.

Bon, J., *Determination of the optimum combination of water management systems in areas with a microrelief*, vol. 56 of *Technical Bulletins*, chap. II. The configuration of the Groundwater table, p. 188, ICW, Wageningen, 1968.

Bouvier, J. D., C. H. Kaars-Sijpesteijn, D. F. Kluesner, C. C. Onyejekwe, and R. C. Pal, Three-dimensional seismic interpretation and fault sealing investigations, Nun River field, Nigeria, *American Association of Petroleum Geologists Bulletin*, *73*, 1397–1414, 1989.

Boyle, J. M., and Z. A. Saleem, Determination of recharge rates using temperature-depth profiles in wells, *Water Resources Research*, *15*, 1616–1622, 1979.

Bravo, H. R., F. Jiang, and R. J. Hunt, Using groundwater temperature data to constrain parameter estimation in a groundwater flow model, *Water Resources Research*, *38(8)*, 1153, doi:10.1029/2000WR000172, 2002.

Bredehoeft, J. D., and I. S. Papadopulos, Rates of vertical groundwater movement estimated from the Earth's thermal profile, *Water Resources Research*, *1*, 325–328, 1965.

Broers, H. P., and E. A. Buijs, The origin of trace-elements and ar in the water supply area of the village of Oostrum [in Dutch], *TNO-Rapport NITG 97-198-A*, NITG-TNO, Delft, 1997.

Buchter, B., C. Hinz, and H. Fluher, Sample size for determination of coarse fragment content in a stony soil, *Geoderma*, *63*, 265–275, 1994.

Burhannudinnur, M., and C. K. Morley, Anatomy of growth fault zones in poorly lithified sandstones and shales: implications for reservoir studies and seismic interpretation: part 1, outcrop study, *Petroleum Geoscience*, *3*, 211–224, 1997.

Buttner, G., and E. Huenges, The heat transfer in the region of the Mauna Kea (Hawaii) - Constraints from borehole temperature measurements and coupled thermo-hydraulic modeling, *Tectonophysics*, *371*, 23–40, 2003.

Caine, J. S., J. P. Evans, and C. B. Forster, Fault zone architcture and permeability structure, *Geology*, *24*, 1025–1028, 1996.

Carman, P. C., Determination of the specific surface of powders, *Journal Society Chemical Industry*, *57*, 225–234, 1938.

Cartwright, K., Tracing shallow groundwater systems by soil temperatures, *Water Resources Research*, *10*, 847–855, 1974.

Cartwright, K., Measurement of fluid velocity using temperature profiles: Experimental verification, *Journal of Hydrology*, *43*, 185–194, 1979.

Čermák, V., L. Bodri, and J. Šafanda, Recent climate change recorded in the underground: evidence from Cuba, *Palaeogeography, Palaeoclimatology, Palaeoecology*, *98*, 219–223, 1992.

Chan, M. A., W. T. Parry, and J. R. Bowman, Diagenetic hematite and manganese oxides and fault-related fluid flow in Jurassic sandstones, southeastern Utah, *American Association Petroleum Geologists Bulletin*, *84*, 1281–1310, 2000.

Chester, F. M., J. P. Evans, and R. L. Biegel, Internal structure and weakening mechanisms of the San Andreas fault, *Journal of Geophysical Research*, *98*, 771–786, 1993.

Childs, C., A. Nicol, J. J. Walsh, and J. Watterson, Growth of vertically segmented normal faults, *Journal of Structural Geology*, *18*, 1389–1397, 1996.

Childs, C., A. Nicol, J. J. Walsh, and J. Watterson, The growth and propagation of synsedimentary faults, *Journal of Structural Geology*, *25*, 633–648, 2003.

Cloetingh, S., Perspectives on environmental earth system dynamics, *Global and Planetary Change*, *27*, 1–21, 2000.

Cloetingh, S., P. Ziegler, and T. Cornu, Investigating environmental tectonics in northern Alpine foreland of Europe, *EOS, Transactions, American Geophysical Union*, *84*, 349, 356–357, 2003.

Constantz, J., A. E. Stewart, R. Niswonger, and L. Sarma, Analysis of temperature profiles for investigating stream losses beneath epheremal channels, *Water Resources Research*, *38(12)*, 1316, doi:10.1029 / 2001WR001221, 2002.

Constantz, J., S. W. Tyler, and K. Edward, Temperature-profile methods for estimating percolation rates in arid environments, *Vadose Zone Journal*, *2*, 12–24, 2003.

Cook, P., and A. L. Herczeg, *Environmental tracers in subsurface hydrology*, Kluwer Academic Publishers, Boston, 2000.

Csónka, J., Report on the applicability of the geothermal method in the Netherlands [in Dutch], *Tech. Rep. OS 92-40A*, TNO Dienst Grondwaterverkenning, Delft, 1968.

Darby, D., R. S. Haszeldine, and G. D. Couples, Pressure cells and pressure seals in the UK Central Graben, *Marine and Petroleum Geology*, *13*, 865–878, 1996.

Davis, J. M., J. L. Wilson, and F. M. Phillips, A portable air-minipermeameter for rapid in situ field measurements, *Ground Water*, *32*, 258–266, 1994.

De Glee, G. J., and S. Brandenburg, Report on the extension of the 'Prise d'Eau' of the Tilburg water supply [in Dutch], *Tech. rep.*, 1926.

De Jong, S. J., and W. Geirnaert, The groundwater thermal regime in the Flevo polders and the Gelderse Vallei (southern IJsselmeer area, The Netherlands), *Netherlands Journal of Geosciences/Geologie en Mijnbouw*, *58*, 295–304, 1979.

De Vries, J. J., Groundwater flow systems and stream nets in the Netherlands, Phd-thesis, Vrije Universiteit Amsterdam, Amsterdam, 1974.

De Vries, J. J., Dynamics of the interface between streams and groundwater systems in lowland areas, with reference to stream net evolution, *Journal of Hydrology*, *155*, 39–56, 1994.

Dirkzwager, J., J. Van Wees, S. Cloetingh, M. Geluk, B. Dost, and F. Beekman, Geo-mechanical and rheological modelling of upper crustal faults and their near-surface expressions in the Netherlands, *Global and Planetary Change*, *27*, 67–88, 2000.

Domenico, P. A., and V. V. Palciauskas, Theoretical analysis of forced convective heat transfer in regional ground-water flow, *Geological Society of America Bulletin*, *84*, 3803–3813, 1973.

Domenico, P. A., and F. W. Schwartz, *Physical and chemical hydrogeology*, 2nd ed., John Wiley & Sons, New York, 1998.

Doughty, P. T., Clay smear seals and fault sealing potential of an exhumed growth fault, Rio Grande Rift, New Mexico, *American Association of Peroleum Geologists Bulletin*, *87*, 427–444, 2003.

Ernst, L. F., and N. A. De Ridder, High resistance to horizontal ground-water flow in coarse sediments due to faulting, *Netherlands Journal of Geosciences/Geologie en Mijnbouw*, *39*, 66–85, 1960.

Evans, J. P., C. B. Forster, and J. V. Goddard, Permeability of fault-related rocks, and implications for hydraulic structure of fault zones, *Journal of Structural Geology*, *19*, 1393–1404, 1997.

Forster, C., and L. Smith, The influence of groundwater flow on thermal regimes in mountaineous terrain: A model study, *Journal of Geophysical Research*, *94*, 9439–9451, 1989.

Freeman, B., G. Yielding, D. T. Needham, and M. Badley, Fault seal prediction: the gouge ratio method, in *Structural geology in reservoir characterization*, edited by M. P. Coward, T. S. Daltaban, and H. Johnson, vol. 127 of *Special Publication*, pp. 19–25, Geological Society London, 1998.

Freeze, R. A., and J. A. Cherry, *Groundwater*, 1st ed., Prentice-Hall, Inc., London, 1979.

Fristad, T., A. Groth, G. Yielding, and B. Freeman, Quantitative fault seal production: a case study from Oseburg Syd, in *Hydrocarbon Seals: Importance for Exploration and Production*, edited by P. Møller-Pedersen and A. G. Koestler, pp. 107–124, Elsevier, Amsterdam, 1997.

Fulljames, J. R., J. J. Zijerveld, and R. C. M. W. Franssen, Fault seal processes: systematic analysis of fault seals over geological and production time scales, in *Hydrocarbon seals - imporatance for exploration and production*, edited by N. P. Society, vol. 9 of *NPF, Special Publication*, pp. 51–59, Nowegian Petroleum Society, Oslo, 1997.

Garven, G., M. S. Appold, V. I. Toptygina, and T. J. Hazlett, Hydrogeologic modeling of the genesis of carbonate lead-zinc ores, *Hydrogeology Journal*, *7*, 108–126, 1999.

Geluk, M. C., E. J. T. Duin, M. Dusar, and R. H. B. Rijkers, Stratigraphy and tectonics of the Roer Valley Graben, *Netherlands Journal of Geosciences/Geologie en Mijnbouw*, *73*, 129–141, 1994.

Gibson, R. G., Physical character and fluid-flow properties of sandstone derived fault gouge, in *Structural Geology in Reservoir Characterization*, edited by M. P. Coward, T. S. Daltaban, and H. Johnson, vol. 127 of *Special Publications*, pp. 83–97, Geological Society, London, 1998.

Haneberg, W. C., Steady state groundwater flow across idealized faults, *Water Resources Research*, *31*, 1815–1820, 1995.

Haneberg, W. C., P. S. Mozley, J. Casey Moore, and L. B. Goodwin (Eds.), *Faults and Subsurface Fluid Flow in the Shallow Crust*, vol. 113 of *AGU Geophysical Monograph Series*, American Geophysical Union, Washington D. C., 1999.

Harper, T. R., and E. R. Lundin, Fault seal analysis: reducing our dependance on empiricism, in *Hydrocarbon Seals: Importance for Exploration and Production*, edited by P. Møller-Pedersen and A. G. Koestler, vol. 7 of *NPF Special Publications*, pp. 149–165, Elsevier B. V., Singapore, 1997.

Harris, D., G. Yielding, P. Levine, G. Maxwell, P. T. Rose, and P. Nell, Using Shale Gouge Ratio (SGR) to model faults as transmissibility barriers in reservoirs: an example from the Strathspey Field, North Sea, *Petroleum Geoscience*, *8*, 167–176, 2002.

Heynekamp, M. R., L. B. Goodwin, P. S. Mozley, and W. C. Haneberg, Controls on fault-zone architecture in poorly lithified sediments, Rio Grande Rift, New Mexico: Implications for fault-zone permeability and fluid flow, in *Faults and Subsurface Fluid Flow in the Shallow Crust*, edited by W. C. Haneberg, P. S. Mozley, J. Casey Moore, and L. B. Goodwin, vol. 113 of *AGU Geophysical Monograph*, pp. 27–51, American Geophysical Union, Washington D. C., 1999.

Houtgast, R. F., R. T. Van Balen, L. M. Bouwer, G. B. M. Brand, and J. M. Brijker, Late Quaternary activity of the Feldbiss Fault Zone, Roer Valley Rift System, the Netherlands, based on displaced fluvial terrace fragments, *Tectonophysics*, *352*, 295–315, 2002.

Houtgast, R. H., and R. T. van Balen, Neotectonics of the Roer Valley Rift System, the Netherlands, *Global and Planetary Change*, *27*, 131–146, 2000.

Huang, S., H. N. Pollack, and P.-Y. Shen, Temperature trends over the past five centuries reconstructed from borehole temperatures, *Nature*, *403*, 756 – 758, 2000.

Hunt, R. J., D. P. Krabbenhoft, and M. P. Anderson, Assessing hydrogeochemical heterogeneity in natural and constructed wetlands, *Biogeochemistry*, *39*, 271–293, 1997.

Hunt, R. J., T. D. Bullen, D. P. Krabbenhoft, and C. Kendall, Using stable isotopes of water and strontium to investigate the hydrology of a natural and a constructed wetland, *Ground Water*, *36*, 434–443, 1998.

Knipe, R. J., The influence of fault zone processes and diagenesis on fluid flow, in *Diagenesis and Basin Development*, edited by A. D. Horbury and A. G. Robinson, vol. 36 of *Studies in Geology*, pp. 135–148, American Association of Petroleum Geologists, 1993.

Knott, S. D., Fault seal analysis in the North Sea, *American Association of Petroleum Geologists Bulletin*, *77*, 778–792, 1993.

Knott, S. D., A. Beach, brockbank P. J., J. Lawson, and J. L. Brown, Spatial and mechanical controls on normal fault populations, *Journal of Structural Geology*, *18*, 359–372, 1996.

Krcmár, B., and J. Mášín, Prospecting by the geothermic method, *Geophysical Prospecting*, *18*, 255–260, 1970.

Kukkonen, I. T., and C. Clauser, Simulation of heat transfer at the Kola deep-hole site: Implications for advection, heat refraction and paleoclimate effects, *Geophysics Journal International*, *116*, 409–420, 1994.

Langguth, H. R., and N. Ullrich, On the hydrochemistry of deep groundwater below clay layer no. 1 in the vicinity of 'Hambach' open-cast mine [in German], *Mitteilungen Ingenieurs- und Hydrogeologie*, *76*, 377–388, 2000.

Lansing Taylor, W., and D. D. Pollard, Estimation of in situ permeability of deformation bands in porous sandstone, valley of fire, Nevada, *Water Resources Research*, *36*, 2595–2606, 2000.

Lapham, W. W., Use of temperature profiles beneath streams to determine rates of vertical ground-water flow and vertical hydraulic conductivity, *U. S Geol. Surv. Water Supply Pap 2337*, USGS, 1989.

Larsen, P.-H., Relay structures in a Lower Permian basement involved extension system, East Greenland, *Journal of Structural Geology*, *10*, 3–8, 1988.

Lehner, F. K., and W. F. Pilaar, On a mechanism of clay smear emplacement in synsedimentary normal faults, in *Hydrocarbon Seals: Importance for Exploration and Production*, edited by P. Møller-Pedersen and A. G. Koestler, vol. 7 of *NPF Special Publications*, pp. 39–50, Elsevier B. V., Singapore, 1997.

Leveille, G. P., R. Knipe, C. More, D. Ellis, G. Dudley, G. Jones, Q. J. Fisher, and G. Allinson, Compartmentalization of Rotliegendes gas reservoirs by sealing fault, Jupiter fields are, southern North Sea, in *Petroleum Geology of the Southern North Sea: Future Potential*, edited by K. Ziegler, P. Turner, and S. Daines, vol. 123 of *Geological Society Special Publications*, pp. 87–104, 1997.

Lewis, T. J., and L. Wang, Geothermal evidence for deforestation induced warming: Implications for the climatic development, *Geophysical Research Letters*, *25*, 535–538, 1998.

Lindsay, N. G., F. C. Murphy, J. J. Walsh, and J. Watterson, Outcrop studies of shale smears on fault surfaces, in *The Geological Modelling of Hydrocarbon Reservoirs and Outcrop Analogues*, edited by S. S. Flint and I. D. Bryant, vol. 15, pp. 113–123, Blackwell Scientific publications, Oxford, 1993.

Lu, N., and S. Ge, Effect of horizontal heat and fluid flow on the vertical temperature distribution in a semiconfining layer, *Water Resources Research*, *32*, 1449–1453, 1996.

Maas, K., The drawdown pattern around a well close to a non-sealing fault in a layered aquifer [in Dutch], *Stromingen*, *6*, 37–49, 2000.

Mailloux, B. J., M. Person, S. Kelley, N. Dunbar, S. Cather, L. Strayer, and P. Hudleston, Tectonic controls on the hydrogeology of the Rio Grande Rift, New Mexico, *Water Resources Research*, *35*, 2641–2659, 1999.

Mal'kovskii, V., and A. Pek, Evaluation of the influence of a highly permeable fault on transport of pollutants by the local groundwater flow, *Geology of Ore deposits*, *43*, 216–223, 2001.

Manzocchi, T., J. J. Walsh, P. Nell, and G. Yielding, Fault transmissibility multipliers for flow simulation models, *Petroleum Geoscience*, *5*, 53–63, 1999.

Michon, L., R. T. Van Balen, O. Merle, and H. Pagnier, The Cenozoic evolution of the Roer Valley Rift System integrated at a European scale, *Tectonophysics*, *367 (1-2)*, 101–126, 2003.

Miedema, R., and T. Jongmans, Soil formation in Late Glacial Meuse sediments related to the Peel Boundary Fault activity, *Netherlands Journal of Geosciences/Geologie en Mijnbouw*, *81*, 71–81, 2002.

Minnema, B., G. Klaver, and J. Verstraelen, Pumping station Nuland: Fased reserch after the origin of chloride-treats [in Dutch], *Stromingen*, *7*, 33–46, 2001.

Møller-Pedersen, P., and A. G. Koestler (Eds.), *Hydrocarbon Seals - Importance for Exploration and Production*, Elsevier, Amsterdam, 1997.

Morley, C. K., and M. Burhannudinnur, Anatomy of growth fault zones in poorly lithified sandstones and shales: implications for reservoir studies and seismic interpretation: part 2, seismic reflection geometries, *Petroleum Geoscience*, *3*, 225–231, 1997.

Morley, C. K., R. A. Nelson, T. L. Patton, and S. G. Munn, Transfer zones in the East African Rift System and their relevance to hydrocarbon exploration in rifts, *American Association of Petroleum Geologists Bulletin*, *74*, 1234–1253, 1990.

Mozley, P. S., and L. B. Goodwin, Patterns of cementation along a Cenozoic normal fault: A record of paleoflow orientations, *Geology*, *23*, 539–542, 1995.

Nelson, E. P., A. J. Kullman, and M. H. Gardner, Fault-fracture networks and related fluid flow and sealing, Brushy Canyon formation, West Texas, in *Faults and Subsurface Fluid Flow in the Shallow Crust*, edited by W. C. Haneberg, P. S. Mozley, J. Casey Moore, and L. B. Goodwin, vol. 113 of *AGU Geophysical Monograph*, pp. 69–81, American Geophysical Union, Washington D. C., 1999.

Nuclear Energy Agency (Ed.), *Fluid flow through faults and fractures in argillaceous formations, a joint NEA/EC Workshop*, Organisation for Economic Co-operation and Development, Berne, Switzerland, 1996.

Ofoegbou, G. I., S. Painter, R. Chen, F. R. W., and D. A. Ferril, Geomechanical and thermal effects on moisture flow at the proposed Yucca mountain nuclear waste repository, *Nuclear Technology*, *134*, 241–262, 2001.

Olsthoorn, T. N., Goundwater lowering as a result of the German open cast mines in the Roer Valley Graben [in Dutch], *in Dutch 728610001*, Rijks Instituut voor Volksgezondheid en Milieuhygiene , 1989.

Paulissen, E., J. Vandenberghe, and F. Gullentops, The Feldbiss fault in the Maas valley bottom (Limburg, Belgium), *Netherlands Journal of Geosciences/Geologie en Mijnbouw*, *64*, 79–87, 1985.

PDE Solutions, *FlexPDE v. 3. 10*, http: / / www. pdesolutions. com, 2003.

Peacock, D. C. P., and D. J. Sanderson, Geometry and development of relay ramps in normal fault systems, *American Association of Petroleum Geologists Bulletin*, *78*, 147–165, 1994.

Person, M., J. P. Raffensberger, S. Ge, and G. Garven, Basin-scale hydrogeologic modeling, *Reviews of Geophysics*, *34*, 61–87, 1996.

Person, M., C. Neuzil, P. Hsieh, B. Mailloux, P. Eadington, E. Bekele, and J. Swenson, Rift2d: A finite element model for simulating two-dimensional fluid, heat, and solute mass transport in evolving sedimentary basin, *Water resources investigations report*, US Geological Survey Water Resources Investigation, submitted.

Peukert, D., and F. Helmbold, Investigations on the conservation of the ground-water resources in the North of the Rhineland brown coal mining area, using a ground-water model [in German], *Braunkohle*, *52*, 9–26, 2000.

Pittman, E. D., Effect of fault-related granulation on porosity and permeability of quartz sandstones. Simpson Group (Ordovician), Oklahoma, *American Association of Petroleum Geologists Bulletin*, *65*, 2381–2387, 1981.

Post, V. E. A., Groundwater salinization processes in the coastal area of the Netherlands due to transgressions during the Holocene, Phd-thesis, Vrije Universiteit Amsterdam, 2004.

Putnam, S. N., and D. S. Chapman, A geothermal climate change observatory: first year results from Emigrant Pass in northwest Utah, *Journal of Geophysical Research*, *101*, 21,877–21,890, 1996.

Rawling, G. C., L. B. Goodwin, and J. L. Wilson, Internal architecture, permeability structure, and hydrologic significance of contrasting fault zone types, *Geology*, *27*, 43–46, 2001.

Ronan, A. D., D. E. Prudic, C. E. Thodal, and J. Constantz, Field study and simulation and diurnal temperature effects on infiltration and variably saturated flow beneath an ephemeral stream, *Water Resources Research*, *34*, 2137–2153, 1998.

Sammel, E. A., Convective flow and its effect on temperature logging in small-diameter wells, *Geophysics*, *33*, 1004–1012, 1968.

Schäfer, A., D. Hilger, G. Gross, and F. von der Hocht, Cyclic sedimentation in Tertiary Lower-Rhine Basin (Germany) - the 'Liegendrücken' of the brown-coal open-cast Fortuna mine, *Sedimentary Geology*, *103*, 229–247, 1996.

Sebagenzi, M. N., G. Vasseur, and P. Louis, Recent warming in central Zaire (Central Africa) inferred from disturbed geothermal gradients, *Palaeogeography, Palaeoclimatology, Palaeoecology*, *98*, 209–217, 1992.

Shan, S., I. Javandel, and P. A. Witherspoon, Characterisation of leaky faults: study of water flow in aquifer-fault-aquifer systems, *Water Resources Research*, *31*, 2897–2904, 1995.

Sibson, R. H., Fluid flow accompanying faulting: Field evidence and models, in *Earthquake prediction; an international review*, edited by AGU, vol. 4 of *Maurice Ewing Series*, pp. 593–603, AGU, Washington D. C., 1981.

Sibson, R. H., Fluid involvement in normal faulting, *Journal of Geodynamics*, *29*, 469–499, 2000.

Sigda, J. M., and J. L. Wilson, Are faults preferential flow paths through semiarid and arid vadose zones?, *Water Resources Research*, *39*, 1225, doi:10. 1029 / 2002WR001406, 2003.

Sigda, J. M., L. B. Goodwin, P. S. Mozley, and J. L. Wilson, Permeability alteration in small-displacement faults in poorly lithified sediments: Rio Grande Rift, central New Mexico, in *Faults and Subsurface Fluid Flow in the Shallow Crust*, edited by W. C. Haneberg, P. S. Mozley, J. Casey Moore, and L. B. Goodwin, vol. 113, pp. 51–68, American Geophysical Union, Washington, D. C., 1999.

Silliman, S. E., and D. F. Booth, Analysis of time-series measurements of sediment temperature for identification of gaining v. losing portions of Juday Creek, Indiana, *Journal of Hydrology*, *146*, 131–148, 1993.

Silliman, S. E., J. Ramirez, and R. L. McCabe, Quantifying downflow through creek sediments using temperature time series: one-dimensional solution incorporating measured surface temperature, *Journal of Hydrology*, *167*, 99–119, 1995.

Smith, D. A., Sealing and non-sealing faults in Louisiana Gulf Coast basins, *American Association of Petroleum Geologists Bulletin*, *64*, 145–172, 1980.

Smith, L., and D. S. Chapman, On the thermal effects of groundwater flow - 1. Regional scale systems, *Journal of Geophysical Research*, *88*, 593–608, 1983.

Spelter, M., and D. Schneider, Considerations on the permeability of faults in the southerns part of the Lower Rhine Embayment, with special attention to the Rheindahlener Fault, using groundwater flow models [in german], *Mitteilugen Ingenieurs und Hydrogeologie*, *32*, 387–414, 1989.

Sperrevik, S., R. B. Farseth, and R. H. Gabrielsen, Experiments on clay smear formation along faults, *Petroleum Geoscience*, *6*, 113–123, 2000.

Sperrevik, S., P. A. Gillespie, Q. J. Fisher, T. Halvorsen, and R. J. Knipe, Empirical estimation of fault rock properties, in *Hydrocarbon Seal Quantification*, edited by A. G. Koestler and R. Hunsdale, vol. 11 of *NPF, Special publication*, pp. 109–125, Elsevier B. V., Amsterdam, 2002.

Stallman, R. W., Notes on the use of temperature data for computing ground-water velocity, *Tech. Rep. 3 (Question 1)*, Société Hydrotechnique de France, 1960.

Stallman, R. W., Steady one-dimensional fluid flow in a semi-infinite porous medium with sinusoidal surface temperature, *Journal of Geophysical Research*, *70*, 2821–2827, 1965.

STIBOKA, Soil map of the Netherlands - 50 Oost Tilburg, 1985.

Stolk, P., Analysis of temperature measurements in the Dutch subsurface (20 - 300m below ground surface) in relation to hydrological and meteorological conditions in the present and the past [in Dutch], Msc-thesis, Vrije Universiteit Amsterdam, 2000.

Stuurman, R. J., Transboundary hydrogeological processes in the southern Netherlands, in *Evaluation and protection of groundwater resources, conference Wageningen, 20 September 2000*, pp. 59–77, IAH, 2000.

Stuurman, R. J., and R. H. Atari, The groundwater flow situation around the "Wijstgronden" near the village of Uden [in Dutch], *Tech. Rep. 97-212(a)*, NITG-TNO, 1997.

Sverdrup, E., and K. Bjørlykke, Fault properties and the development of cemented fault zones in sedimentary basins: field examples and predictive models, in *Hydrocarbon Seals: Importance for Exploration and Production*, edited by P. Møller-Pedersen and A. G. Koestler, vol. 7 of *NPF Special Publication*, pp. 91–106, Elsevier, Singapore, 1997.

Takahashi, M., Permeability change during experimental fault smearing, *Journal of Geophysical Research*, *108*, 2235, doi:10. 1029 / 2002JB001984, 2003.

Taniguchi, M., Evaluation of vertical groundwater fluxes and thermal properties of aquifers based on transient temperature-depth profiles, *Water Resources Research*, *29*, 2021–2026, 1993.

Taniguchi, M., J. Shimada, T. Tadashi, I. Kayane, Y. Sakura, Y. Shimano, S. Dapaah-Siakwan, and S. Kawashima, Disturbances of temperature-depth profiles due to surface climate change and subsurface water flow: 1. An effect of linear increase in surface temperature caused by global warming and urbanization in the Tokyo metropolitan area, Japan, *Water Resources Research*, *35*, 1507–1517, 1999a.

Taniguchi, M., D. R. Williamson, and A. J. Peck, Disturbances of temperature-depth profiles due to surface climate change and subsurface water flow: 2. An effect of step increase in surface temperature caused by forest clearing in southwest Western Australia, *Water Resources Research*, *35*, 1519–1529, 1999b.

Tiab, D., and E. C. Donaldson, *Porosity and permeability*, chap. 3, pp. 77–136, Gulf Publishing Company, Houston, TX - USA, 1996.

Tigrek, S., P. Kiden, R. Houtgast, and J. Van Kuijk, A high resolution seismic survey on the river Maas, in *EAGE Conference - Petrophysics meets Geophysics*, edited by EAGE, EAGE, Paris, 2000.

TNO-NITG, Groundwater map of the Netherlands - Roer Valley Graben; 57 East - 58 West - 58 East, 1974a.

TNO-NITG, Groundwater map of the Netherlands - 's-Hertogenbosch; 45 West - 45 East, 1974b.

Van Balen, R., J. M. Verweij, J. D. van Wees, H. Simmelink, F. Van Bergen, and H. Pagnier, Deep subsurface temperatures in the Roer Valley Graben and the Peelblock, the Netherlands - new results, *Netherlands Journal of Geosciences/Geologie en Mijnbouw*, *81*, 19–27, 2002.

Van Balen, R. T., F. van Bergen, C. de Leeuw, H. Pagnier, H. Simmelink, J. D. Van Wees, and J. M. Verweij, Modelling the hydrocarbon generation and migration in the West Netherlands Basin, the Netherlands, *Netherlands Journal of Geosciences/Geologie en Mijnbouw*, *79*, 29–44, 2000.

Van den Berg, E. H., A. G. C. A. Meesters, J. A. M. Kenter, and W. Schlager, Automated separation of touching grains in digital images of thin sections, *Computers & Geosciences*, *28*, 179–190, 2002.

Van den Berg, E. H., V. F. Bense, and W. Schlager, Assessing textural variation in laminated sands using digital image analysis of thin sections, *Journal of Sedimentary Research*, *73*, 133–143, 2003.

Van den Berg, M., K. Vaneste, B. Dost, A. Lokhorst, M. Van Eijk, and K. Verbeeck, Paleoseismic investigations along the peel boundary fault: geological setting, site selection and trenching results, *Netherlands Journal of Geosciences/Geologie en Mijnbouw*, *81*, 39–60, 2002.

Van der Zee, W., Dynamics of fault gouge development in layered sand-clay sequences, Ph.D. thesis, Rheinisch-Westfälischen Technischen Hochschule, Aachen, 2002.

Van Wirdum, G., Vegetation and hydrology of floating rich-fens, Phd-thesis, University of Amsterdam, 1991.

Van Zanten, E., Risk analysis of the Gilzerbaan Fault Zone [in Dutch], *Tech. rep.*, Vrije Universiteit Amsterdam, 1996.

Vandenberghe, J., Geoelectric investigations of a fault system in Quaternary deposits, *Geophysical Prospecting*, *30*, 879–897, 1982.

Vandenberghe, J., Morphological effects of Pleistocene faulting in unconsolidated sediments (Central Graben, Netherlands), *Zeitschrift fur Geomorphologie N. F.*, *Heft 1*, 113–124, 1990.

Verweij, J. M., Fluid flow systems analysis on geological timescales in onshore and offshore Netherlands, Phd-thesis, Vrije Universiteit Amsterdam, 2003.

Visser, W. C., The problem of the "Wijstgronden" [in Dutch], *Tijdschrift van het Koninklijk Aardrijkskundig Genootschap*, *65*, 798–823, 1948.

Wallbraun, A., The impact of block-bounding faults on groundwater discharge in the Lower Rhine Embayment [in German], Ph.D. thesis, Rheinisch-Westfälischen Technischen Hochschule, Aachen, 1992.

Walsh, J. J., and J. Watterson, Displacement gradients on fault surfaces, *Journal of Structural Geology*, *11*, 307–316, 1989.

Walsh, J. J., J. Watterson, W. R. Bailey, and C. Childs, Fault relays, bends and branch-lines, *Journal of Structural Geology*, *21*, 1019–1026, 1999.

Walsh, J. J., W. R. Bailey, C. Childs, A. Nicol, and C. G. Bonson, Formation of segmented normal faults: a 3-D perspective, *Journal of Structural Geology*, *25*, 1251–1262, 2003.

Willemse, E. J. M., D. D. Pollard, and A. Aydin, Three-dimensional analyses of slip distributions on normal fault arrays with consequences for fault scaling, *Journal of Structural Geology*, *18*, 295–309, 1996.

Winstanley, A. M., A review of the Triassic play in the Roer Valley Graben, SE onshore Netherlands, in *Petroleum Geology of Northwest Europe: Proceedings of the 4th Conference*, edited by J. R. Parker, London, 1993.

Woodbury, A. D., and L. Smith, Simultaneous inversion of hydrogeologic and thermal data - 2. Incorporation of thermal data, *Water Resources Research*, *24*, 356–372, 1988.

Yechieli, Y., U. Kafri, M. Goldman, and C. I. Voss, Factors controlling the configuration of the fresh-saline water interface in the Dead Sea coastal aquifers: synthesis of TDEM surveys and numerical groundwater modeling, *Hydrogeology Journal*, *9*, 367–377, 2001.

Yielding, G., Shale Gouge Ratio - calibration by geohistory, in *Hydrocarbon Seal Quantification*, edited by A. G. Koestler and R. Hunsdale, vol. 11 of *NPF, Special publication*, pp. 1–15, Elsevier B. V., Amsterdam, 2002.

Yielding, G., B. Freeman, and D. T. Needham, Quantitative fault seal prediction, *American Association of Petroleum Geologists Bulletin*, *81*, 897–917, 1997.

Yielding, G., J. A. Øverland, and G. Byberg, Characterization of fault zones for reservoir modeling: An example from the Gullfaks Field, Northern North Sea, *American Association of Petroleum Geologists Bulletin*, *83*, 925–951, 1999.

References

Ziegler, P. A., Cenozoic rift system of western and central Europe: an overview, *Netherlands Journal of Geosciences/Geologie en Mijnbouw*, *73*, 99–127, 1994.

Zijl, W., *Scale analysis in groundwater hydrology*, vol. 24 of *Hydrology series - Vrije Universiteit Brussel*, Brussels, Belgium, 1993.

Acknowledgements

Veel mensen hebben tijdens de afgelopen jaren bijgedragen aan het tot stand komen van dit proefschrift. Die wil ik hier bedanken.

In de eerste plaats ben ik mijn promotores Sierd Cloetingh en Co de Vries dankbaar voor het initiatief om een project te starten waarin hydrologie en structurele geologie dichterbij elkaar gebracht zouden worden, en mij te vragen dat uit te voeren. Ronald van Balen, co-promotor en ook lid van de leescommissie, dank ik voor zijn begeleiding, advies, steun en het meeschrijven van delen van het proefschrift en artikelen. Co de Vries heeft waardevolle aanvullingen en commentaar op de inhoud van dit proefschrift gegeven.

The members of the reading committee, John Walsh (Fault Analysis Group Dublin), Hanneke Verweij (NITG-TNO), Hans Gehrels (NITG-TNO) en Peter Kukla (RWTH - Aachen) are gratefully acknowledged for all of the attention they have given to the manuscript of my thesis.

I would like to thank Mark Person (Indiana University) for being of support over the last few years and for his comments and criticism on parts of the work reported in this thesis. I look forward to working with him for the years to come.

Ik weet nog goed hoe verbaasd Vincent Post en ik waren toen we de ondiepe stijghoogtes maten in de sleuf over de Peelrandbreuk bij Neer en na uitgebreid waterpassen en hermeten toch echt moesten concluderen dat hier iets abnormaals aan de hand was (zie Figuur 2.15). Vinc, bedankt voor je stimulerende hulp op deze eerste dag dat ik het gevoel had dat ik echt iets aan het onderzoeken was. Deze eerste waarnemingen heb ik verwerkt in het artikel dat ik vervolgens samen met Ronald van Balen en Co de Vries heb geschreven (Hoofdstuk 2).

Zonder de samenwerking met Elmer van den Berg had het derde hoofdstuk van mijn proefschrift er heel anders uitgezien. Met hem heb ik het werk aan de sedimentmonsters

gedaan die we hadden verzameld tijdens een regenachtig en experimenteel weekend in de door Rob Houtgast gegraven sleuf over de Geleenbreuk. Deze monsters zijn vervolgens vakkundig ingegoten met blauwe hars, gezaagd en geslepen door Nanda Koot en Bouk Laçet van de afdeling gesteentebewerking. Wim Lustenhouwer stond me toe om een aantal detailfoto's van de slijpplaatjes te maken met behulp van zijn daarvoor uitgeruste microscoop. Uiteindelijk is dit onderzoek verwerkt tot mijn eerste publicatie die ik samen met Elmer van den Berg en Ronald van Balen heb geschreven (Hoofdstuk 3)

Voor het uitvoeren van het veldwerk bij Uden heb ik veel hulp gehad van Vincent Post, Elmer van den Berg, Boris van Breukelen (bedankt voor het introduceren van de hoog debiet pomp), Michele Minihane, Michiel Driessen en mijn vader. Al dat veldwerk had ik niet kunnen doen zonder de apparatuur (de "prikstok" en haspels) die door de de instrumentmakers (Harry Visch, Michel Groen, Jan Vink, Niek van Harlingen) op de begane grond en op de afdeling elektronica (Johan de Lange, Ron Lootens) is ontwikkeld. Hetty Shäfer en Kay Beets dank ik voor de chemische analyses die zij hebben gedaan van de grondwatermonsters. Voor de uitwerking van de veldgegevens heb ik nauw met Henk Kooi samengewerkt. Henk heeft me geholpen heeft met opzetten van de numerieke simulaties van de warmteverdeling in de ondergrond rondom de Peelrandbreuk en samen met hem heb ik grote delen van Hoofdstuk 4 een aantal keer herschreven.

The research that is reported in Chapter 5 benefitted largely from the course I followed with Graham Yielding at Badleys Geosciences (*http://www.badleys.co.uk*) on fault seal analysis. I also thank Peter Bretan and other people at Badleys for allowing me to come over a second time and for their effort to learn me how to handle the TRAPTESTER software. The data that I worked on for this study had been made available by *RWE Power* (the former *Rheinbraun AG*) that exploits the lignite mines in the Lower Rhine Embayment. Dr. Tomas Oswald (*RWE Power*, Cologne), Dr. Christian Forkel and Dr. Jens Voigt are very much thanked for all of their help concerning the data availability. Additionally, Dr. Axel Wallbraun (Erftverband, Bergheim) and Dr. Fritz von der Hocht (*RWE Power*, Cologne) are gratefully acknowledged for making our descent into the impressively large and deep lignite mines a succes.

Bij het Nederlands Instituut voor Toegepaste Geowetenschappen heb ik vooral tijdens de eerste jaren van mijn onderzoek een aantal stimulerende gesprekken gehad met Gerard Klaver, Meindert van den Berg en Patrick Kiden waarvoor ik ze hartelijk dank. Dick Edelman (Tilburgse Waterleiding Maatschappij), Maria Juhász (Waterleiding Maatschappij Limburg) en Inke Leunk (Brabant Water) zijn zeer behulpzaam geweest bij het verlenen van toestemming voor het uitvoeren van veldwerk en/of het beschikbaar maken van gegevens. Met Dick Edelman heb ik daarnaast ook de nodige zeer aangename uurtjes gesproken over alle curiosia die zich in de Nederlandse ondergrond afspelen en afgespeeld hebben in het geologische verleden. Ik dank Piet van Rooijen voor de aangename dag die ik bij hem heb doorgebracht in het zuiden van Limburg voor het bespreken van de verschillende aspecten

van grondwaterstroming rondom breuken.

De veldwerken langs de Brabantse Wal voor de eerstejaars waren alle jaren erg leuk en leerzaam en ik dank Mark Bokhorst, Saskia Keesstra, Gerard Aalbersberg, Patrick Bogaart, Kay Beets, Jaap Griede, Cees Kasse en Wim Hoek voor alle plezier en leermomenten die we daar gehad hebben. Kick, bedankt voor je altijd weer onoplosbare raadsels tijdens de koffie en wervelende discussies.

Over de laatste jaren heb ik heel wat mensen op de C-4 gang zien gaan en komen. Toen ik begon zaten Rob, Patrick, Govert, Albert en Henk in de kamers om mij heen. Daar kwamen al snel Boris, Vincent, Rik, Gu en Elmer bij. Gelukkig maar, zonder jullie was alles heel anders gelopen. Elmer, bedankt voor de tijd dat we samen in C-416 zaten, echt ruim was het niet maar wel gezellig toch? Later kwamen Mirjam en Mark de C-4 gang binnen en op het laatst ook nog Stefan, Freek, Jochem, Jos en Ane. Het was altijd weer een mooi gezicht om te zien hoeveel deuren er in de C-4 gang open stonden terwijl het in de F-4 gang meestal toch wat rustiger was. Zeer bedankt voor jullie aanwezigheid, steun en gezelligheid.

Adri, sorry dat het altijd zo kort was.

Michiel en Elmer, dank jullie wel dat jullie me bijstaan als paranimfen tijdens het verdedigen van dit proefschrift.

Mijn moeder heeft mijn promotie niet mogen meemaken. Ze overleed vlak voordat ik op de VU begon in 1999. Ik ben haar en mijn vader dankbaar voor het me laten doen wat ik graag wilde doen en voor de steun en liefde die ze daarbij altijd gegeven hebben.

Sylvia en een nu nog kleine Ronja zijn onmisbaar in alles, ik hou van ze en ik ben heel blij dat ze met me mee willen verhuizen naar een nieuwe plek in een ander land, zo ver weg.

Amsterdam, Juni 2004

Bezinning

Na de schrik en
Begenadiging
Onder 't snikken
Van verzadiging,

Na de feesten
Van het vleesch
Keert de geest en
Rijst de vrees:

Deze extase
Keert niet weer.
't Licht doet dwaas en
't Leven zeer

J. Slauerhoff (1898-1936)